

**Experiments on Compressor Cascades  
Using a Helium-Driven Shock Tube**

**Paulus Iwan Setiawan**

**A Thesis  
in  
The Department  
of  
Mechanical  
Engineering**

**Presented in Partial Fulfillment of the Requirements  
for the degree of Master of Engineering at  
Concordia University  
Montréal, Québec, Canada**

**March 1984**

**© Paulus Iwan Setiawan, 1984**

-1-

ABSTRACT

Experiments on Compressor Cascades  
Using a Helium-Driven Shock Tube

Paulus Iwan Setiawan

The performance of a helium driven shock tube, 15.25 cm in diameter and 7 m long, is investigated experimentally for its ability in providing uniform flow for use in testing supersonic flow in compressor cascades. At the downstream end of the shock tube, a 5 by 10 cm rectangular tube, 2.4 m long, was mounted to allow two-dimensional flow visualization in the test section which was designed to hold the cascades at various angle of incidences to the incoming flow direction.

The uniformity of the flow entering the test section was examined via spark schlieren photography and the use of a wedge and a blunt body of revolution. Pressure measurements were performed downstream of the shock tube to determine the duration of the uniform flow. The results show the presence of a constant pressure period of about 1.0 milliseconds. Out of this period the total data acquisition time was mathematically found to be around 0.55 milliseconds, which is large enough for the flow to achieve steady conditions.

Compressor cascades were mounted in the test section at various angle of incidences to the uniform supersonic flow at a Mach number of 1.53 and the flow was examined via spark schlieren photography and pressure measurements. Using three blade system, mounted on two plexyglass windows, similarity in the flow was easily achieved, provided that two extension plates are present downstream of the first and the last blades.

The flow conditions and pressure ratios across the cascades were varied by means of a damper placed at the end of the extension plates. With the damper absent, supersonic flow is maintained inside passages. The contact of discontinuity at the trailing edge and associated oblique shock waves system were clearly observed. By placing small disturbances along the suction and pressure surfaces, additional Mach waves were formed in the flow. The experimental Mach number variation along both surfaces, were then determined by measuring the Mach angles from corresponding schlieren pictures. They were found to be in close agreement with those obtained theoretically by the method of characteristics and with those provided by PWAC using Time Dependent Finite Difference Scheme with artificial viscosity. With damper partially closed, strong shock waves were observed and the flow behind those shocks become subsonic.

**FIGURE**

**PAGE**

27	Surface Pressure Distribution for Pressure Ratio of 1.4 and Zero Degrees Angle of Incidence . . . . .	111
28	Surface Pressure Distribution Provided by PWAC for 1.64 Pressure Ratio and Zero Degrees Angle of Incidence . . . . .	112

## TABLE OF CONTENTS

	<u>PAGE</u>
ABSTRACT . . . . .	i
ACKNOWLEDGEMENT . . . . .	iii
TABLE OF CONTENTS . . . . .	iv
LIST OF FIGURES . . . . .	vi
LIST OF TABLES . . . . .	x
NOMENCLATURE . . . . .	xi
CHAPTER	
1 INTRODUCTION . . . . .	1
2. THEORETICAL ANALYSIS . . . . .	4
2.1 Shock Tube Theory . . . . .	4
2.2 The Choice of the Driver Gas . . . . .	6
2.3 Two Dimensional Analysis of Supersonic Flow Around Airfoils . . . . .	8
2.4 Process Occuring at the Shock Tube Exit . . . . .	13
2.5 Different Methods of Obtaining Supersonic Flow of Mach Number 1.53 . . . . .	14
3. EXPERIMENTAL APPARATUS AND PROCEDURES . . . . .	16
3.1 The 52 mm Square Shock Tube . . . . .	16
3.2 The 15.25 cm Nominal Size Circular Shock Tube . . . . .	16
3.3 Design and Functions of the Rectangular Cross Section Tube . . . . .	18
3.4 The Test Section . . . . .	19
3.5 The Schlieren System . . . . .	19
3.6 The Time-Delayed Spark System . . . . .	21
3.7 Secondary Units . . . . .	23
3.8 Pressure and Velocity Measurements . . . . .	24
3.8.1 Pressure Measurement . . . . .	24
3.8.2 Velocity Measurement . . . . .	25
3.8.3 Uniformity in the Test Section . . . . .	26
4. EXPERIMENTAL RESULTS AND DISCUSSIONS . . . . .	28
4.1 Performance of a Helium-Driven Square Shock Tube . . . . .	28
4.1.1 Flow Uniformity and Test Time Duration . . . . .	28
4.1.2 Data Acquisition Time Interval . . . . .	30
4.1.3 Flow Visualization and Shock Structure . . . . .	32
4.1.4 Concluding Remarks Concerning the Test Con- ducted Using Square Shock Tube . . . . .	33

<u>CHAPTER</u>	<u>PAGE</u>
4.2 Tests Conducted Using the 15.25 cm Nominal Size Shock Tube . . . . .	33
4.2.1 Flow Structure and Uniformity in the Test Section . . . . .	34
4.2.2 Shock Wave Structure Within the Cascade Passage at Different Pressure Ratios . . . . .	35
4.2.3 Pressure Variations Along the Suction and Pressure Surfaces . . . . .	37
5. CONCLUSION . . . . .	43
REFERENCES . . . . .	47
APPENDIX I: Derivation of Shock Tube Equations . . . . .	51
APPENDIX II: Spacial 2-D Supersonic Irrotational Flow . . . . .	59
APPENDIX III: Process Occuring Inside Driven Section . . . . .	66

LIST OF FIGURES

<u>FIGURES</u>		<u>PAGE</u>
1a	A Simple Shock Tube Assembly . . . . .	69
1b	Pressure Distribution Along the Shock Tube . . . . .	69
1c	x,t Diagram of the Process Occuring . . . . .	70
2	Shock Mach Number Against The Pressure Ratio of the Driver to the Driven Chambers . . . . .	71
3a	Wave Diagram for 4 Degrees Angle of Incidence . . . . .	72
3b	Wave Diagram for 0 Degrees Angle of Incidence . . . . .	73
4	The Transmitted Shock Wave Diffraction Process at the Downstream end of the driven section and the Open End Pressure History . . . . .	74
5	Helium Driven Shock Tube With Two Driver Chambers . . . . .	75
6	A Schematic of the Square Shock Tube and its Accesories . . . . .	76
7	The Cylindrical Shock Tube and its Auxiliary Equipments . . . . .	77
8	The Rectangular Cross Section Extension Tube . . . . .	78
9	Shock Tube Test Section . . . . .	79
10	Top View of the Schlieren System . . . . .	80
11	The Time-Delay Spark System . . . . .	81

**FIGURE**

**PAGE**

12a	Transducer Pressure Traces for 3.5 m Driven Section Length . . . . .	82
12b	Interpretation of Fig. 12a . . . . .	83
13a	Transducer Pressure Traces for 4.5 m Driven Section Length . . . . .	84
13b	Interpretation of Fig. 13a . . . . .	85
14	The Blunt Body of Revolution . . . . .	86
15	The 6 Degrees Included Angle Wedge . . . . .	87
16a	Schlieren Photographs of a Blunt Body for Determining Flow Uniformity in the Longitudinal Direction . . . . .	88
16b	Mach Number Variation in the Longitudinal Direction . . . . .	90
17a	Schlieren Photographs of a Wedge for Determining Flow Uniformity in Transverse Direction . . . . .	91
17b	Mach Number Variation in Lateral Direction . . . . .	93
18	Reflected Shock Wave Interaction with the Expansion Waves Originating at the Open End . . . . .	94
19	Data Acquisition Time Interval . . . . .	95
20a	Schlieren Picture of a Single Turbine Blade Inside Uniform Supersonic Flow of Mach Number 1.4 . . . . .	96
20b	Schlieren Picture of Two Turbine Blades Inside Uniform Supersonic Flow of Mach Number 1.4 . . . . .	97



FIGURE		<u>PAGE</u>
20c	Schlieren Picture of Two Turbine Blades with Damper Placed Downstream of the System . . . . .	98
21	The Wave Diagram of the Underexpanded Jet . . . . .	99
22a	Schlieren Photographs of a Wedge Inside Uniform Supersonic Flow . . . . .	100
22b	Uniform Supersonic Flow Mach Number . . . . .	102
23	Schlieren Picture of the Cascade System Exposed to Super- sonic Flow of $M = 1.53$ and 4 Degrees Angle of Incidence . . . . .	103
24	Schematic View of the Damper . . . . .	104
25a	Schlieren Picture of Three Blade Cascade System with 8% Reduction of Exit Area . . . . .	105
25b	Schlieren Picture of Three Blade Cascade System with 10% Reduction of Exit Area . . . . .	106
25c	Schlieren Picture of Three Blade Cascade System with 24% Reduction of Exit Area . . . . .	107
26a	Surface Pressure Distribution for Pressure Ratio of 1.3 and 4 Degrees Angle of Incidence . . . . .	108
26b	Surface Pressure Distribution for Pressure Ratio of 1.62 and 4 Degrees Angle of Incidence . . . . .	109
26c	Surface Pressure Distribution for Pressure Ratio of 2.0 and 4 Degrees Angle of Incidence . . . . .	110

ACKNOWLEDGEMENT

The author would like first to express his gratitude to Dr. R.A. Neemeh for his constant encouragement, for his many helpful suggestions and generous guidances through the course of this work.

Thanks are due to Mr. D. Dress for his assistance in the experiment.

Thanks are due to Mr. Z. Ahmad for his assistance in the experiment and for his enlighting discussions.

Thanks are due to Messrs. E. Heasman, P. Schreck, H. Hugener and E. Haeseli for designing, suggesting and machining the testing facilities.

Thanks are due to Miss Jayne Claassen for typing this thesis.

The present work was supported by the Natural Science and Engineering Research Council of Canada under PRAI/Grant No. P-8102. Partial support under Grant No. A-4206 is acknowledged.

LIST OF TABLES

<u>TABLE</u>		<u>PAGE</u>
1.	Coordinate Points of the Blade Surfaces . . . . .	114
2a.	Wave Diagram Calculation Steps for 4 Degrees Angle of Incidence . . . . .	116
2b.	Wave Diagram Calculation Steps for 0 Degrees Angle of Incidence . . . . .	122

NOMENCLATURE

a	Speed of sound
Q	Nondimensional form of a; $a/a_0$
A	Cross-sectional area
$C_p$	Specific heat at constant pressure
$C_v$	Specific heat at constant volume
d	Blunt body nose diameter
g	Gravity acceleration
L	Length
M	Flow Mach number
$M_s$	Shock Mach number
n	Normal to stream line
p	Pressure
$Q = v + \theta$	Riemann variables for steady 2-dimensional flow
$R = v - \theta$	
$Q = \frac{2}{\gamma - 1} a - U$	Riemann variables for unsteady 1-dimensional flow
$R = \frac{2}{\gamma - 1} a + U$	
R	Gas constant
S	Specific entropy
s	Stream line direction
t	Time
T	Temperature
u	Flow velocity in x-direction
U	Nondimensional form of u; $u/u_0$
$u_s$	Shock velocity
v	Flow velocity in y direction

Nomenclature cont'd:

x	Coordinate
X	Nondimensional form of x; $x/L_0$ or $x/a_0 t$
y	Coordinate
$\alpha$	Incidence angle to the flow direction
$\beta$	Shock wave angle
$\gamma$	Ratio of specific heats; $C_p/C_v$
$\delta$	Distance from flat nose of the blunt body to outer edge of the detached shock
$\rho$	Density
$\xi$	Coordinate along the constant R characteristics
$\nu$	Prandtl-meyer function
$\eta$	Coordinate along the constant Q characteristics
$\mu$	Angle between mach line and stream line
$\tau$	Nondimensional form of t; $a_0 t/L_0$
$\theta$	Deflection angle
$\phi$	Half wedge angle

Subscripts

0	Reference condition
1	Condition ahead of shock wave
2	Condition behind shock wave
s	Shock wave
t	Stagnation condition

## CHAPTER I INTRODUCTION

The design of supersonic compressor cascades has been hampered in the past due to the difficulties in simulating the flow conditions which they undergo in actual flight, experimentally as well as analytically. Due to the fact that mathematical treatment of the supersonic flow about an airfoil is so involved, experimental investigation may therefore be needed, especially in those cases where theory cannot predict the real performance of compressors under some specific operating conditions. Experimentally, research and development on compressor has always been expensive and time consuming, in large part because simulation of both Mach number and Reynolds number has necessitated research on full sized, full speed test rigs, with problems of large mechanical stress and high power consumptions.

There are many testing facilities which are currently used, to name a few, the Supersonic Wind Tunnel, the combusted Ludweig Tube and the MIT Blow Down Compressor [1-2]. Although these apparatus enable one to obtain the desired flow conditions, the operating costs, maintenance and power limitations have restricted the continuous use of those facilities.

For the above reasons, it is the objective of this research to eliminate some of these restrictions and make possible fundamental studies of aerodynamics, with full flow conditions simulation at modest cost. This led to the conception of this experiment to be discussed here, in which a shock tube is used to drive a test gas, through the proposed compressor cascade, at a supersonic uniform flow.

The type of shock tube employed is unique in a way that the test section is located downstream of the expansion chamber and open to ambient. This arrangement offers several advantages [3]: First it eliminates the problem of leakages, second, it offers simpler ways of installing the test object and in altering the design as compared to the test section located inside the expansion chamber. The downstream end of the shock tube (driven section) is separated from ambient air by a thin diaphragm while the driver section, which is separated from the driven section with another diaphragm, is filled with helium at a specific pressure.

The driven section is evacuated to a predetermined pressure, such that when the diaphragm is burst the incident shock leaves the shock tube, followed by the supersonic flow. During the passage of this supersonic flow, aerodynamics data are acquired via schlieren photography and pressure measurements.

Different flow Mach number could be obtained by varying the diaphragm thickness separating the driver and driven chamber and/or varying the pressure ratios across the two chambers. The duration of uniform supersonic flow in the test section could be varied by varying the length of the driven section.

The advantages of using the present techniques over those of the Combusted Ludweig Tube are the omission of the required nozzle and choke plates designed specifically for a given flow Mach number and the elimination of the combustion process which did lead to flow non-uniformity. The factors contributed to the low cost of the present design are the small amount of

the test gas used and various different gases that could be employed depending on the flow Mach number desired. Finally this apparatus could be used not only for investigating flow behaviour about compressor or turbine airfoils, but also, if proper modifications are made, for other types of aerodynamic testings, i.e. for investigating the stability of converging shock wave [4].

In the following chapter, the theoretical analysis of the shock tube and the method of characteristics which is used for flow calculating inside the cascade passage, are presented. The experimental apparatus and its secondary units, followed by discussion about the experimental procedures and techniques are presented in Chapter 3.

Experimental results and discussions are described in Chapter 4. Finally, Chapter 5 completes the reports with the concluding remarks and points to be improved for future study.

In the appendix detailed derivations of shock tube equations are included.



CHAPTER II  
THEORETICAL ANALYSIS

2.1 Theory of Shock Tube

A shock tube is a device in which high speed flow and shock waves are produced by means of rupturing the diaphragm separating the high pressure region (driver) and low pressure region (driven) [5]. Fig. 1a shows a schematic of a simple shock tube while Fig. 1b shows the pressure distribution along the shock tube prior to and just after the rupture of the diaphragm.

When the diaphragm is caused to rupture by simply increasing the driver chamber pressure, a shock wave travels into the low pressure chamber and a rarefaction waves travel back into the high pressure chamber.

The region bounded by the shock front and the tail of the expansion waves is a region of constant pressure and uniform velocities. However, the temperature and densities in these regions are not uniform. The regions, of different temperatures and densities are separated by broken line (Fig. 1c) which is called contact surface [6]. The broken line in Fig. 1c denotes the position occupied by that gas which was originally at the diaphragm, the gas on the right side of the contact surface has been heated and compressed by the shock wave and hence has lower densities than the one located on the left of the contact surface which has been cooled by the expansion waves.

Fig. 1c shows the X-t diagram of the processes occurring in the shock tube after rupture of the diaphragm. Region 1 contains the gas that

originally occupies the driven chamber whereas region 4 contains the gas that originally occupies the driver chamber. The shock front is represented by line OA which has the slope of  $\frac{dt}{dx} = \frac{1}{u_s}$ .

When this shock reaches the end of the expansion chamber, it reflects, thus creating a pressure build up behind this reflected shock. At one point of the process the pressure becomes excessive and causes the second thin diaphragm to burst. This will result in the formation of a transmitted shock and a reflected wave. The transmitted one diffracts and causes the pressure at the downstream end to drop monotonically, resulting in a system of expansion waves to travel upstream catching up with the reflected shock and make it change its direction to leave the shock tube as demonstrated in Fig. 1c.

Accordingly, the experimental data should be obtained during the time interval between the arrival of the reflected shock wave and that of the contact surface to the downstream end of the shock tube. In Fig. 1c, the contact surface is represented by broken-line OB whose slope is  $1/u_2$ . It will be demonstrated later that this test time interval is a function of driven chamber length and to a certain degree to the thickness of diaphragm  $D_2$ . Longer test time interval should be produced by extending the expansion chamber length and for the sake of this time interval it will be advantageous to employ diaphragm  $D_2$  as thin as possible. However, excessively thin diaphragm might probably fail during the process of evacuation the driven chamber prior to each experiment.

The performance of a simple shock tube can easily be made by assuming that the gases in the driver and driven sections (denoted as gases "4" and "1" in Fig. 1c) to be ideal gases having constant specific heats and by assuming that the diaphragm plays no part in the processes once it has shattered and the 2-dimensional shock and rarefaction waves are formed immediately.

The parameters which determine the shock mach number or the flow mach number behind the shock are the pressure ratios across the driver and driven chambers, the specific gravities of the gases and the initial temperature of the gases.

The equations that determine the performance of a shock tube in terms of the above parameters are given in appendix I.

## 2.2 The Choice of the Driver Gas

It is the objective of this section to demonstrate the advantage of using different driver gases to get stronger shock wave at a specified pressure ratio. The equation which relates the shock strength to the tube parameters (i.e.,  $P_4/P_1$ ,  $a_4/a_1$ ,  $\gamma_4/\gamma_1$ ) has been derived in appendix I, namely equation 21. It could be proven using equation 21 that with air to air shock tube, the maximum theoretical shock mach number is only approximately 6. For this reason it is sometimes necessary to apply different gases to produce higher flow Mach number. Examining equation 21, it follows that to increase the flow mach number it is necessary to make the sound of speed ratio  $a_4/a_1$  as high as possible and to choose the driver gas with the molecular weight as small as possible. To demonstrate this phenomena we make use of equation 21 for three different types of gases namely air,

helium and hydrogen. Assume that both chambers are initially at  $T = 25^\circ\text{C}$  and the following are given

- For Air  $\gamma = 1.40$   
 $R = 0.287 \text{ kJ/Kg}^\circ\text{K}$
- For Helium  $\gamma = 1.67$   
 $R = 2.079 \text{ kJ/Kg}^\circ\text{K}$
- For Hydrogen  $\gamma = 1.41$   
 $R = 4.125 \text{ kJ/Kg}^\circ\text{K}$

The general equation for simple shock tube is

$$\left(\frac{a_4}{a_1}\right) \left(\frac{\gamma_1 + 1}{\gamma_4 - 1}\right) \left[1 - \left\{\left(\frac{2\gamma_1 M_s^2 - \gamma_1 - 1}{\gamma_1 + 1}\right) \left(\frac{P_1}{P_4}\right)\right\}^{\frac{\gamma_4 - 1}{2\gamma_4}}\right] = M_s - \frac{1}{M_s} \quad (21)$$

Substituting the data into the above equation, we obtain

For Air  $\frac{P_4}{P_1} = \frac{2.8 M_s^2 - 0.4}{2.4 \left[1 - \left(\frac{M_s - \frac{1}{M_s}}{6}\right)^7\right]}$

For Helium  $\frac{P_4}{P_1} = \frac{2.8 M_s^2 - 0.4}{2.4 \left[1 - \left(\frac{M_s - \frac{1}{M_s}}{10.53}\right)^5\right]}$

For Hydrogen  $\frac{P_4}{P_1} = \frac{2.8 M_s^2 - 0.4}{2.4 \left[1 - \left(\frac{M_s - \frac{1}{M_s}}{22.36}\right)^{6.9}\right]}$

Using the above three equations, every  $M_s$  will yield a required value of  $P_4/P_1$ . The corresponding graph of  $M_s$  versus  $P_4/P_1$  for three different gases is shown in Fig. 2. It clearly shows the advantages of using hydrogen and helium instead of air. However, the safety hazard of using hydrogen prohibit the use of this gas, hence throughout this experiment helium will be used as the driver fluid.

A further gain of shock strength can be achieved by increasing the sound of speed ratios, one way of accomplishing this is to heat the driver gas, as in the case of Combusted Ludweig Tube [7].

### 2.3 Two-Dimensional Analysis of Supersonic Flow Around an Airfoil

The exact solution of the supersonic flow inside the cascade passages is obtained by the method of characteristics. The full discussion of the method and the equations relating  $v$  and  $\theta$  for the case of steady two-dimensional, nonviscous, irrotational flow has been outlined in appendix II.

Given the blade surface coordinates, it would then be possible to draw the blade profile by joining these coordinate points by straight lines. Hence the blade surface consists of these small straight line 'segments'. The angle of incidence of each 'segment' to any flow direction could be figured out from its slope and is used to be the boundary condition to the wave diagram. Table 1 lists the coordinate points of the pressure and suction surface of the airfoil that was proposed by PWAC.

The flow Mach number and pressure upstream of the compressor cascade was obtained experimentally and the wave diagram of the supersonic flow across the cascade has been drawn for two different cases, one for zero angle of incidence and another one for 4 degrees angle of incidence. Unfortunately due to the advanced nature of the problem and the scope of the present research, it would be impossible to represent accurately the flow behaviour at the entrance vicinity of the cascade system. For this reason it would be appropriate to assume that we have a finite thickness airfoil. Accordingly this assumption will eliminate the blow shocks

which were observed, standing upstream of airfoils. Since the axial entrance flow Mach number in this case is greater than unity, this assumption will not lead to large errors, as was proven by [8]. Let us demonstrate the use of the method of characteristics to solve a two dimensional supersonic flow inside a series of compressor blades. Suppose we have two compressor blades in series as shown in Fig. 3a, oriented at a 4 degree angle of incidence to the incoming flow direction.

Knowing the Mach number and static pressure upstream of the system, we could represent the flow by a set of R and Q waves

$$M_{\text{upstream}} = 1.528$$

$$P_{\text{upstream}} = 12.82 \text{ Psi}$$

From isentropic flow table (appendix A of [9]), the total upstream pressure, i.e.  $P_{t1}$  was found to be 49.16 Psi.

With the help of Prandtl-Meyer table given in reference [9], it was found for  $M = 1.528$ , that  $\nu = 12.79$ .

Then

$$\begin{aligned} \text{Characteristic } Q &= \nu + \theta \\ &= 12.79 + (-23.65) \\ &= -10.86^\circ \end{aligned}$$

$$\begin{aligned} \text{Characteristic } R &= \nu - \theta \\ &= 12.79 - (-23.65) \\ &= +36.44^\circ \end{aligned}$$

Note that for convenience, the horizontal direction is set to be  $-23.65^\circ$  from positive x-axis (clockwise direction is negative).

These sets of characteristic waves could be drawn through the fact that Q and R characteristics are making angles of  $(\theta - \mu)$  and  $(\theta + \mu)$  to horizontal direction, respectively.

These characteristics could be used to 'simulate' the supersonic flow up to the entrance region of blade 1, where there is a sudden negative deflection angle of 2.2 degrees. Since we ignored the blade thickness there will be a simple Prandtl-Meyer expansion wave originating at the upstream end of the suction surface.

The flow properties behind the tail of these expansion waves would be found as follows (see Fig. 3a for location of the subscript numbers)

$$\begin{aligned} \nu_{21} &= 12.79^\circ \quad ; \text{ from Prandtl-Meyer table with} \\ & \quad M : 1.528 \end{aligned}$$

$$\begin{aligned} \nu_{32'} &= \nu_{21} + 2.2^\circ \\ &= 14.92^\circ \end{aligned}$$

$$\begin{aligned} M_{32'} &= 1.603 \quad ; \text{ from Prandtl-Meyer table with} \\ & \quad \nu_{32'} = 14.92 \end{aligned}$$

$$\mu_{32'} = 38.60^\circ$$

All other properties behind the expansion waves could be found by the help of isentropic flow table.

To find the flow properties of point 42, the boundary conditions given in table 1 will be used.

$$Q_{42} = Q_{32'} = -10.90^\circ$$

Point 42 falls on region (segment) 3 of the suction surface. Hence

$$\theta_{42} = 25.96 \quad ; \text{ from table 1}$$

Then

$$\begin{aligned}v_{42} &= -10.90 - \theta_{42} \\ &= -10.90 + 25.96 \\ &= 15.06^\circ\end{aligned}$$

$$\begin{aligned}R_{42} &= v_{42} - \theta_{42} \\ &= 15.06 + 25.96 \\ &= 41.02^\circ\end{aligned}$$

Properties of point 43 will be found as follows:

$$\begin{aligned}R_{43} &= (v - \theta)_{43} = R_{42} = 41.02 \\ Q_{43} &= (v + \theta)_{43} = Q_{33} = 10.90\end{aligned}$$

Solving these two equations simultaneously, all properties of point 43 could be found and are tabulated in table 2a.

In this fashion the wave diagram could be constructed mesh by mesh until the formation of the shock wave from the pressure surface, due to a sudden positive deflection of  $4^\circ$  (see table 1). All flow properties ahead of the shock are known, together with the known geometric deflection angle; they can be used to find flow properties behind the shock wave.

The intersection of the characteristic and shock wave could be constructed only by trial and error method. It is customary to assume the flow directions behind the shock and check the validity of the assumption using the boundary condition on the pressure surface.



However, this method is necessary only when the oblique shock present is a strong one, obviously this is not the case here. Furthermore the oblique shock, further downstream is weakened by the arrival of the expansion waves from suction surface. For this reason, it is assumed that R waves are constant across the shock. The Q waves behind the shock are found by trial and error method, if the assumed Q wave meets the intersection between R wave and the shock, we found the right value of Q. Otherwise vary Q until, R characteristic, the shock and Q characteristic intersect at one point. The slope of the shock further downstream is obtained by averaging Q characteristic before and after the shock, better value is obtained by averaging the above value with the one obtained from the next mesh.

$$R_{141} = R_{140}$$

Assume

$$Q_{141} = -18.80 ; \text{ between the values of } Q_{129} \text{ and } Q_{130}$$

It is found that the R wave of point 139, Q wave from point 141 and the average slope of the shock wave of point 128 and 129 coincided at one point. This condition implied that the assumed value of  $Q_{141}$  is the right choice.

Further point properties are to be found in table 2a and the wave diagram itself is shown in Fig. 3a. The pressure surface distribution along the suction and pressure surfaces were plotted in Fig. 26a. Similar wave diagram but for the case when the upper portion of the blade is oriented at  $0^\circ$  of incidence to the incoming flow direction, has been constructed, see Fig. 3b. The resulted pressure variation along both surfaces is shown in Fig. 27.

Detailed discussion of the results will be given in Chapter 4, where a comparison of the experimental results with the theoretical values obtained by method of characteristics and results provided to us by PWAC is presented.

#### 2.4 Process Occuring at the Shock Tube Exit

Fig. 4 demonstrates the diffraction process of the transmitted shock, where the shock wave originating at the location of the diaphragm travels radially outward creating a continuous pressure decrease at the centre of shock tube exit. The fluid particles upstream are given the messages about the presence of this low pressure region by means of expansion waves originating at downstream end with the head travelling back into the tube.

These waves of expansion interact with the reflected shock brought about when the incident shock hit the second diaphragm. The latter becomes weaker so that its propagation velocity decreases. The absolute propagation velocity becomes zero when the shock mach number becomes equal to that of the incoming supersonic flow (ahead of the shock); upon further weakening, the shock is no longer capable of advancing upstream and is swept downstream. Finally when it reaches the exit of the tube, the initial flow is reestablished.

It is necessary to find how far upstream does this disturbance (shock wave reflection) travels back into the tube and after what time interval is the initial flow reestablished.

These answers are crucial in the sense that the time interval of data acquisition is very limited and it is important that the initial supersonic flow has been recovered before the contact of discontinuity reaches the test section.

The examination could be made possible by constructing a wave diagram simulating the interaction between the shock wave and the expansion waves, from this it is possible to predict the net total experiment time available and hence the delay time given to the process, after the second diaphragm is shattered, the experiment data is acquired.

A wave diagram is constructed and the details are presented in Chapter 4.

#### 2.5 Different Methods of Obtaining Supersonic Flow Mach Number 1.53

There are several methods that could be used to obtain higher flow Mach number than that obtained by simple shock tube for the same initial pressure ratio.

One of the possibilities, illustrated in Fig. 5, is to employ two high pressure chambers 3 and 1 in series, constituting the driver sections with an initial pressure difference across the diaphragm. i.e.  $P_3/P_1$  and  $P_1/P_2$  are greater than 1. In operation, diaphragm  $D_1$  is burst by any convenient means whereupon resulting shock  $S_1$  moves into quiet gas (state 1) which is thus accelerated, heated and compressed into uniform state 5. Upon arrival of incident shock  $S_1$  to the location of diaphragm  $D_2$ . It is reflected, thus the driver gas (state 6) is further heated but, it also brought to rest, i.e.  $U_6 = 0$ .

After time delay  $t_d$ , the pressure at state 6 is large enough to break  $D_2$ , resulting shock  $S_2$  to move to driven chamber 2. The initial channel flow with shock  $S_2$  then resemble that of the conventional shock tube except that the driver state 6 is at increased temperature  $T_6 > T_2$ . The resulting mach number  $M_{s2}$  of shock  $S_2$  is greater than that obtained for single diaphragm operating at overall pressure ratio  $P_3/P_2$  and overall temperature ratio  $T_3/T_2 : 1$ .

Although this method sounds quite ready to be adapted; presently, it will not be employed for the following reasons. Its use of 2 driven chambers required much longer total tube length than square shock tube does, that in turn required longer lab space which we are not equipped with. Secondly, its different nature of construction from square tube, required different steps of debugging and types of preliminary testings from those already been done for the case of simple helium driven shock tube. Finally financial support limitation of the present stage will not tolerate us to consider such a complex design.

Fortunately a much simpler technique but produces only a slightly increase of flow Mach number could possibly be done by adjusting the simple shock tube driven chamber pressure in such a way to produce an underexpanded jet. Further discussion of this technique will be presented in Chapter 4.

### CHAPTER III

#### EXPERIMENTAL APPARATUS AND PROCEDURES

Preliminary tests were carried out during year one of the present two years project to determine the ability of a helium driven shock tube in providing uniform supersonic flow for few milliseconds and in visualizing the flow in the cascade passage. The shock tube used for this phase of the work was the 52 by 52 mm square shock tube.

##### 3.1 The 52 mm Square Shock Tube

The 52 mm square shock tube used in the preliminary testing was constructed from seamless structural steel tubing with a 6.35 mm wall thickness and consisted of a driver section of 1.524 m long followed by a driven section of 4.57 m long. Single mylar sheet of 0.50 mm thick was used, separating the helium in the driver section from the air in the driven section. Also a single mylar sheet of 0.0254 mm thick was used to separate the partially evacuated driven section from ambient conditions. The compressed helium in the driver section was supplied from a reusable helium cylinder while the driven section was kept to a vacuum pressure of 640 to 700 mm Hg. A schematic of the shock tube together with its facilities is shown in Fig. 6. The test section is located downstream of driven section, inserted firmly into the flange at the end of the shock tube. The design of this test section will be discussed thoroughly in section 3.4.

##### 3.2 The 15.25 cm Nominal Size Circular Shock Tube

The apparatus used to obtain the final results is the 15.25 cm nominal size circular cross section shock tube, which has bigger and longer dimensions than the square one, hence gives longer test time duration.

and provides larger area of uniform flow in the test section. This shock tube is constructed from a cylindrical 15.20 cm I.D. seamless steel pipe of 5.60 m long with 7.11 mm wall thickness. An additional 1.22 m long rectangular cross section (10.16 x 5.08 x 0.472 cm) tube has been added to the main tube. The design and function of this extension tube will be discussed in a later section.

The driver section consisted of 1.80 m long cylindrical cross section tube. The driven section similarly consisted of a 3.81 m long cylindrical cross section tube followed by 1.22 m long rectangular cross section aluminum tube. As discussed before, this driven section length is necessary to delay the arrival of the contact surface into the test section.

The test section, as Fig. 7 shows, is inserted firmly into the flange at the end of the extension rectangular tube. This insertion is necessary to ensure the alignment of the test section to the main tube and to prevent any flow leakage.

The shock tube was mounted on four supports, two for the driver and the other two for driven section. Each support consisted of an adjustable height roller mounted on a steel column. At the end of each section a 68 Kg forged steel slip-on flange was attached with full circumference weld and an O-ring groove was cut in the raised face of the flange.

Some cares were taken in the design of the shock tube as a vacuum system. The number of instrumentation access hole in the driven section was kept to a minimum. Neoprene O-ring seals were used on both flanges connecting the


driver to the driven sections and on the flange at the end of driven chamber to assume good grip on both sides of the diaphragm and to reduce any leakages. Vacuum grease was used on every connecting flange.

### 3.3 Design and Function of the Rectangular Cross Section Extension Tube

As it was mentioned in the preceding section, an extension of the shock tube driven section was needed because its optimal performance was based on a predetermined length.

The employed extension tube was manufactured from a rectangular cross section aluminum tube with good surface finish, to minimize any flow interference. The extension tube was connected to the main tube via an aluminum flange which was welded on the rectangular cross section tube at its mid-span.

The purpose of utilizing the two dimensional cross section tube was to convert the axisymmetric flow generated from the main tube by the rupture of the diaphragm into a two dimensional flow. The insertion of half of the rectangular tube into the cylindrical tube and the choice of its length was to ensure the recovery of the flow due to the extension tube inlet disturbance, before entering the test section. Both ends of this extension tube were carefully chamfered. For instance, the upstream end was chamfered from all sides to about  $5^\circ$  in order to minimize the flow disturbances at the inlet region. At downstream end, an aluminum flange was welded to serve as a clamping base for a second flange. These flanges were used to hold a thin diaphragm which isolate the air inside the driven chamber from ambient air. To prevent any leakage, an O-ring seal was installed on the base flange. A schematic view of the described extension tube is presented in Fig. 8.



### 3.4 Test Section

The test section used is located downstream of the driven section and consists of two parallel plexyglass windows inserted firmly into parallel aluminum plates. A number of secondary fasteners were located on the connection between the windows and the aluminum plates, to ensure the alignment of this connection, not to introduce any disturbances to the flow.

The plexyglass windows were used to allow the aerodynamic visualization of the events within the blades using Schlieren photography system.

The blades are held in positions by two pins on each side which are inserted in holes of the plexyglass windows so as to stay firmly in position. These windows were allowed to be rotated to vary the airfoil angle of incidence to the incoming flow direction. The two aluminum parallel plates were mounted on a horizontal aluminum base by means of screw fasteners and the whole test section was sitted on top of an adjustable stand which permit the test section movement longitudinally as well as vertically. The test section alignment to the main tube was done by inserting the parallel aluminum plates into two parallel groves at the end flange.

During the experiment the plexyglass windows were secured by clamps to prevent the expansion of the windows under loading. The described test section is shown in Fig. 9.

### 3.5 Schlieren System

Top view of the schlieren system is shown in Fig. 10.  $S_1$  is a continuous light source located in front of a condenser lens  $L_1$  and  $S_2$  is a spark light



source situated between  $L_1$  and  $L_2$ . Either light source produces an effective light source  $S_3$ , the size and shape of which are controlled by knife edge  $K_1$ .  $K_1$  has to be positioned at the focal point of a spherical mirror to  $M_1$  to give a parallel light beams, passing through the test section and shining on another spherical mirror  $M_2$ .

$M_2$  converges the light rays to the focal point  $S_4$ . Another knife-edge  $K_2$  is used to cut part of  $S_4$ , producing the schlieren effect, in such a way that only a certain fraction (often about half) of the light enters the camera.

Continuous and spark light sources are used. The continuous light is required for alignment and adjustment of the schlieren components and the spark light source supplies a light pulse of 5 to 10 microseconds for instantaneous photography of the flow phenomena.

The continuous light source is an air-cooled 100 watts concentrated Arc lamp connected to a (ENCO) power supply unit.

To obtain an effective light source, two optical condensers of 17.5 cm focal length are used. The two spherical mirror of 15 cm diameter (made by Unertl Optical Co., Pittsburgh) have 1.232 m focal point each. The plane square mirror of 5 cm wide, is used to fold the beams so as to give a compact arrangement. The knife-edge component for light interception consists of razor blades held in position by four screws and framed on a stand with sliding adjustment.

A polaroid MP-3 land camera, without lens is used to hold the polaroid film (type 47, ASA 3000). The camera sits on a stand which is adjustable for

setting the right distance between the film and the spherical mirror  $M_2$ , a critical requirement for obtaining a sharp photography.

The ratio of the size of the image on the photography plate to that of the object in the test section is defined as magnification factor,  $m$  [11]. This factor is given as the ratio of the distance to the image from mirror  $M_2$  and the distance to the object from mirror  $M_2$  which both could easily be calculated from the mirror formula. However, a simpler way of obtaining this number will be adapted here. A vernier with a specified opening is located at the test section, then  $m$  is simply the ratio of the image opening on the photography plate to the actual opening of the vernier. It is found the magnification factor for our case to be 0.52.

### 3.6 The Time-Delayed Spark System

Schlieren observation of nonstationary gas dynamics phenomena frequently requires the use of high intensity, short duration light source. This is practically applicable, in shock tube facilities where events are typically characterized by times of order microseconds. In addition, sequence photographs are often necessary for complete description of a particular phenomenon. Thus, some provision for high frequency multiple flashes is desirable. Alternately, if the events have a high degree of repeatability, the phenomenon can be reproduced and photographed many times with each successive photograph delayed relative to its predecessor to yield a time history of the events. This latter process will be made possible by employing the Time-Delayed spark unit.

The primary components of the apparatus are the trigger unit, the spark lamp and the time delay generator. They are coupled with a triggering device by various secondary units. A schematic of the entire system and approximate pulse voltage of the components is presented in Fig. 11.

The trigger circuit of the system consists of a piezoelectric pressure transducer (component 1 in Fig. 11) followed by a pulse amplifier (component 2) and a pulse generator (3) which serve two purposes. First, via a capacitive voltage divider, one pulse is sent to trigger an oscilloscope which is used for timing purpose and checking the accuracy of the unit when necessary, and another signal of sufficient amplitude is sent to trigger the delay generator (component 5).

In addition, the use of manual firing switch on the pulse generator (3) allows testing the rest of the system without the necessity of firing the shock tube, this feature is particularly advantageous for checking the alignment of the optical system.

The delay generator output voltage is amplified and used to trigger another pulse generator similar to that in the trigger circuit. Thus, after a specified time delay this unit generates a pulse amplitude of 400 volts, sufficient enough to trigger the spark unit (component 7). The spark unit which function as a light source for the schlieren optical system, controlled by a hydrogen thyratron tube acts as a switch. A positive pulse at the grid causes the thyratron to conduct and induce a spark to arc across a high voltage gap. Within the delay generator diagram, a manual switch allows selection of a 100 microseconds range delay or a 1000 microseconds delay. The

control furnished an actual delay range of 10 to 250 microseconds and 40 to 2200 microseconds, respectively.

This unit was tested and gave the desired high intensity light source for 5 to 10 microseconds which was found large enough for our schlieren system using pressure transducer of 1 microsecond rise time. Further details of each component could be obtained from [12].

### 3.7 Secondary Units

Several secondary units are necessary to support the other primary facilities. Vacuum was provided by a Balzers Vacuum pump (type DUO 5, ultimate pressure of 0.01 mm Hg). The vacuum pump was connected to the control panel by 1.90 cm I.D. copper tubing and via a rubber tubing of 1.27 cm I.D. to each chamber (driver and driven). The vacuum pressure in the driven section was measured by an MFG testing gauge range 0-760 mm Hg vacuum. The maximum error yielded was  $\pm 0.25\%$  of full scale. Another similar gauge was used for measuring the vacuum pressure in the driver section prior to the introduction of Helium into this chamber.

During the introduction of helium, supplied from reusable HP helium cylinder, the driver chamber pressure was measured by an Ascroft testing gauge, range 0-69 Bar.

Mylar plastic sheets of various thickness were used as diaphragm, whose thickness between the two chamber was selected experimentally according to the shock Mach number desired, whereas the second diaphragm at the end of driven chamber was chosen to be as thin as possible, so as to minimize the flow disturbance upon its rupture.

### 3.8 Experiment Procedure

All tests were performed using helium as driver fluid. For both tubes a diaphragm of 0.5 mm thickness was used separating the helium from the air in the driven section, a mylar sheet of 0.0254 mm thickness was used to separate the partially evacuated driven section from ambient.

In case of square shock tube the driven chamber was kept to a vacuum of 700 mm Hg (620 mm Hg for the case of cylindrical shock tube) and the driver section was slowly filled with helium until the diaphragm between the driver and driven chamber was suddenly ruptured. It was noticed that the driver chamber pressure at the instant of diaphragm rupture was  $830 \pm 14$  kPa for square tube and  $1120 \pm 14$  kPa for the case of cylindrical tube.

This procedure was found to give satisfactory results provided that the driver tube was filled with gas slowly enough. Prior to introduction of helium the air in the driver tube was first partially pumped out.

A pressure transducer was located downstream of the driven chamber, acting as a shock wave detector and depending on the type of data required, this transducer output could be used to trigger the schlieren system for photography visualization or could be used to trigger oscilloscope for pressure measurement.

#### 3.8.1 Pressure Measurement

All pressure measurements were performed using piezoelectric pressure transducer type 101A, with rise time of one microsecond and pressure range up to 100 psi, in group of two, as shown in Fig. 6 and 7.

The first pressure transducer was used to trigger the oscilloscope (TEKTRONIX, type 5D10) and the second one was connected to the input terminal of the oscilloscope vertical deflection plate. Then by knowing the transducer constant  $\Delta V/\Delta P$  (it is 32.2 mV/Psi for this case) and the oscilloscope voltage and time scale, the pressure behind the shock was easily computed from the oscilloscope pressure traces which were recorded on Polaroid film (Type 47, ASA 3000). Sample of pressure traces are shown in Fig. 12 and 13.

The Tektronix oscilloscope, type 5D10 was equipped with cursors which enable one to read directly the voltage difference from its screen. This feature is of great advantage, time wise, for searching the indicated pressure value from such a graph:

Pressure measurement along the blade surface was recorded by the same pressure transducer (type 101A) inserted firmly into one of the plexyglass window next to the blade surface.

### 3.8.2 Velocity Measurement

The velocity measurements were performed to determine the shock velocity along shock tube, as well as the flow velocity behind the incident shock.

In the first case, piezoelectric pressure transducers (type 101A, with rise time of one microsecond) were employed in groups of two, with the first pressure transducer used to trigger the oscilloscope and the second one connected to the input terminal of the oscilloscope

vertical deflection plate. Then by knowing the distance ( $\Delta x$ ) between the pressure transducers and the time scale of the oscilloscope, the shock velocity was easily computed from oscilloscope traces.

To measure the flow velocity in the compressor cascade passage, the photographs taken by time delayed spark schlieren optical system were employed.

From the corresponding picture various mach angles could be obtained. A flow mach number could be determined from each mach angle. Additional mach numbers could be induced by introducing small disturbances along the blade surface.

### 3.8.3 Flow Uniformity in the Test Section

The flow uniformity at various locations of the test section was investigated. This was carried out using a blunt body of revolution with a flat nose and a wedge located at various longitudinal and lateral positions in the test section.

For the case of wedge the procedure is outlined as follows. First, one measures the oblique shock wave angle ( $\beta$ ) from the corresponding schlieren picture, then knowing the geometry deflection angle ( $\phi$ ) and utilizing the oblique shock charts [13], the flow mach number is readily determined.

In the case of blunt body, the distance ( $\delta$ ) from the flat nose of the blunt body to outer edge of the yielded detached shock was

measured from schlieren pictures and knowing the blunt body diameter (d), the parameter ( $\delta/D$ ) could be determined. These parameters could be used to obtain the flow mach number from Fig. 4.15 of [14].

To investigate the time duration of constant flow uniformity in the test section, a pressure transducer is attached on to the tube wall downstream of driven chamber, from the pressure traces the duration of constant pressure is directly obtained.



CHAPTER IV  
EXPERIMENTAL RESULTS AND DISCUSSION

The performance of a helium driven shock tube and its capability for supersonic flow testing were first investigated using the 52 by 52 mm square shock tube. The experiments carried out here were mainly to determine the flow uniformity in the test section, the period of constant properties and finally the quality of the schlieren photographs which can be obtained using the existing 2-Kv time-delayed spark unit.

The testings of the actual compressor cascade system was however carried out with a comparatively larger shock tube namely the 15.25 cm nominal size cylindrical shock tube. The later tests were performed to determine the shock structure and surface pressure distribution within the compressor cascade passage at different pressure ratios and angles of incidence.

4.1 Performance of Helium-Driven Square Shock Tube

4.1.1 Flow Uniformity and Test Time Duration

The flow uniformity in the test section was examined via pressure measurements and spark schlieren photography. Pressure traces recorded downstream of the driven section is presented in Fig. 12 for the case of 700 mm Hg vacuum pressure. A constant pressure region is seen to prevail for a period of 0.6 msec corresponding to a driven section length 3.5 m. By extending this length to 4.57 m, the constant pressure duration was found to increase proportionally to about 1.0 msec as demonstrated by longer straight line portion in Fig. 13.

From the pressure traces displayed in Fig. 12 and 13, the transient process occurring at the open end can easily be deduced. Following the oscilloscope triggering, the pressure rises first because of the incident shock followed by a second jump due to the reflected shock. This pressure rise continues until the pressure is registered around 290 kPa, after which point the pressure attenuation behind the reflected shock is clearly seen due to diffraction of the transmitted shock at the open end.

This flow behaviour was found to agree with the theoretical analysis. Outlined in Section 2.4, in which the presence of low pressure region at the centre of tube exit represents the formation of expansion waves at the location of downstream diaphragm with its head moving into the main tube.

Now that the fluid properties leaving the shock tube are found to remain practically unchanged for a certain period of time, it is then necessary to determine the flow uniformity at various locations inside the test section. This was carried out using a blunt body of revolution with a flat nose, (see Fig. 14). The body was placed at various locations in the test section and the mach number variation was determined by measuring the stand off distance from the schlieren pictures and the use of the stand off distance versus mach number relationship given in Ref. [15]. The results are presented in Fig. 16, together with those obtained using a wedge of  $6^\circ$  included angle (see Fig. 15). The latter were obtained by measuring the oblique shock angles from corresponding schlieren pictures. The results

show that in the test section, there exist in longitudinal direction a supersonic flow of mach number 1.4, with no significant flow property variation. The flow uniformity in the lateral direction was also investigated experimentally using the wedge discussed previously. The results presented in Fig. 17, demonstrate the presence of uniform supersonic flow of mach number 1.4.

From the above investigation, the flow uniformity is therefore confirmed in both the longitudinal and the lateral directions. From the results presented thus far, it was concluded that a helium driven shock tube is an apparatus which could be used to provide uniform supersonic flow for a test time which depends on the length of the driven section and in testing supersonic flow in a compressor cascade passage.

#### 4.1.2 Data Acquisition Time Interval

The pressure trace of Fig. 13, revealed that a constant pressure exist for a period of 1.0 msec constant pressure interval. However, constant pressure does not necessarily mean constant flow properties since it does not specifically indicate which region the pressure is registered to. Note that, both regions 2 and 3 (Fig. 1c) have the same pressure although contain different fluid of different densities.

Ideally, the experiment time is the time interval between the arrival of incident shock wave and the arrival of contact surface to the downstream end. Unfortunately part of this time is used

for flow recovery from disturbances of shock wave reflection, hence limiting the experiment time to that of the difference between the former and the latter.

Neglecting entropy variations behind the weak reflected shock and using the open end pressure history given in Fig. 13, the wave diagram shown in Fig. 18 was constructed. It is seen from the x-t diagram that the greatest distance from the exit the disturbances of the shock could be felt is 2.15 cm and the initial flow is reestablished after a time 1.02 msec has elapsed since the diaphragm breakage.

Looking back into Fig. 13b, it was found that 1.02 msec time interval more or less equal to the time interval of the exponentially decay, that is the time after diaphragm shatter, it takes for the process to come to constant pressure condition.

Fig. 19 has been prepared to help us to find the experiment time. All the necessary calculations are presented in appendix III. For the case of square shock tube, the time interval between the arrival of the shock and the arrival of contact surface to the location of second diaphragm is 1.43 msec, thus giving us 0.41 msec to acquire experimental data.

From our knowledge thus far, it is then decided that the data were (will be) obtained at time delay of around 1.35 msec after the arrival of the first incident shock to the face of the detecting

pressure transducer, attached on the tube wall at the end of driven chamber. This delay gives us approximately 0.25 msec data acquisition time interval before the contact of discontinuity reaches the exit. This period was found large enough for the type of experiment, where events are cited in the order of microseconds.

#### 4.1.3. Flow Visualization and Shock Structure

The following tests, carried out using the square shock tube were for flow and shock position visualization, for a given set of blading. These blades were not compressor blades, but turbine blades provided to Concordia University by PWAC for use in preliminary stage of the actual investigation.

The first schlieren photograph is presented in Fig. 20a, for a single airfoil placed in a uniform supersonic flow of mach number 1.4. In this picture the oblique shocks and flow separation at the suction surface are clearly seen. In the schlieren photography of Fig. 20b, two blades were used and weak oblique shock waves are seen at the upstream ends of the cascade system. As a proof to the flow uniformity, the oblique shocks remain are straight until their arrival to the jet boundary. The contact of discontinuities at downstream end of each blade are clearly seen. By choking the flow at the downstream end, which is equivalent to an increase of pressure ratio, the upstream shock becomes detached as shown in Fig. 20c. In this case flow separation is seen to take place at an upstream position resulting from an increase of pressure gradient. A better design of choking the flow will be presented in a later section.

#### 4.1.4 Concluding Remarks Concerning the Tests Conducted Using the Square Shock Tube

From the pressure measurements downstream of the shock tube, which shows the existence as a constant pressure period in the order of a few milliseconds and from the resulting experimental flow mach numbers at several locations inside the test section which shows the presence of uniform flow, it is safe to conclude that a helium driven shock tube is an appropriate apparatus in providing uniform supersonic flow for few milliseconds. The schlieren pictures using a single and two blade systems shows clearly the shock shape and flow separation for different flow conditions and therefore the spark-delay system employed can then be used for latter studies in testing the actual compressor cascade system.

#### 4.2 Tests Conducted Using the 15.25 cm Nominal Size Cylindrical Shock Tube

The final tests were conducted using the cylindrical shock tube which have a larger test section and a longer driver section to provide a constant period longer than 1.0 msec.

The data acquisition time for this shock tube is calculated and the details presented in appendix III. This time period is found to be 0.56 msec. Then it is decided that the data will be taken at delay time of 1.40 msec, after the first incident shock hit the detecting pressure transducer, thus allowing a total time of 0.34 msec to record experimental data. This time interval should be plenty enough for the events to reach steady state.

#### 4.2.1. Flow Structure and Uniformity Inside the Test Section

To provide a supersonic flow mach number higher than 1.4 the driven chamber pressure is adjusted in such a way to provide a flow with a mach number of 1.4 at the shock tube exit plane but at a pressure slightly higher than the ambient pressure. This results in an underexpanded jet with a higher but constant flow mach number within a certain region (i.e. region abcd in Fig. 21). The compressor cascade systems was therefore placed in this region. The reflected waves from the jet boundary were practically eliminated by placing a plate parallel to the shock tube centerline and chamfered to an angle of  $6^\circ$  so that the shock wave formed is attached to the leading edge and do not effect significantly the flow under this plate.

The structure of the jet was investigated using a wedge with an included angle of  $6^\circ$  placed at different locations in the flow. The results were checked out later using piezoelectric pressure transducer mounted on one of the two side plates and placed at different locations in each region. The results obtained from the pressure measurements showed that the pressure of the shock tube exit is greater than ambient (region I), followed by ambient pressure in region II and little below ambient in region III.

The flow uniformity inside region abcd of Fig. 21 was examined by taking a photograph of a wedge with 6 degrees included angle exposed to supersonic flow under investigation. From corresponding schlieren pictures, the shock wave angles and hence the flow mach numbers could directly be obtained. Fig. 22a shows a series of

schlieren pictures taken during this experiment and the resulting flow mach number is presented in the following figure. It shows the presence of uniform supersonic flow of mach number 1.53.

#### 4.2.2 Shock Wave Structure Within the Cascade Passage at Different Pressure Ratios

Following PWAC specification, a three blade compressor cascade system was employed, to examine the flow behaviour and shock structure within the systems. As previously mentioned, the upper plate was placed to eliminate any reflected waves from the upper jet boundary so that the flow in the test region can be maintained at constant mach number.

To maintain the pressures at the downstream end of the three blade systems unaffected by ambient pressure two additional plates were placed parallel to the slipstreams which was observed in earlier tests, trailing behind the middle blade. The presence of those plates were necessary especially at higher pressure ratios where the pressure downstream of the cascade system is much higher than ambient pressure. Without the presence of these extension plates the downstream pressure registered will not indicate the actual one since it will be the pressure of mixture between downstream air with the surrounding. Note should be taken for the joint between the end of the blade and upstream end of the extension plate especially for lower ones, where just a small leak could cause the high pressure underneath to escape and disturb the flow in the passage.



A schlieren picture of the cascade exposed to supersonic flow of mach number 1.53 at  $4^\circ$  angle of incidence to the incoming flow direction is presented in Fig. 23. As noted, the flow in this case is everywhere supersonic, characterized by oblique shock present at the upstream end of the system due to  $4^\circ$  angle of incidence the pressure surface made with the incoming flow plus the blade thickness itself. The shocks at downstream end are produced from the interaction between the flow of the pressure surface with that of the suction one, where the low pressure regions from suction surface interacts with that of a higher one from pressure surface. This interaction is separated by a slipstream seen trailing the middle blade, to represent the existence of two different flow regions with the same pressure and flow direction. As they have passed through shocks of different strength. However, they have incurred different entropy increases, and hence the two regions have different flow velocity.

By choking the flow (i.e. decreasing the exit flow area by attaching grille at downstreams of the extension plate, as shown in Fig. 24) 8%, the trailing oblique shocks are observed to move upstream and flow separation takes place, just downstream of these shocks (see Fig. 25a). The earlier shock formations corresponds to the increase of pressure gradient because of the presence of the grille. By decreasing the exit area further (i.e. 10%) the downstream shock moves further upstream interacting with that formed at the upstream end of the pressure surface, see Fig. 25b.

An area reduction of 24% will result in strong oblique shock system standing off the cascade entrance as shown in Fig. 25c, the flow behind the strong oblique shock is therefore subsonic.

#### 4.2.3 Pressure Variation Along the Suction and Pressure Surface

A detailed pressure measurement was carried out using piezoelectric pressure transducer to determine its variation along the cascade system.

The measurement has been done for two different angles of incidences namely  $+4^\circ$  and  $0^\circ$ .

For the case of  $4^\circ$  angle of incidence the pressure variation along the surfaces of the blades have been determined for three different pressure ratios 1.3, 1.62 and 2.0, corresponding to no reduction of exit area, 8% reduction and 24% reduction, respectively.

For a pressure ratio of 1.3 the flow is everywhere supersonic, verified in the preceding section.

The pressure distribution for both surfaces is presented in Fig. 26a. On the suction surface side the pressure suddenly jumps from that of the upstream, according to the strength of shock waves present at the leading edge vicinity. Then it shows more or less constant pressure trend to the interval from 10% to 60% of the blade actual span, follows by monotonically pressure decrease due to the presence of a series of infinitesimally small surface convex turns.

Along the pressure surface, the pressure increase in the upstream portion is found higher than that of the suction surface because of stronger shock wave from positive 4 degree angles of incidence the upstream portion of pressure surface makes with the incoming flow direction. From then on the pressure is seen to continuously decrease even below that of the other surface indicating the arrival of a series of expansion waves from suction surface side.

The theoretical pressure distribution along both blade surfaces for supersonic case was obtained using method of Characteristics which is discussed briefly in appendix II. The solution procedure together with all the assumptions made to come to those solutions, shown in Fig. 26a, was outlined in Chapter 2. Another theoretical result was presented to Concordia University by PWAC. They are obtained using Time Dependent Finite Difference Scheme with Artificial Viscosities. Similar to our assumption the latter also ignored the presence of shock wave from the blade thickness. Unfortunately, the solution from PWAC corresponds to different pressure ratio from the ones we have. Despite the fact comparison still could be done within certain interval (explained later).

To certify the validity of experimental results for pressure ratio of 1.3, they will be compared with those obtained by Method of Characteristics. The visual comparison could be seen from Fig. 26a. It says along the suction surface, the experimental results follow the theoretical curve closely beyond 15% of the blade length whereas along pressure surface in the same interval, the experimental

results although follow the theoretical curve but indicate higher values. The latter could be explained as follows, the moderate strength shock wave at the entrance region, increase the pressure considerably which in turn keeps the experimental values along pressure surface high relative to theoretical ones which have eliminated the pressure increase due to blade thickness factor.

Within 15% of the blade length (from leading edge) the experimental results indicate much higher values than predicted theoretically. Obviously, no comparison could be made due to the improper analyzation of the flow within the entrance region.

The reliability of the experimental results were verified further by placing small disturbances along the blade surface. The experimental flow mach numbers and hence the pressures were then determined by measuring the mach angles from the corresponding schlieren picture. From Fig. 26a, it is seen that the results obtained from pressure transducer are acceptably close with those obtained by Mach wave techniques.

Fig. 26b displayed the experimental pressure curve from both pressure and suction surface for pressure ratio of 1.62, it shows that the downstream shock wave was moved to the point  $x/L = 0.9$ , instead of originating at the trailing edge as was found for the case of 1.3 pressure ratio. The shock formation is indicated by a sudden increase of pressure, i.e. for this case the pressure increase from 0.22 to 0.39.

The shock arrived on the pressure surface side at around  $x/L = 0.75$  (indicated also by a pressure jump), then reflected. The pressure behind this reflected shock is registered around 0.6.

For a pressure ratio of 2, strong shock waves formed at the blade leading edge and the pressure behind the shock, along pressure surface remains more or less constant at around 0.6 (corresponding to subsonic case). The suction surface pressure increased first because of the upstream shock wave, then remains constant until the arrival of the strong shock wave from the pressure surface, thus increasing the pressure to a higher value, see Fig. 26c.

One interesting phenomenon has been noticed for three cases discussed previously is the fact that the pressure variation from upstream end until the location of shock formation or arrival along the corresponding type of surface is more or less the same. Notice the following, along the suction surface, the pressure history shown in Fig. 26a from  $0 \leq x/L \leq 0.9$  is the same with the one shown in Fig. 26b and along pressure surface for  $0 \leq x/L \leq 0.75$  the pressure history shown in Fig. 26a is the same with the one displayed in Fig. 26b. Similar comparisons could be made utilizing any of the mentioned pressure and that shown in Fig. 26c. The above result could be used to support our argument that there exists a uniform flow region in the test section and the shock tube used possesses a fairly good repeatability behaviour.

In the next pressure measurements, the blades were oriented in such a way that the upstream portion of the suction surfaces were making  $0^\circ$  angle of incidence to the incoming flow direction.

A detailed surface pressure measurement was carried out for the case of 1.4 pressure ratio, corresponding to no reduction of exit area.

Theoretical analysis of supersonic flow for this case was obtained by method of Characteristics, as previously mentioned, the blade thickness contribution to shock formation was assumed absent for the sake of simplicity.

The comparison of the experimental results to that of theoretical ones was revealed in Fig. 27, as expected, in the region of  $0 \leq x/L \leq 0.15$ , the experimental results yielded higher pressure than theoretical ones. This pressure jump represents the presence of weak shocks at the entrance region. Beyond 15% of the actual span, the experimental results followed closely those obtained theoretically both on suction and pressure surfaces. The extremely closed agreement between these two results suggested us the fact that relatively weak shocks at the upstream ends did not effect the flow beyond 15% of the blade length.

The experimental results were further compared to the ones obtained by PWAC which were done for the case of  $0^\circ$  angle of incidence with pressure ratio of 1.64. However, as was proven in the preceding discussion, the pressure variations along blade surfaces oriented to the same angle of attack but different downstream to upstream pressure ratio are the same as long as it is upstream of downstream shocks.

Along the suction surface and beyond 15% of blade length, the experimental results followed closely to the pressure trends obtained by PWAC, except in the region beyond 95% of the blade actual span. This discrepancy could not possibly be explained because of my unfamiliarity to PWAC method of treating this problem

Along the pressure surface comparison could only be made for region bounded between  $0 \leq x/L \leq 0.55$  since a shock present at  $x/L = 0.55$ . A reliable comparison could be done only in the interval between  $0.15 \leq x/L \leq 0.55$ , where the two results agreed pretty well, see Fig. 28.

On both surfaces, no actual comparison could be made to check the validity of experimental results in the interval between  $0 \leq x/L \leq 0.15$ , since no accurate analytical representation has been done, to describe the real flow behaviour around the entrance region. For now we have to contend ourselves with the obtained experiment data which seems reliable as were proven throughout the comparison.

CHAPTER V  
CONCLUSION

The performance of helium driven shock tube was examined and tests were carried out on a compressor cascade system for different pressure ratios to determine the shock position as well as the pressure variation along the suction and pressure surfaces.

Within the scope of the present investigation, the main results are summarized and the following conclusions are drawn.

- (1) Helium driven shock tube could be used to provide uniform supersonic flow for a time period which depend on the length of driven section. For a driven section length of 4.5 m, the constant pressure period was found to prevail for one millisecond and the experiment time was found to be 0.41 msec. A longer experiment time interval of 0.56 msec was obtained for a driven section length of 5 m.
- (2) Within limited range, the uniform flow Mach number in the test section could easily be adjusted by varying the driver and driven chambers pressure. For a driver pressure of 830 kPa and driven pressure of 700 mm Hg, the flow Mach inside the test section is 1.4. Higher flow Mach number of 1.53 was provided by increasing the driven pressure to 620 mm Hg (with driver pressure of 1124 kPa), which in turn increases that of the



flow leaving the shock tube. Thus creating an underexpanded jet, giving a certain area of uniform supersonic flow at higher Mach number than 1.4.

- (3) The test section used was proven to be appropriate for the present state objective of the research. Its design allowed the elimination of wave reflections from the jet boundary. It provided a uniform supersonic flow region for a short but sufficient period of time and it permitted the rotation of the blade within itself to vary the incidence angle to the incoming flow direction. Finally the design provides a two dimensional movement, an essential requirement for adjusting and aligning of the test section with respect to the main tube.
- (4) Flow in the cascade passages could successfully be examined through commercial plexyglass windows via a 2-KV spark schlieren system. The photographs showed clearly the shock position, slipstream and flow separation. Testing the flow uniformity was achieved using the blunt body of revolution and wedge techniques.
- (5) Different pressure ratios across compressor cascade was accomplished by decreasing the exit flow area. For the case of 4 degree angle of incidence, with no area reduction the flow, within the cascade was everywhere supersonic, characterized by the presence of oblique shock waves at upstream and downstream ends. With an area reduction on 24% of the flow is everywhere subsonic except the upstream portion of the suction surface.

- (6) The piezoelectric pressure transducer was used to measure pressure variation, shock velocity as well as the uniform flow time interval (in terms of driven section length). Its fast rise time is surely an advantage for this type of experiment where events exist in the order of milliseconds.

In general, the present investigation has successfully achieved the stated objectives, to provide a short period of supersonic flow using helium driven shock tube and to analyze the flow behaviour within the compressor cascade passages using a 2-KV spark schlieren systems and piezoelectric pressure transducer.

Consideration for future work should include the construction of an "improved" shock tube design such as the one outlined in section 2.5. To eliminate the excessive noise, the present apparatus produced during the process, the test section for future design should be located inside the driven chamber, so that the whole process is isolated inside the pipe. The present method of mounting the diaphragms which are done by tightening and untightening of 12, 2.54 cm bolts for every single shock tube firing was not efficient and very time consuming. In the future, these bolts will be replaced by clamps to reduce the total testing time. Although the present 3 blades cascade system did provide us with the required information, in the future the cascade system should contain 5 or more air-foils to completely eliminate the ends effect. Finally, to prevent the expansion of the plexyglass windows, the present set up do, under loading,

the future size of the plexyglass windows should be reduced just enough for showing the cascade systems and for pressure measurements the whole window should be replaced by two aluminum plates.

REFERENCES

- [1] Kerrebrock, J.L., Epstein, A.H., Haines, D.M. and Thompkins, W.T., 'The M.I.T. Blowdown Compressor Facility', Transaction of the ASME, Journal of Engineering and Power, Vol. 96, October 1974.
- [2] Russel, D.A. Knoke, G.S. and Wai, J.C., 'Uniformity of Ludweig Tube Flows'.
- [3] Cook, W.J., 'Test Section Configuration for Aerodynamics Testing in Shock Tubes', Shock Tubes and Waves, Proceeding of the 12th International Symposium on Shock Tubes and Waves, Jerusalem, July 16-19, pp. 127-136, 1979.
- [4] Neemeh, R.A., 'Experimental Studies of Converging Cylindrical Shock Waves Produced by Area Contractions', Ph.D. Degree Thesis, McGill University, Montreal, 1976.
- [5] Wright, J.K., Shock Tubes, John Wiley & Sons Inc., New York, pp. 29, 1961.
- [6] Rudinger, G., 'Nonsteady Duct Flow: Wave Diagram Analysis', Dover Publication Inc., New York, pp. 134-141.
- [7] Russel, op. cit.
- [8] York, R.E. and Woodard, H.S., 'Supersonic Compressor Cascades: An Analysis of the Entrance Region Flow Field Containing Detached Shock Waves', Transaction of the ASME, Journal of Engineering for Power, Series A, Vol. 98, April 1976.
- [9] John, J.E.A., 'Gas Dynamics', Allyn and Bacon Inc., Toronto, pp. 353-356, 1969.
- [10] Ibid, pp. 368-371.

- [11] Wu, J.H.T. and Lee, J.H., 'A Simple Schlieren System', Private Collection.
- [12] Wu, J.H.T., Ostrowski, P.P. and Lee, P., 'Construction of a Time-Delayed Spark System', Tech Note No. 71, Department of Mechanical Engineering, McGill University, Montreal, 1971.
- [13] John, op. cit., pp. 364-367.
- [14] Liepman, op. cit., pp. 105.
- [15] Ibid.
- [16] Rudinger, op. cit., Chapter 3.
- [17] Ibid., pp. 243-272.
- [18] Liepman, op. cit., pp. 284.
- [19] Shapiro, A.H., 'The Dynamics and Thermodynamics of Compressible Fluid Flow', The Ronald Press Company, New York, 1953 for Vol. I and 1954 for Vol. II.
- [20] Ibid.
- [21] Cook, W.J., Presley, L.L. and Chapman, G.T., 'Shock Tube as a Device for Testing Transonic Airfoils at High Reynolds Numbers', AIAA Journal; Vol. 17, No. 7, pp. 714-720, July 1979.
- [22] Epstein, A.H., Kerrebrock, J.L. and Thompkins, W.T., 'Shock Structures in Transonic Compressor Rotors', AIAA Journal, Vol. 17, pp. 355-379, April 1979.
- [23] Garen, W. and Lensch, G., 'The Double Shock Wave Tube: Experimental Investigation of Shock Reflections', Shock Tubes and Waves, Proceeding of the 12th International Symposium on Shock Tubes and Waves, Jerusalem, July 16-19, 1979.
- [24] Gordon Hall, J., Shock Tubes; Part II, Production of Strong Shock Waves, Shock Tube Applications, Design, and Instrumentation, Institute of Aerophysics, University of Toronto, May 1958.

- [25] Hawthorne, W.R., 'Aerodynamics of Turbines and Compressors; High Speed Aerodynamics and Jet Propulsion, Vol. 10, Princeton University Press, Princeton, 1964.
- [26] Kerrebrock, J.L., 'Flow in Transonic Compressors', AIAA Journal, Vol. 19, No. 1, pp. 4-19, January 1981.
- [27] Ladenburg, R.W., Lewis, B., Pease, R.N. and Taylor, H.S., Physical Measurement in Gas Dynamics and Combustion', High Speed Aerodynamics and Jet Propulsion, Vol. 9, Princeton University Press, Princeton, 1954.
- [28] McDonald, P.W., Bolt, C.R., 'A Comparison Between Measured and Computed Flow Fields in a Transonic Compressor Rotor' ASME Paper, 1980.
- [29] Merzkirch, W.F., 'A Simple Schlieren Interferometer System, AIAA Journal, October 1965.
- [30] Owczarek, J.A., 'Fundamentals of Gas Dynamics', International Textbook Company, Scranton, Pennsylvania, 1964.
- [31] Vasil'ev, L.A., 'Schlieren Methods', Translated by A. Baruch, Israel Program for Scientific Translation, New York, 1971.
- [32] Weinberg, F.J., Optics of Flames, Butterworths, London, 1963.
- [33] Zeitoun, D., Brun, R. and Valette, M.J., 'Shock-Tube Flow Computation Including the Diaphragm and Boundary-Layer Effects', Shock Tube and waves, Proceeding of the 12th International Symposium on Shock Tubes and Waves, Jerusalem, July 16-19, 1979.

**APPENDIX I : DERIVATION OF THE SHOCK  
TUBE EQUATIONS**

When the diaphragm across the high pressure and low pressure chambers was suddenly bursted the high pressure gas expands and compresses the gas in the low pressure chamber, hence the wave patterns like the one in Fig. 1c resulted.

Assuming no diffusion process, the region 2 of Fig. 1c contains air and region 3 contains helium. Regions 2 and 3 have different densities and temperatures. To separate these regions a contact of discontinuities exists as shown by the dotted line. It is obvious from the nature of the contact of discontinuities that the velocity and pressure across it must be the same (i.e.  $u_2 = u_3$  and  $p_2 = p_3$ ).

Referring to the wave diagram shown in Fig. 1c, one could see that basically there are three relations which could be used to determine the properties of each region, namely relations across shock wave, across expansion waves and across the contact surface.

The relation across the shock wave will be discussed as follows:

Consider a moving shock wave with a velocity  $u_s$  relative to the still air ahead of it (see Fig. a), now consider the same moving shock

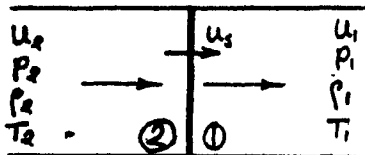


Fig. a. Moving Shock

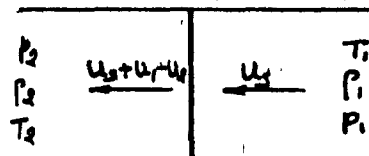


Fig. b. Stationary Shock



with an observer moving at the shock velocity. The shock is now fixed with respect to the observer (Fig. b).

For the case of one dimensional flow;

the continuity equations gives  $\rho_1 u_s = \rho_2 (u_s + u_1 - u_2)$  (1)

The momentum equation yields

$$p_1 A_1 - p_2 A_2 = \rho_1 A_1 u_s^2 - \rho_2 A_2 (u_s + u_1 - u_2)^2$$

Since  $A_1 = A_2$

$$p_1 - p_2 = \rho_1 u_s^2 - \rho_2 (u_s + u_1 - u_2)^2$$
 (2)

The energy equation yields

$$c_p T_1 + \frac{u_s^2}{2} = c_p T_2 + \frac{(u_s + u_1 - u_2)^2}{2}$$
 (3)

The speed of sound is given by

$$a^2 = \gamma RT = \gamma \frac{p}{\rho} \quad (\text{for ideal gas})$$

hence

$$p = \rho \frac{a^2}{\gamma} = \rho RT$$
 (4)

Combining equations (2) and (4), one obtains

$$\rho_1 \frac{a_1^2}{\gamma_1} - \rho_2 \frac{a_2^2}{\gamma_2} = \rho_1 u_s^2 - \rho_2 (u_s + u_1 - u_2)^2$$

Rearranging

$$\frac{\rho_1}{\rho_2} - \frac{a_2^2}{a_1^2} = \frac{\gamma_1 u_s}{a_1^2} [u_s + u_1 - u_2] + \frac{\gamma_1}{a_1^2} [-u_s + (u_2 - u_1)]^2$$

Combining the above equation with equation (1)

$$\left(\frac{a_2}{a_1}\right)^2 = \frac{u_s - (u_2 - u_1)}{u_s} + \frac{\gamma_1}{a_1^2} [u_s - (u_2 - u_1)](u_2 - u_1) \quad (5a)$$

$$\text{or } a_2^2 = \frac{u_s - (u_2 - u_1)}{u_s} a_1^2 + \gamma_1 [u_s - (u_2 - u_1)](u_2 - u_1) \quad (5b)$$

Note that for ideal gas  $C_p = \frac{\gamma R}{\gamma - 1}$

Using this equation and equation (4)

$$C_p(T_1 - T_2) = \frac{a_1^2 - a_2^2}{\gamma_1 - 1}$$

Then equation (3) can be written as

$$\frac{a_1^2 - a_2^2}{\gamma_1 - 1} = -\frac{u_s^2}{2} + \frac{1}{2} [u_s^2 + 2u_s(u_1 - u_2) + (u_1 - u_2)^2]$$

$$\text{or } u_s(u_1 - u_2) = \frac{(u_1 - u_2)^2}{2} - \frac{(a_1^2 - a_2^2)}{\gamma_1 - 1} \quad (6)$$

Thus

$$\left(\frac{dx}{dt_s}\right)^2 = u_1 + u_s = \frac{u_1 + u_2}{2} + \frac{a_1^2 - a_2^2}{(\gamma_1 - 1)(u_1 - u_2)} \quad (7)$$

$$\text{and } \left(\frac{a_2}{a_1}\right)^2 = 1 - \frac{(\gamma_1 - 1)(u_1 - u_2)}{a_1^2} \left[u_1 + u_s \cdot \frac{(u_1 - u_2)}{2}\right] \quad (8)$$

Substituting equation (5b) into (6) and after simplification

$$\frac{u_2 - u_1}{a_1} = \frac{2}{\gamma_1 + 1} \left[ \frac{u_s}{a_1} - \frac{a_1}{u_s} \right] \quad (9a)$$

$$\text{or } \frac{u_2 - u_1}{a_1} = \frac{2}{\gamma_1 + 1} \left[ M_s - \frac{1}{M_s} \right] \quad (9a)$$

since  $u_1 = 0$

$$\frac{u_2}{a_1} = \frac{2}{\gamma_1 + 1} \left[ M_s^2 - \frac{1}{M_s} \right] \quad (9b)$$

Substitution of equation (9a) into equation (8) and after simplification yields the temperature ratio across the shock.

$$\frac{T_2}{T_1} = 1 + \frac{2(\gamma_1 - 1)}{(\gamma_1 + 1)^2} \left[ \left( \frac{u_s}{a_1} \right)^2 - 1 \right] \left[ \gamma_1 + \left( \frac{a_1}{u_s} \right)^2 \right] \quad (10)$$

Density ratio across shock wave can be obtained by combining equations (1) and (9a).

$$\frac{\rho_2}{\rho_1} = \frac{\gamma + 1}{(\gamma - 1) + 2 \left( \frac{a_1}{u_s} \right)^2} \quad (11)$$

The pressure ratio across the shock is given

$$\frac{p_2}{p_1} = \frac{\rho_2}{\rho_1} \times \frac{T_2}{T_1}$$

Multiplying eqn (11) with eqn (10) yields the pressure ratio across the shock wave

$$\frac{p_2}{p_1} = 1 + \frac{2\gamma_1}{\gamma_1 + 1} \left[ \left( \frac{u_s}{a_1} \right)^2 - 1 \right]$$

$$\text{or } \frac{p_2}{p_1} = 1 + \frac{2\gamma_1}{\gamma_1 + 1} \left[ M_s^2 - 1 \right] \quad (12a)$$

Rearranging eqn (12a), we obtain

$$\left( \frac{u_s}{a_1} \right)^2 = M_s^2 = \frac{(\gamma_1 - 1) + \frac{p_2}{p_1} (\gamma_1 + 1)}{2\gamma_1} \quad (12b)$$

and substituting into eqn (10) yields the temperature ratio in terms of pressure ratio

$$\frac{T_2}{T_1} = \left( \frac{a_2}{a_1} \right)^2 = \frac{\frac{p_2}{p_1} + \frac{\gamma_1 + 1}{\gamma_1 - 1}}{\frac{\gamma_1 + 1}{\gamma_1 - 1} + \frac{p_1}{p_2}} \quad (13)$$

The equations derived so far enables us to determine completely the flow properties behind the shock wave given the flow conditions ahead of it.

To find the relations of flow properties across the expansion waves, the method of characteristics for one dimensional unsteady flow will be employed. Further discussions of this method was discussed in detail by Ref [16] in Chapter 3.

The R and Q characteristics are defined as follows: Along R characteristics of slope  $\frac{dx}{dt} = U + a$

$$\frac{2}{\gamma - 1} a + U = \text{Constant.}$$

Along Q characteristics of slope  $\frac{dx}{dt} = U - a$

$$\frac{2}{\gamma - 1} a - U = \text{constant}$$

Between regions 3 and 4 of Fig. 1c, the characteristic R will be maintained constant (assuming direction of U is possible to the right)

Then

$$R_3 = R_4$$

$$\text{or } u_3 + \frac{2}{\gamma_3 - 1} a_3 = u_4 + \frac{2}{\gamma_4 - 1} a_4 \quad (14)$$

but  $u_4 = 0$  and  $\gamma_3 = \gamma_4$

hence

$$u_3 = \frac{2}{\gamma_4 - 1} [a_4 - a_3]$$

Applying the condition across the contact surface (i.e.  $u_2 = u_3$  and  $P_2 = P_3$ ) and keeping in mind that  $u_1 = 0$ , we can combine eqn (9a) and eqn (15) to yield

$$\frac{2}{\gamma_4 - 1} [a_4 - a_3] = \frac{2a_1}{\gamma_1 + 1} (M_s - \frac{1}{M_s})$$

$$\text{or } \frac{2a_4}{\gamma_4 - 1} [1 - \frac{a_3}{a_4}] = \frac{2a_1}{\gamma_1 + 1} (M_s - \frac{1}{M_s}) \quad (16)$$

From isentropic relation across expansion waves

$$\frac{a_3}{a_4} = \left( \frac{P_3}{P_4} \right)^{\frac{\gamma_4 - 1}{2\gamma_4}} \quad (17)$$

where

$$\frac{P_3}{P_4} = \frac{P_2}{P_1} \times \frac{P_1}{P_4}, \quad \text{since } P_2 = P_3 \quad (18)$$

Substituting eqn (12a) into eqn (18)

$$\frac{P_3}{P_4} = \frac{2\gamma_1 M_s^2 - (\gamma_1 - 1)}{\gamma_1 + 1} \times \frac{P_1}{P_4} \quad (19)$$

Substitution into eqn (17)

$$\frac{a_3}{a_4} = \left[ \frac{2\gamma_1 M_s^2 - (\gamma_1 - 1)}{\gamma_1 + 1} \times \frac{P_1}{P_4} \right]^{\frac{\gamma_4 - 1}{2\gamma_4}} \quad (20)$$

Combining eqn (16) with eqn (20) yields

$$\frac{a_4}{a_1} \left( \frac{\gamma_1 + 1}{\gamma_4 - 1} \right) = \left[ 1 - \left\{ \frac{(2\gamma_1 M_s^2 + (\gamma_1 - 1))}{\gamma_1 + 1} \times \left( \frac{P_1}{P_4} \right)^{\frac{\gamma_4 - 1}{2\gamma_4}} \right\} \right] = M_s - \frac{1}{M_s} \quad (21)$$

Equation (21) enables us to determine the shock mach number for a given pressure ratio or vice versa. To find the flow mach number, we use table 1 of [17] for a given shock mach number, to obtain the value of  $\frac{|\Delta u|}{a}$  and  $\frac{a'}{a}$ , dividing the above we obtain an expression of  $\frac{|\Delta u|}{a'}$ . this quantity represents the flow mach number behind the shock.

Determination of flow properties (i.e. u, a) in each region in Fig. 1c.

### REGION 2

Knowing the pressure ratios between regions 4 and 1 and using eqn (21), one finds the shock mach number. To solve eqn (21) it is best done by trial and error method.

From the shock table for the known shock mach number, we obtained accordingly

$$i) \quad \frac{|\Delta u|}{a} = \frac{|u_2 - u_1|}{a_1} = \frac{u_2}{a_1}$$

$$ii) \quad \frac{a'}{a} = \frac{a_2}{a_1}$$

$$iii) \quad \Delta s = s_2 - s_1$$

The flow properties of region 1 are known hence the above quantities are enough to calculate properties in region 2.

REGION 3

Gas properties in region 3 could be related to gas properties in region (4) by R characteristics

$$u_3 + \frac{2}{\gamma_4 - 1} a_3 = u_4 + \frac{2}{\gamma_4 - 1} a_4$$

Keeping in mind that  $u_2 = u_3$ . We can determine the value of  $a_3$  by the above equation.

REGION 5

Knowing that the velocity ahead of the shock is zero (i.e.  $u_5 = 0$ ), the properties in Region 5 could be determined by the help of the shock wave table. However as could be seen experimentally before attaining a pressure predicted by shock table. The diaphragm downstream of driven section has already shattered, followed by expansion to bring down the high pressure to that of the outside. Due to the advanced nature of this pressure variation, the pressure history will be based on experiment, as shown in Fig. 13.

APPENDIX II : Spacial 2-D Supersonic  
Irrotational Flow



The full nonlinear equation of motion for two dimensional nonviscous, irrotational steady flow are [18]

$$(u^2 - a^2) \frac{\partial u}{\partial x} + uv \left( \frac{\partial u}{\partial y} + \frac{\partial v}{\partial x} \right) + (v^2 - a^2) \frac{\partial v}{\partial y} = 0 \quad (22)$$

$$\frac{\partial v}{\partial x} - \frac{\partial u}{\partial y} = 0$$

For the case of Supersonic flow, or when

$$\frac{(u^2 + v^2)}{a^2} > 1$$

equation (22) is of hyperbolic type and the numerical solution can be obtained by the method of characteristics. This method provides an exact solution of the above equation and has the advantage of further insight into the structure of supersonic flow.

The distinguishing property of hyperbolic equation is the present of the characteristic lines in the x,y plane. On the characteristic lines, defined as lines on which there exists a discontinuity of velocity gradient, then as long as the velocity itself is continuous, it is possible to simulate different flows together at these lines.

On the characteristics, the dependent variables (u,v) satisfy a certain compatibility relation, which can be used as the method of computation.

#### The Method of Characteristics

In natural coordinate system, the equation of motion can be summarized as follows [19]

continuity :  $\rho u \cdot \Delta n = \text{const}$  (23)

momentum :  $\rho u \frac{\partial u}{\partial s} = - \frac{\partial p}{\partial s}$  (24)

irrotationality :  $\frac{\partial u}{\partial \eta} - u \frac{\partial \theta}{\partial s} = 0$  (25)

isentropic relation :  $\frac{\rho}{\rho_0} = \left( \frac{p}{p_0} \right)^{\gamma}$  (26)

Taking the natural log of continuity equation and differentiating with respect to  $s$  yields

$$\frac{1}{\rho} \frac{\partial \rho}{\partial s} + \frac{1}{u} \frac{\partial u}{\partial s} + \frac{1}{\Delta \eta} \frac{\partial \Delta \eta}{\partial s} = 0 \quad (27)$$

The mesh of flow for two dimensional case can be represented by the stream lines and normal to them as shown in Fig. c. From this mesh figure the change in angle  $\Delta \theta$  is represented by

$$\Delta \theta = \frac{\partial \Delta \eta}{\partial s}$$

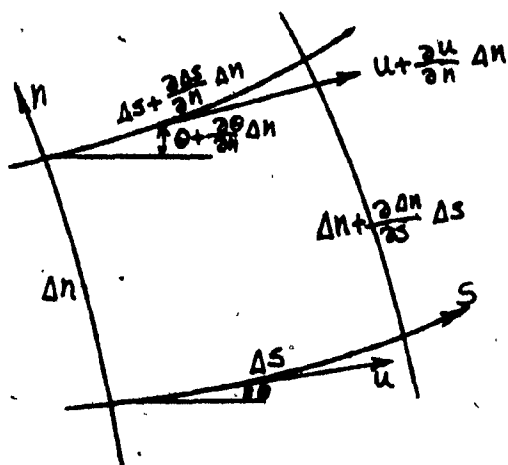


Fig. c. Flow Mesh

Substitution into eqn (27)

$$\frac{1}{\rho} \frac{\partial \rho}{\partial s} + \frac{1}{u} \frac{\partial u}{\partial s} - \frac{\partial \theta}{\partial \eta} = 0 \quad (28)$$

For ideal gas, equation (26) can be written as

$$a^2 = \frac{dp}{\rho} = \frac{\gamma p}{\rho}$$

Combining with equation (24)

$$u \frac{\partial u}{\partial s} = - \frac{a^2}{\rho} \frac{\partial \rho}{\partial s} \quad (29)$$

Combining with eqn (27) and after arranging

$$\left( \frac{u^2}{a^2} - 1 \right) \frac{1}{u} \frac{\partial u}{\partial s} - \frac{\partial \theta}{\partial \eta} = 0 \quad (30)$$

Now, let us imagine that a supersonic flow turns through a negative angle  $d\eta$ , see Fig. d. Equating  $u_t$  of region 1 and region 2 of Fig. d yields

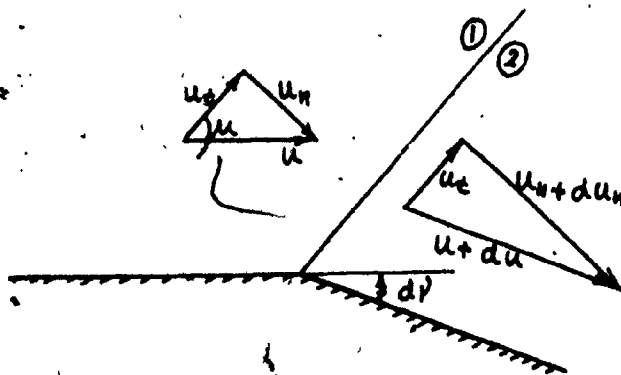


Fig. d. Flow Expansion

$$\begin{aligned} u \cos \mu &= (u + du) \cos (\mu + d\mu) \\ &= (u + du)(\cos \mu \cos d\mu - \sin \mu \sin d\mu) \end{aligned} \quad (31)$$

Since  $d\nu$  is a small angle then

$$\cos d\nu \rightarrow 1$$

$$\sin d\nu \rightarrow 0$$

therefore

$$u \cos \mu = (u + du) (\cos \mu - \sin \mu d\nu) \quad (32)$$

expanding and ignoring the second order terms, we get

$$\frac{du}{u} = \tan \mu d\nu$$

Since  $\sin \mu = \frac{1}{M}$ , it follows then

$$\tan \mu = \frac{1}{\sqrt{M^2 - 1}}$$

or 
$$\frac{du}{u} = \frac{1}{\sqrt{M^2 - 1}} d\nu \quad (33)$$

Combining eqn (33) with eqn (30)

$$\frac{\partial \nu}{\partial s} - \tan \mu \frac{\partial \theta}{\partial n} = 0 \quad (34)$$

Combining eqn (33) with eqn (25)

$$\tan \mu \frac{\partial \nu}{\partial n} - \frac{\partial \theta}{\partial s} = 0 \quad (35)$$

The compatibility relations are to be found from equations 34 and 35, relating the sets of characteristics direction (Q, R) with the stream line coordinate system (s, n) based on the fact that the mach lines are inclined at angles of  $\pm \mu$  to the stream lines, see Fig. e. Adding and subtracting eqn 34 and 35 yields eqn 36 and 37 respectively.

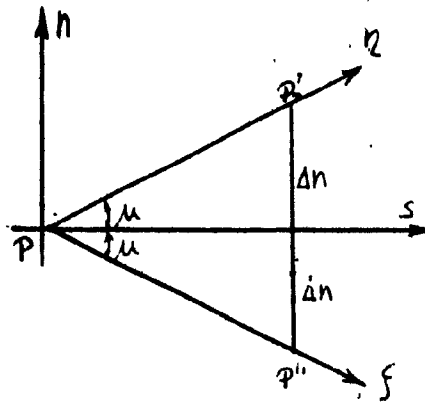
$$\frac{\partial}{\partial s} (v - \theta) + \tan \mu \frac{\partial}{\partial \eta} (v - \theta) = 0 \quad (36)$$

$$\frac{\partial}{\partial s} (v + \theta) - \tan \mu \frac{\partial}{\partial \eta} (v + \theta) = 0 \quad (37)$$

then

$$\frac{\partial}{\partial \eta} (v - \theta) = 0$$

$$\frac{\partial}{\partial \xi} (v + \theta) = 0$$



hence there exists a compatible relation between  $v$  and  $\theta$  for the case of steady two dimensional, nonviscous and irrotational supersonic flow. These relations are simply

$$v - \theta = R ; \text{ Constant along } \eta - \text{ coordinate} \quad (38)$$

$$v + \theta = Q ; \text{ Constant along } \xi - \text{ coordinate} \quad (39)$$

These compatibility relations will be used to simulate the supersonic flow in the compressor cascade. Further discussion of the method of characteristic could be found in Ref [20].

Calculation Procedure

The following section will be used to demonstrate how the method of characteristics can be used to solve for a two-dimensional flow field. Suppose along a data curve MN, the data or boundary conditions (i.e. velocity, direction, pressure, etc.) are given and it is required to find the conditions at an arbitrary point P. Through point P there are two characteristics. One of Q-type and another of R-type, which intersect the data curve on A and B respectively. Since both of these two points lie on the data curve,  $v$  and  $\theta$  can be found, so that the characteristics values of R and Q can be calculated from equations 38 and 39 respectively. The method of computation is illustrated in Fig. f, it follows that at p.

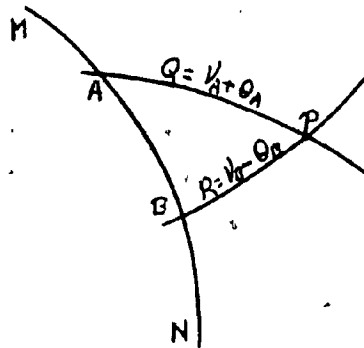


Fig.f. Characteristic Network For Wave Diagram Computation.

$$Q_P = Q_A$$

$$R_P = R_B$$

or 
$$v_P + \theta_P = v_A + \theta_A$$

$$v_P - \theta_P = v_B + \theta_B$$

Solving these two last equations simultaneously it is found that

$$v_p = \frac{1}{2} (v_A + v_B) + \frac{1}{2} (\theta_A - \theta_B)$$

$$\theta_p = \frac{1}{2} (v_A - v_B) + \frac{1}{2} (\theta_A + \theta_B)$$

Up to this point, the conditions of point p are known but not its position. Since mach number varies throughout the flow field, the characteristic lines AP and BP are not necessarily straight but rather are curved. However, if the size of the mesh is kept small enough, the characteristics AP and BP can be approximated by straight line inclined at the mach angle to the flow direction. Obviously the accuracy of this procedure depends on the mesh size, the smaller the mesh, the more accurate the solution.

**APPENDIX III: Process Occuring Inside  
Driven Section**



Specifications given (for 52 x 52 mm square shock tube)

Note: For subscripts see Fig. 1.

Driver Section

Helium

$$p_4 = 827.40 \text{ kPa}$$

$$\gamma_4 = 1.67$$

$$R_4 = 2.080 \text{ kJ/kg } ^\circ\text{K}$$

Driven Section

Air

$$p_1 = 14 \text{ kPa}$$

$$\gamma_1 = 1.40$$

$$R_1 = 0.290 \text{ kJ/kg } ^\circ\text{K}$$

Assume that both chambers are initially at ambient temperature, that are  $T_1$  and  $T_4 = 25^\circ\text{C} = 298 \text{ } ^\circ\text{K}$ .

$$\begin{aligned} \text{Hence } a_1 &= \sqrt{\gamma_1 R_1 T_1} = \sqrt{1.4 \times 290 \times 298} \\ &= 350 \text{ m/sec} \end{aligned}$$

$$\begin{aligned} a_4 &= \sqrt{\gamma_4 R_4 T_4} = \sqrt{1.67 \times 2080 \times 289} \\ &= 1016.5 \text{ m/sec} \end{aligned}$$

$$\text{So } \frac{a_4}{a_1} = \frac{1016.5}{350} = 2.95$$

Substituting the data into eqn 21 and corresponding to  $p_4/p_1 = 60$ , the shock mach number  $M_s$  is found to be 3.25.

Using  $M_s = 3.25$  and table 1a (shock wave table) of Rudinger,

$$\frac{u_2 - u_1}{a_1} = 2.422 \quad u_2 = 838.1 \text{ m/sec}$$

$$\frac{a_2}{a_1} = 1.716 \quad a_2 = 593.80 \text{ m/sec}$$

$$\frac{p_2}{p_1} = 11.91 \quad p_2 = 95.32 \text{ kPa}$$

now  $u_5 = 0 \quad \frac{u_2 - u_5}{a_2} = \frac{838.1}{593.8} = 1.14$

From shock wave table, it is found that

$$M_s \text{ (reflection)} = 2.155$$

$$\frac{a_5}{a_2} = 1.348 \quad a_5 = 800.44 \text{ m/sec}$$

$$\frac{p_5}{p_2} = 5.25 \quad p_5 = 8.75.40 \text{ kPa}$$

However, from experiment results given in Fig. 13, it has been shown that  $p_5$  never reached to 875 kPa. Instead it was shown that the downstream thin diaphragm breaks at a pressure of about 275 kPa. To represent the reality we will use experiment values to predict experiment time interval.

Then

$$\frac{p_5}{p_2} = \frac{275}{95.32} = 2.885$$

From shock wave table corresponding to the above pressure ratio it is found that

$$(M_s) \text{ reflected} = 1.618$$

$$\frac{a_5}{a_2} = 1.183 \quad \text{or } a_5 \cong 702.5 \text{ m/sec}$$

The shock speed is  $3.25 \times 350 \text{ m/sec} = 1138 \text{ m/sec}$ . It is known for the square shock tube, which has driven section of 4.57 m that the time for incident shock to reach the exit is

$$\frac{4.57}{1138} \times 1000 \text{ msec} = 4.02 \text{ msec}$$

and the time for contact surface to reach to the same point is

$$\frac{4.57}{838} \times 1000 \text{ msec} = 5.45 \text{ msec}$$

In section 4.1.2 it has been shown that the flow disturbance from shock wave reflection is recovered in a time period of 1.02 msec.

According to definition, given in section 2.4, therefore, the net data acquisition time is  $(5.45 - 4.02 - 1.02) = 0.41$  msec. This time is shown schematically in Fig. 19.

For the case of cylindrical shock tube, though the initial pressure of driven section is set higher than the one in the square tube, the incident shock mach number is the same for both cases. Due to the fact that the diaphragm separating helium in driver chamber from air in driven section have the same thickness and the reflected shock strength could be taken from the former case since diaphragm  $D_2$  is the same for both cases.

Then for calculation of experiment time period data could be obtained from previous case. However, for this tube, the driven section length is 5.032 m.

The time for incident shock to reach downstream end is  $\frac{5.032}{1138} \times 1000 \text{ msec} = 4.42$  msec, and the time for contact surface to reach downstream end is  $\frac{5.032}{838} \times 1000 \text{ msec} = 6$  msec. Then the available test time is

$$(6 - 4.42 - 1.02) = 0.56 \text{ msec}$$

as that shown in Fig. 19.

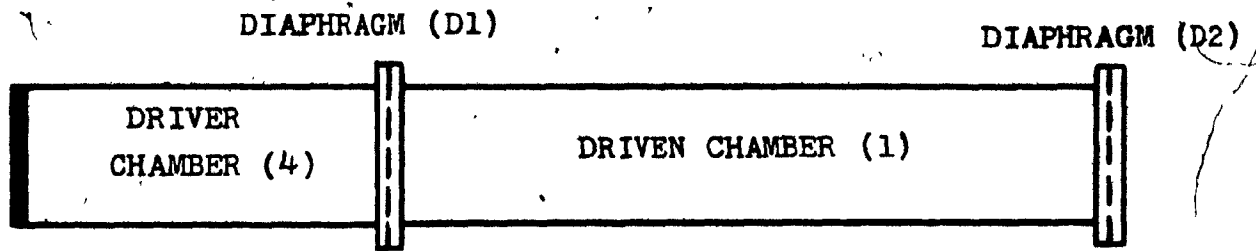


Fig. 1a. A simple Shock Tube Assembly.

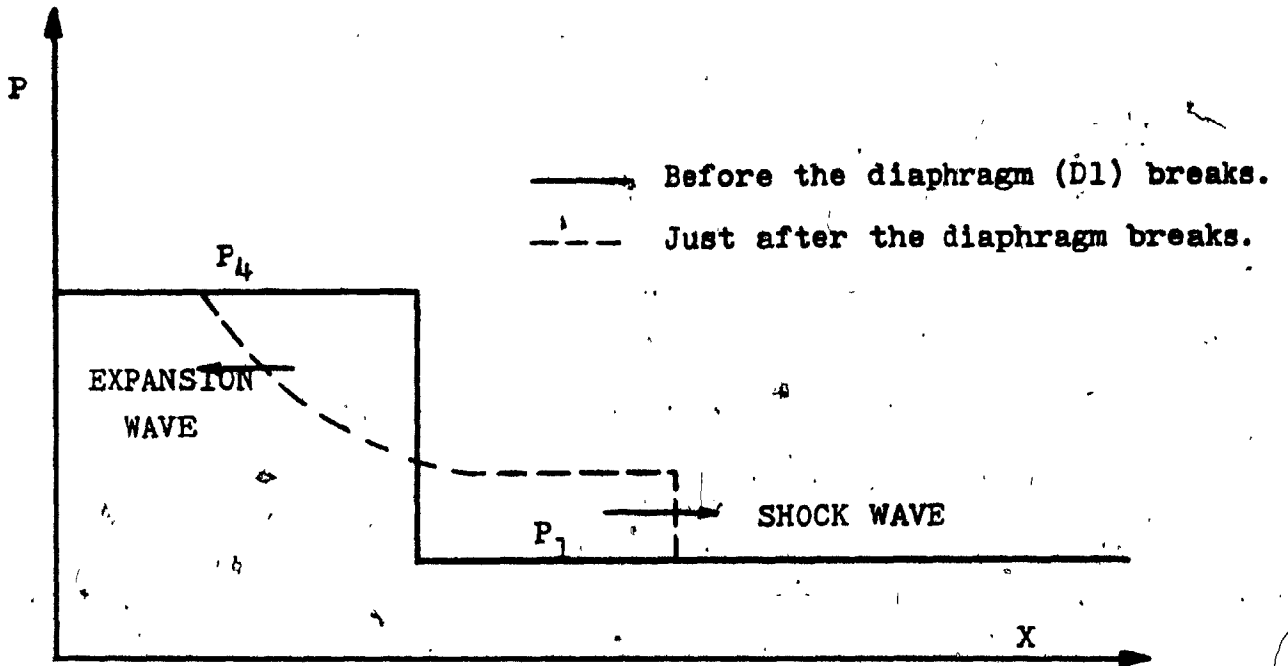


Fig. 1b. Pressure Distribution Along The Shock Tube.

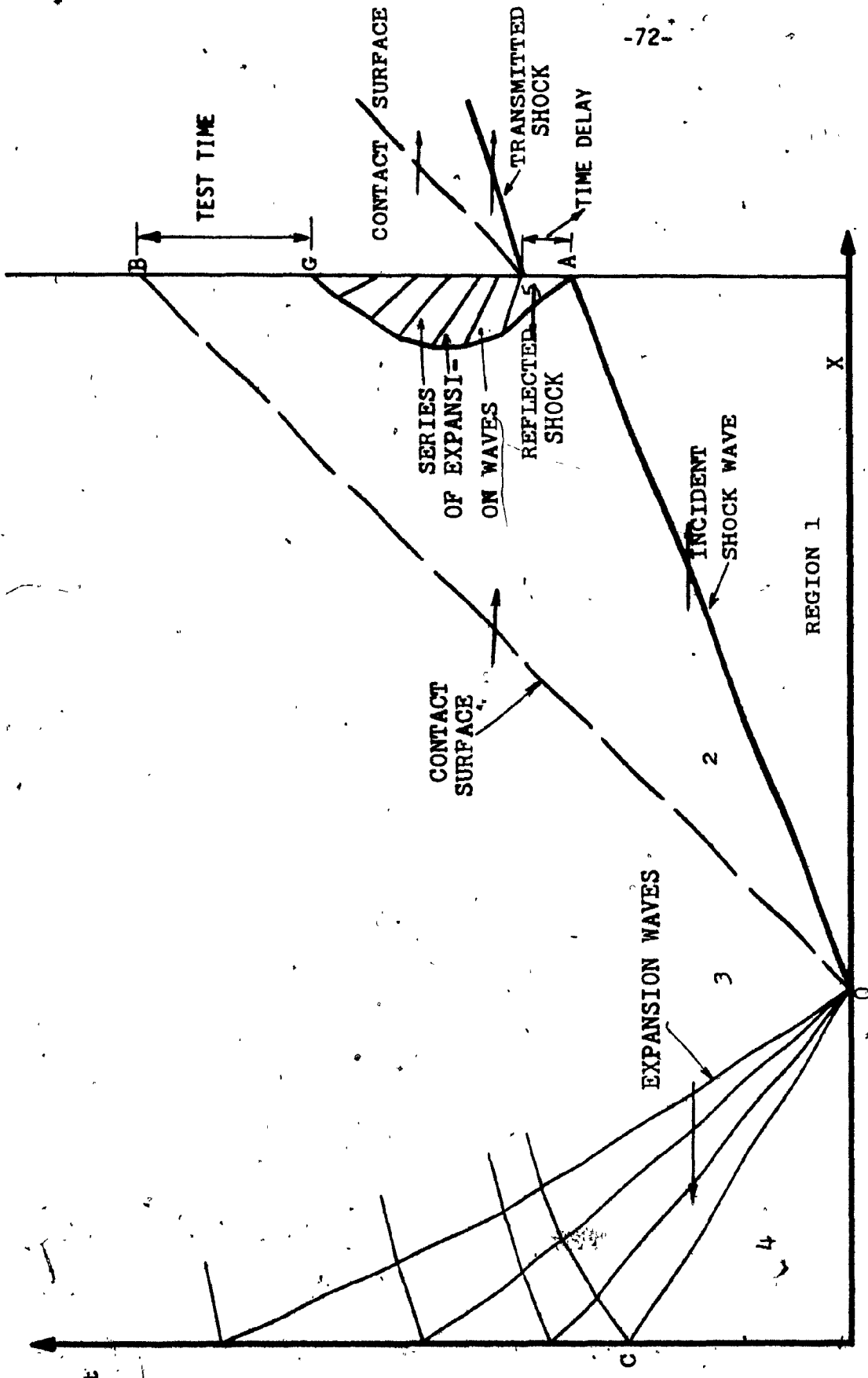


Fig. 1c.  $X, t$  Diagram Of The Process Occuring.

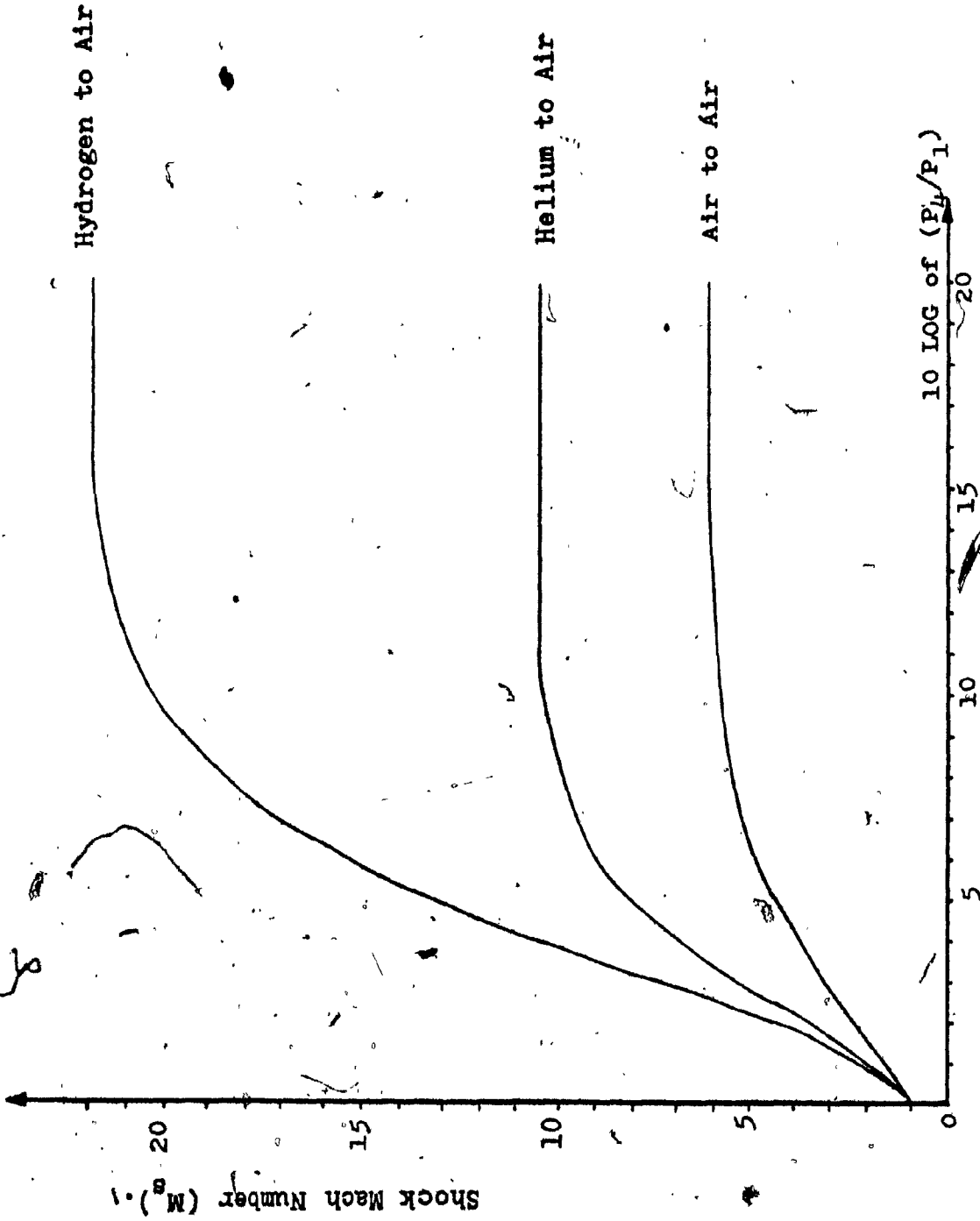


Fig. 2. Shock Mach Number against the Pressure Ratio of The Driver to the Driven Chambers.

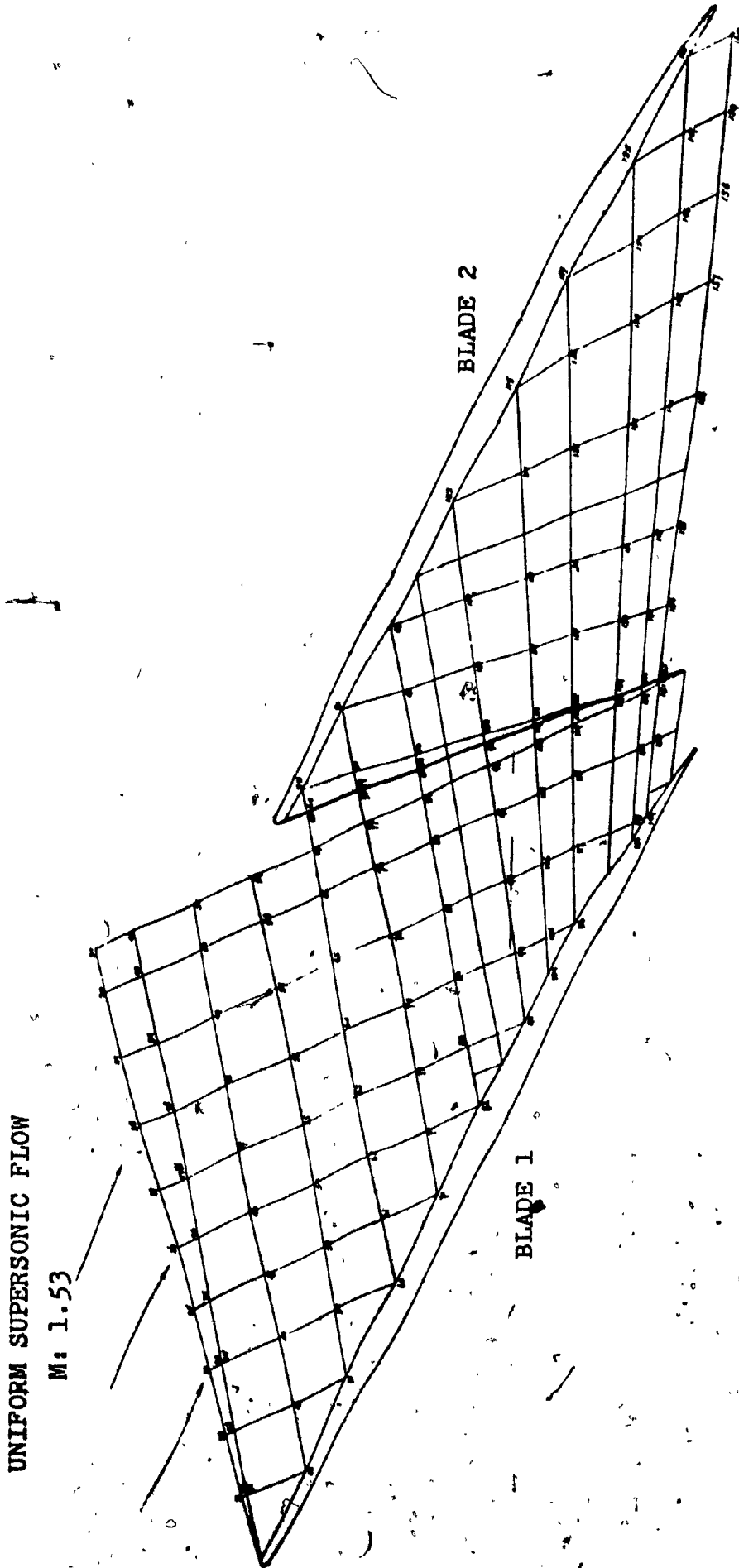


Fig. 3a. Wave Diagram For 4 Degrees Angle Of Incidence.

UNIFORM SUPERSONIC FLOW

M: 1.53

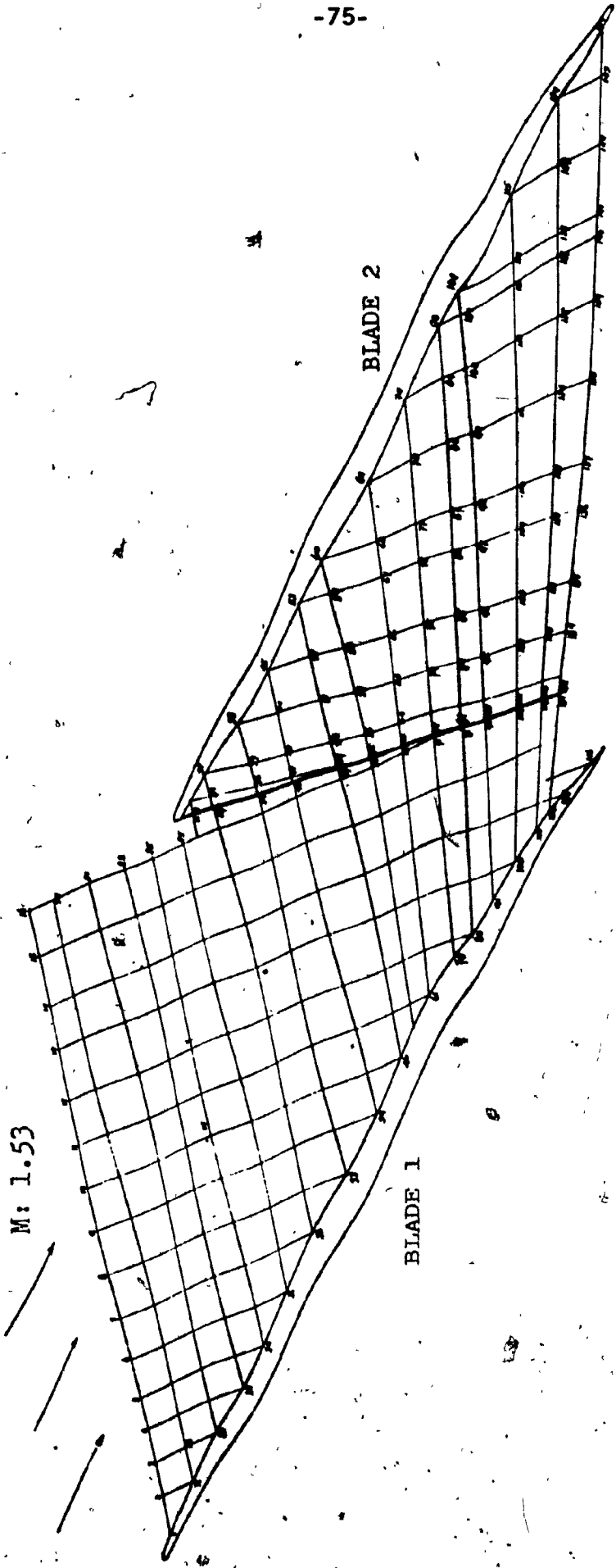


Fig. 3b. Wave Diagram For 0 Degrees Angle Of Incidence.



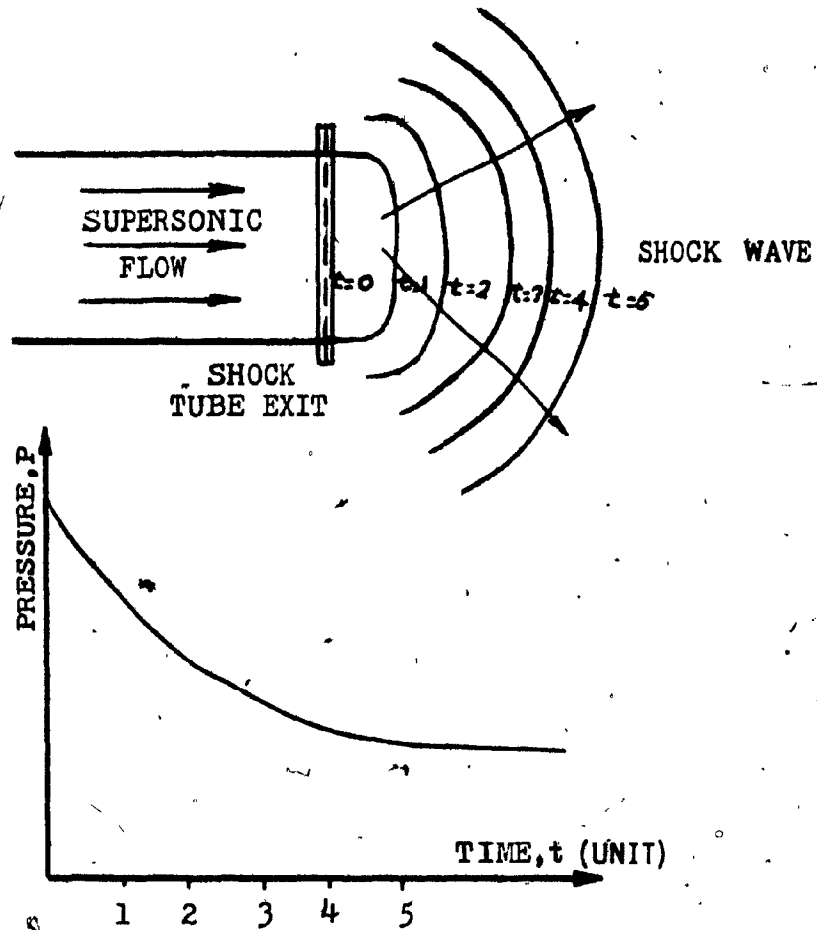


Fig. 4. The Transmitted Shock Wave Diffraction  
And The Open End Pressure History.

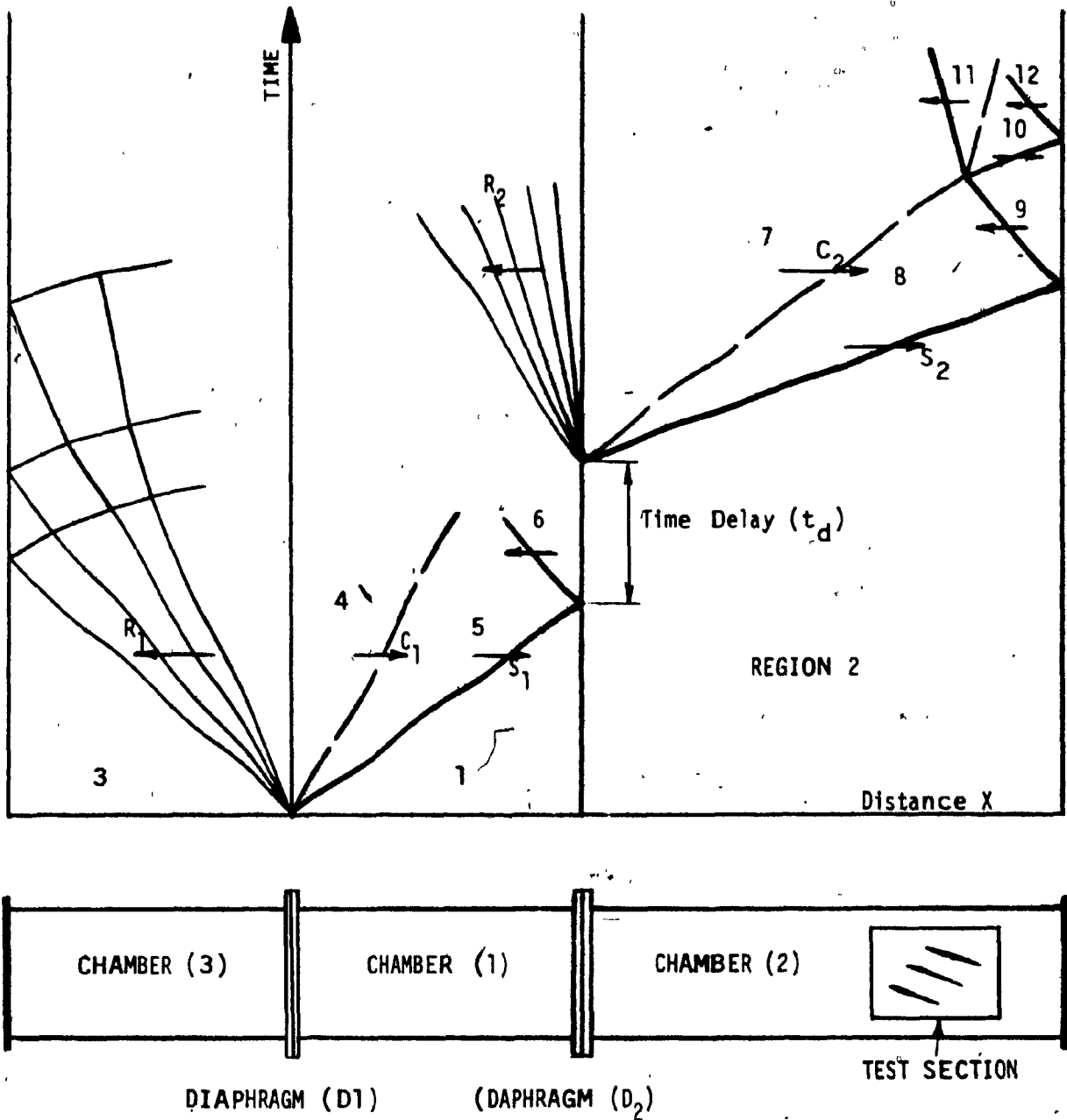


Fig. 5 . Shock Tube With Two Driver Chamber.

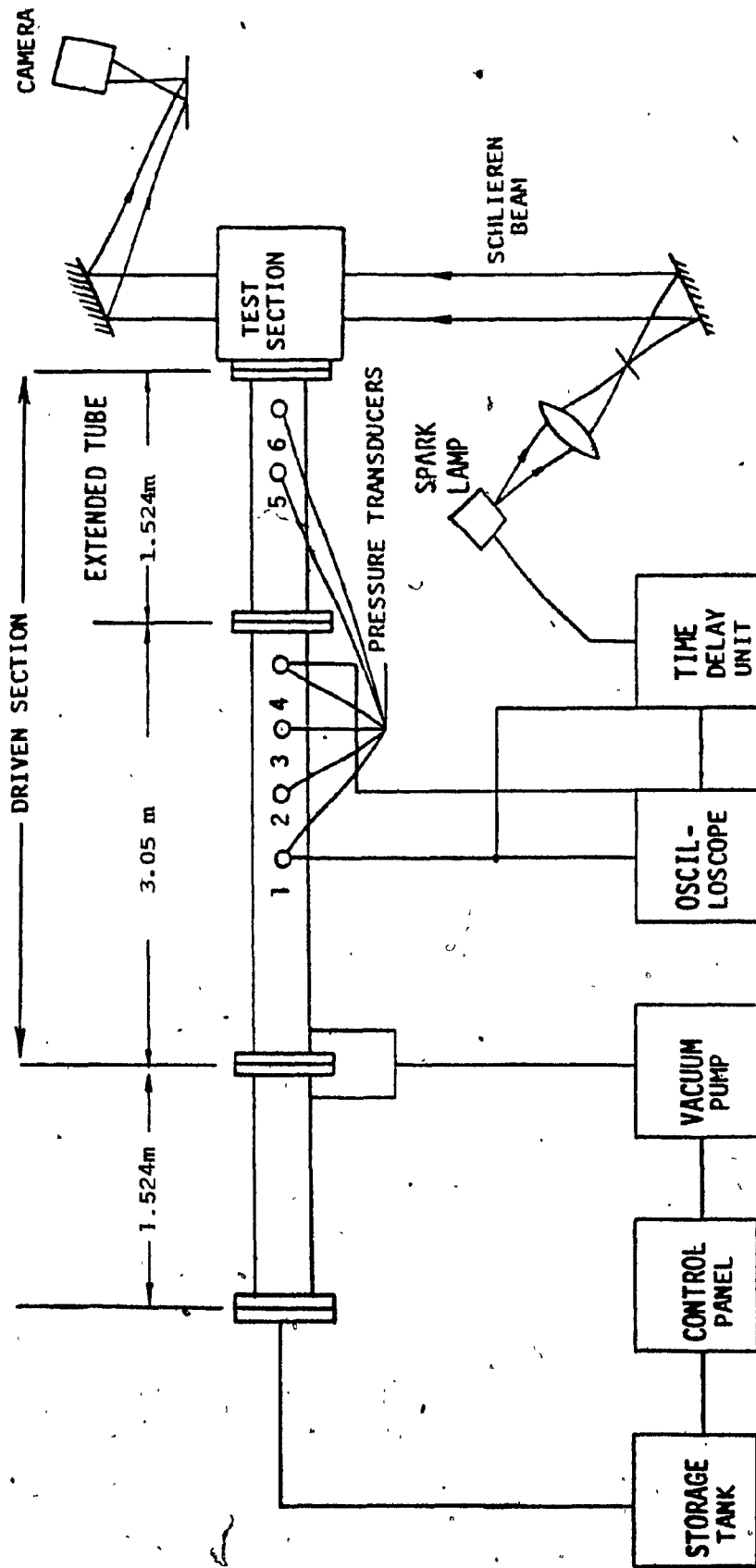


Fig. 6. A Schematic of the Square Shock Tube Together with Accessories.

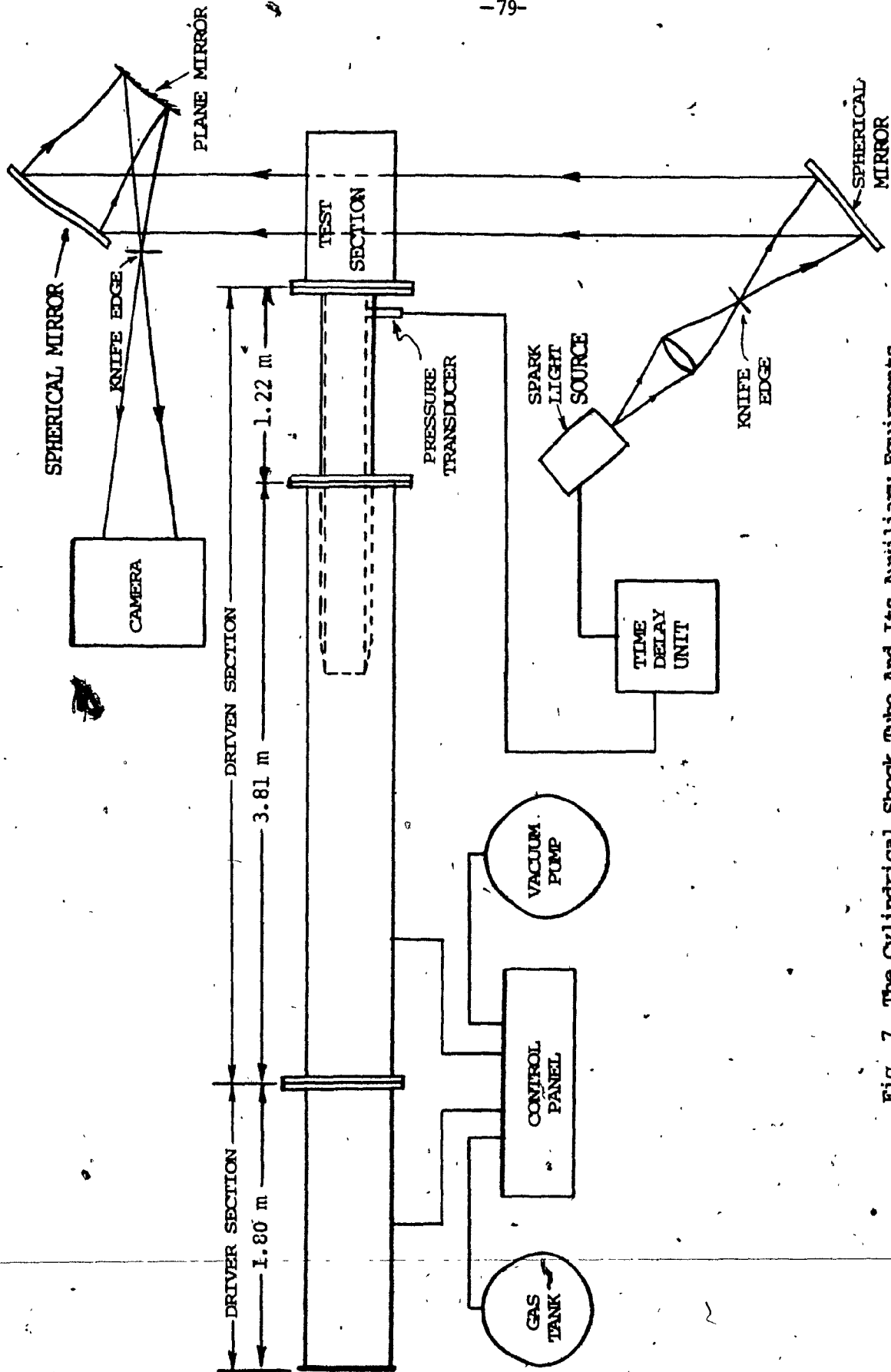
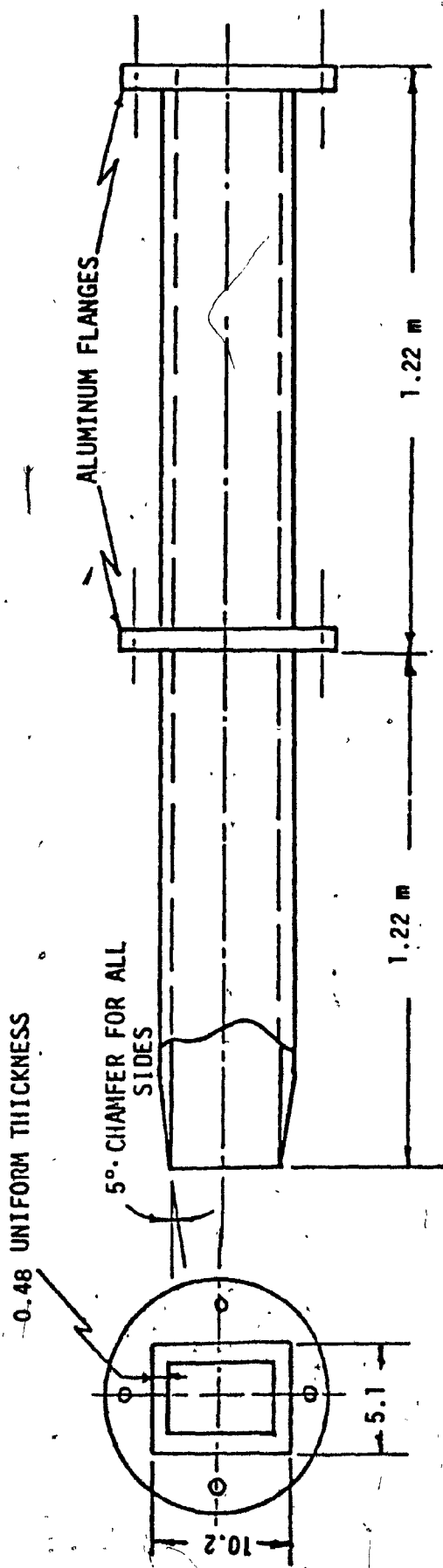
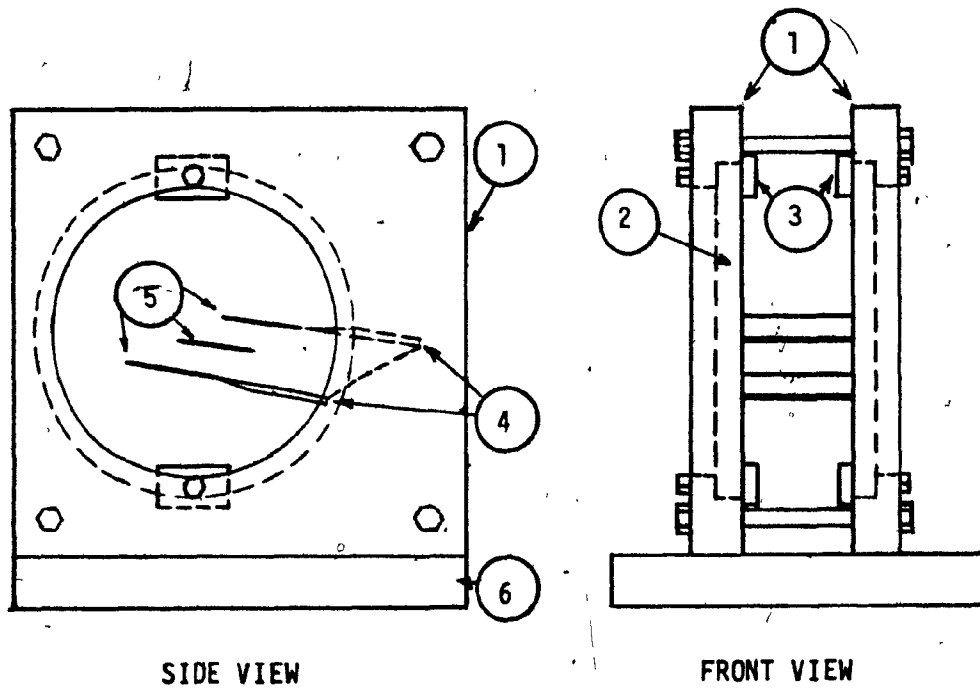


Fig. 7. The Cylindrical Shock Tube And Its Auxiliary Equipments.



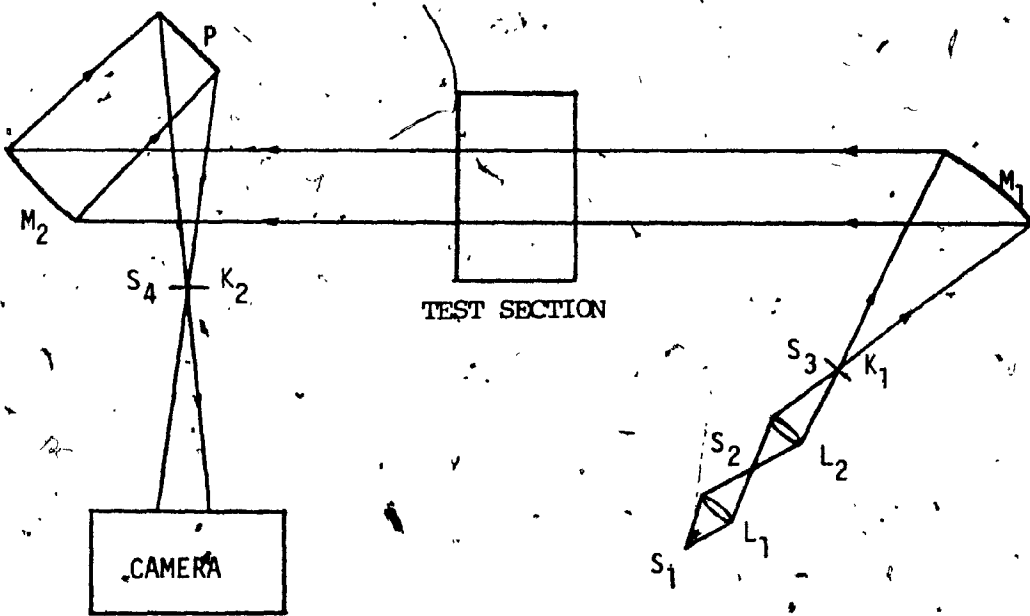
All dimensions are given in cm, otherwise stated.

Fig. 8. Rectangular Cross Section Extension Tube.



- LEGENDS
- ① Vertical Aluminium Plates
  - ② Plexyglass Window
  - ③ Fasteners
  - ④ Extension Plates
  - ⑤ Blades
  - ⑥ Aluminium Base

Fig. 9. Shock Tube Test Section.



- LEGENDS
- $K_1, K_2$  : Knife Edge
  - $L_1, L_2$  : Condenser Lenses
  - $M_1, M_2$  : Spherical Mirrors
  - P : Plane Mirror
  - $S_1$  : Continuous Light Source
  - $S_2, S_3, S_4$  : Point Light Sources

Fig. 10. Top-View Of The Schlieren System.

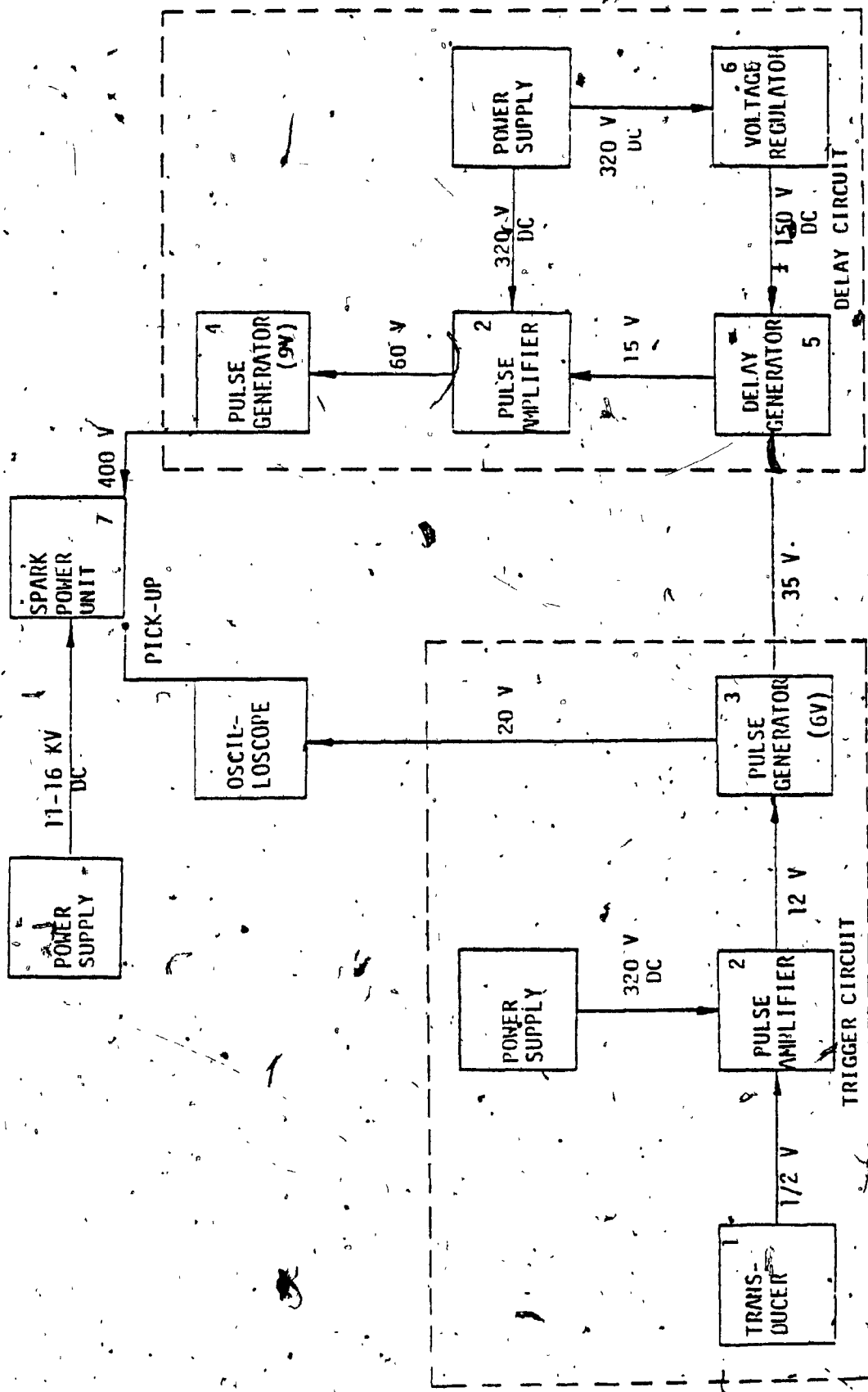
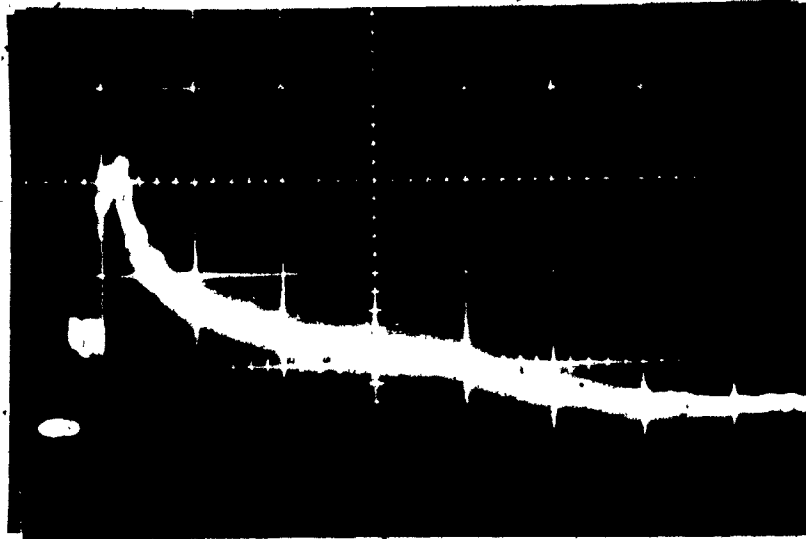


Fig. 11. The Time-Delay Spark System.





Transducer 5 : Trigger  
Transducer 6 : Measure  
Vacuum Pressure : 700 mm Hg  
Oscilloscope Scale : 0.5 msec/cm, 0.5 v/cm

Fig. 12a. Transducer Pressure Traces for 3.5 m Driven Section Length.

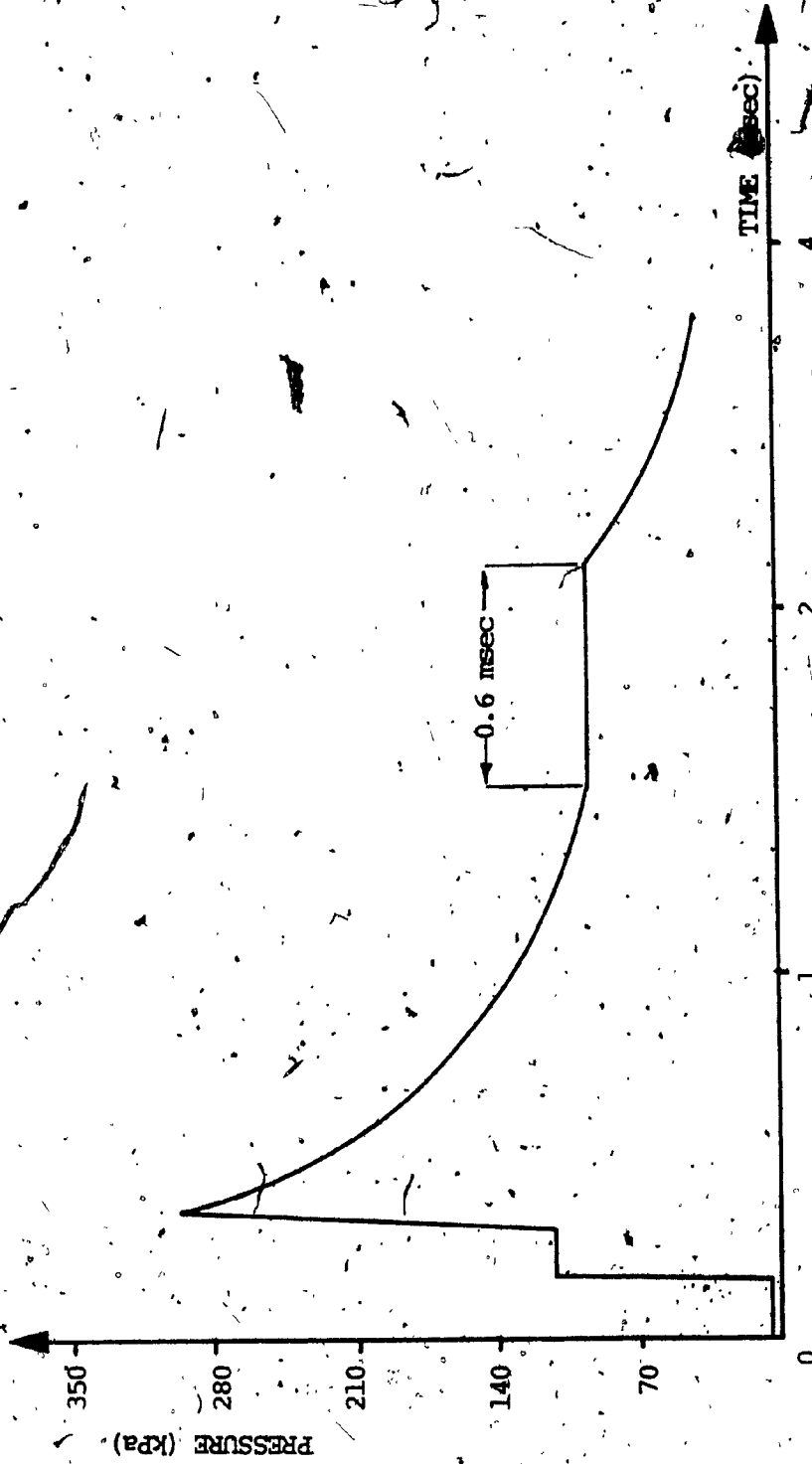
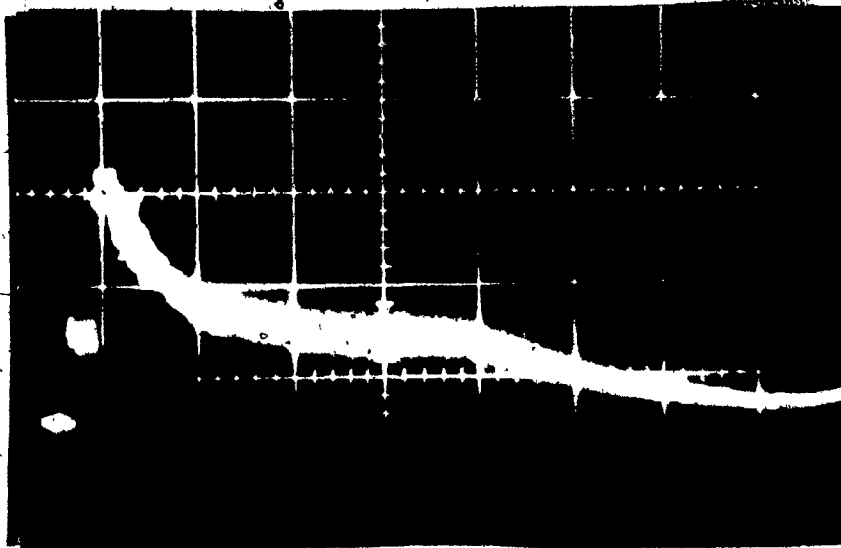


Fig. 12b. Interpretation Of Fig. 11a.



Transducer 5 : Trigger  
Transducer 6 : Measure  
Vacuum Pressure : 700 mm Hg  
Oscilloscope Scale : 0.5 msec/cm, 0.5 v/cm.

Fig. 13a. Transducer Pressure Traces 4.8 m  
Driven Section Length.

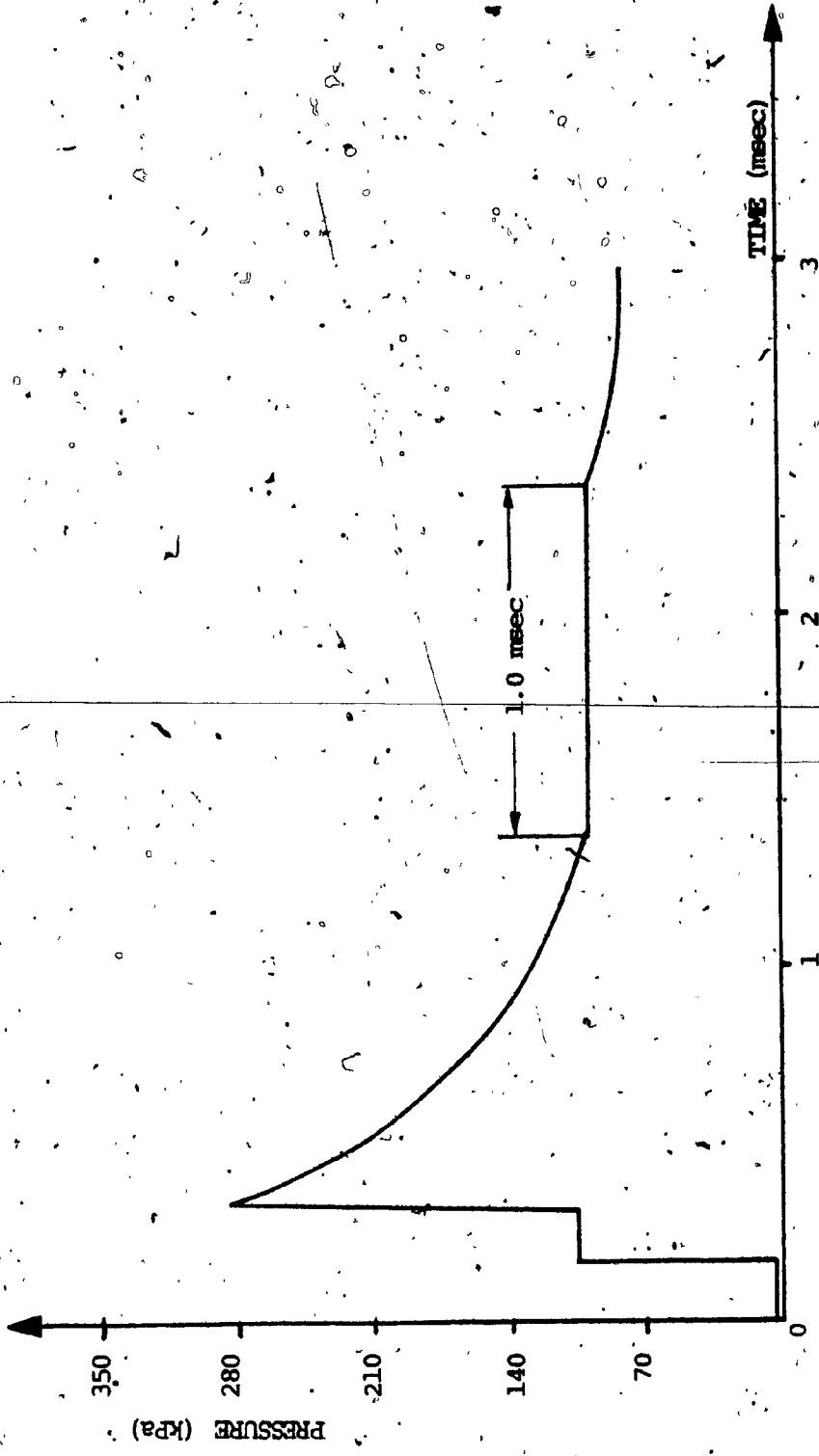


Fig. 13b. Interpretation of Fig. 12a.

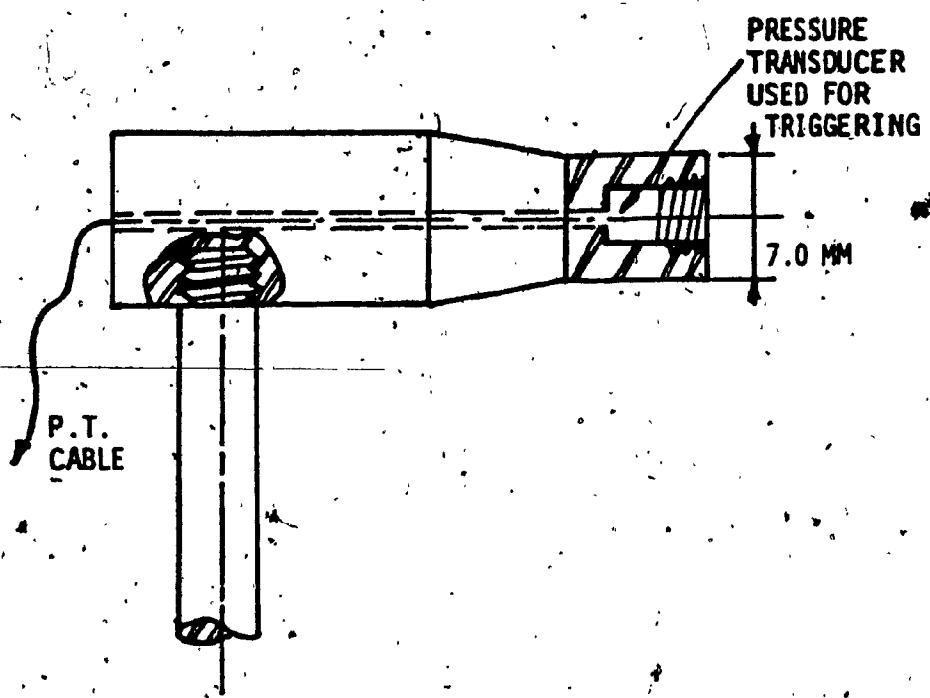


Fig. 14. Blunt Body-Of Revolution.

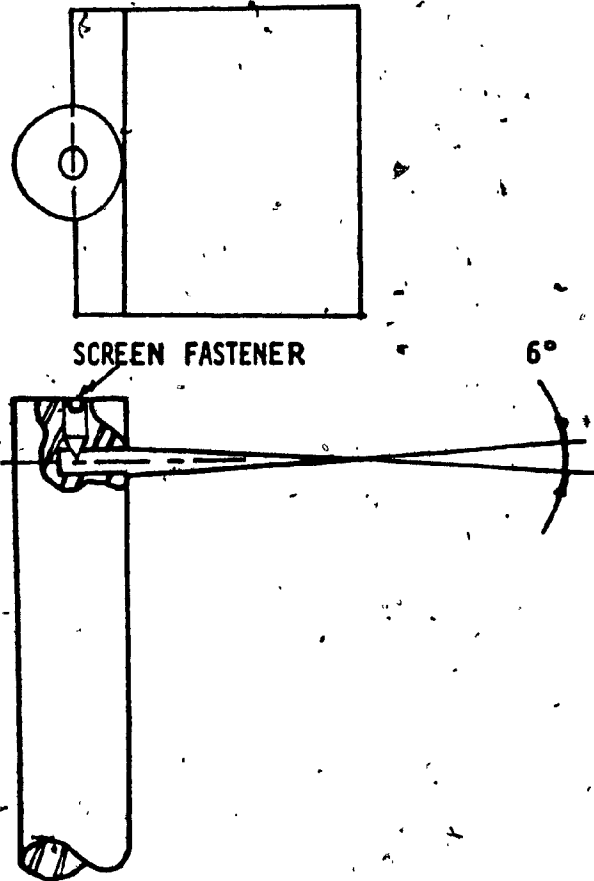
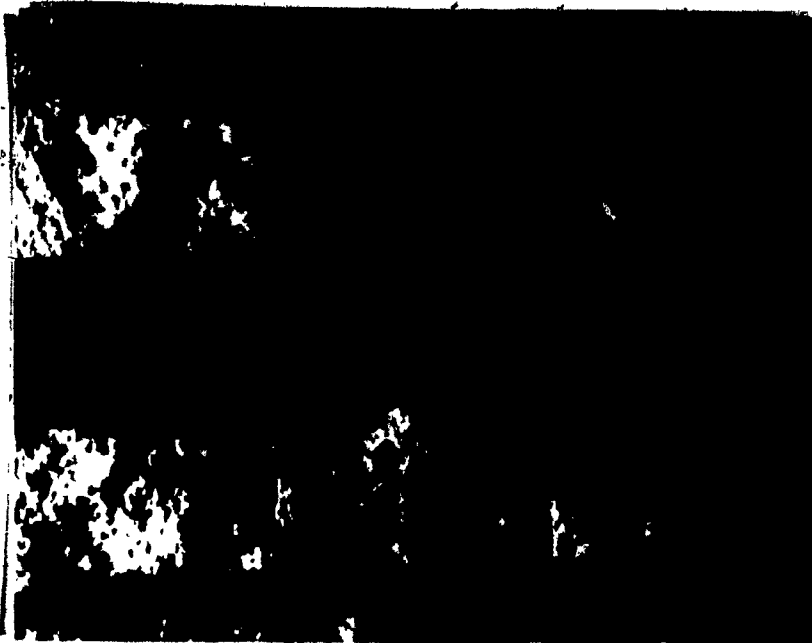
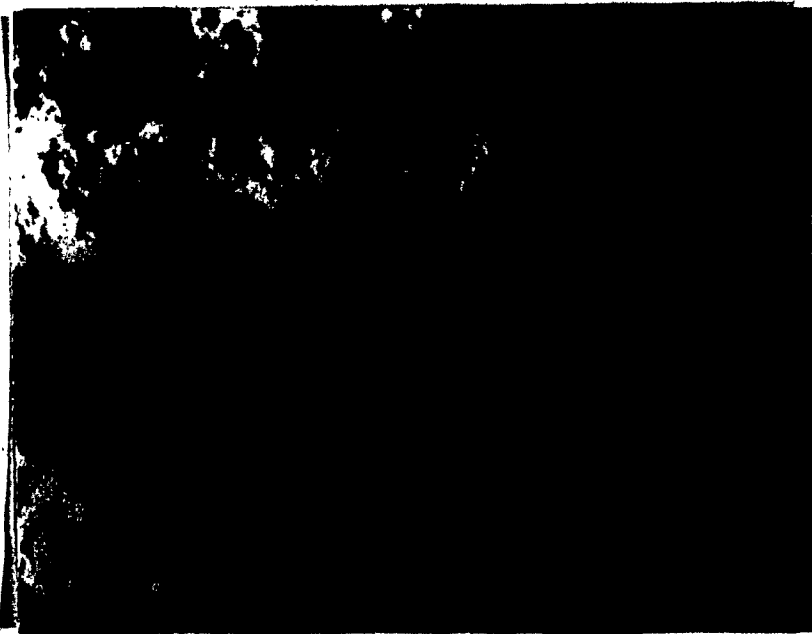


Fig. 15. Wedge With 6 Degrees Included Angle.

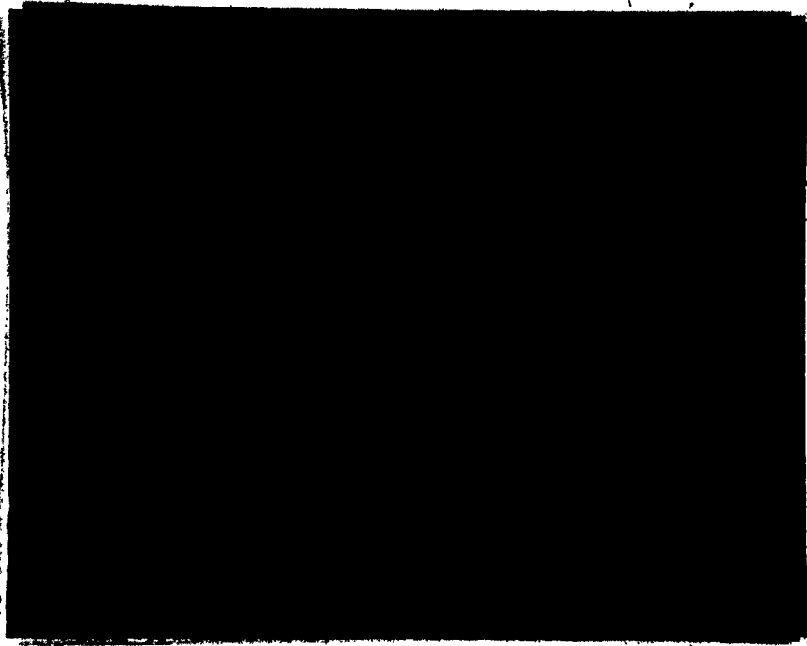


Time Delay 1350  $\mu$ sec  
Distance From Exit 19 mm  
Vacuum Pressure 700 mm Hg



Time Delay 1350  $\mu$ sec  
Distance From Exit 25.5 mm  
Vacuum Pressure 700 mm Hg

Fig. 16a. Schlieren Photographs Of The Blunt Body For Determining Flow Uniformity In Longitudinal Direction.



Time Delay 1350 sec  
Distance From Exit 38 mm  
Vacuum Pressure 700 mm Hg

Fig. 16a. Continues.



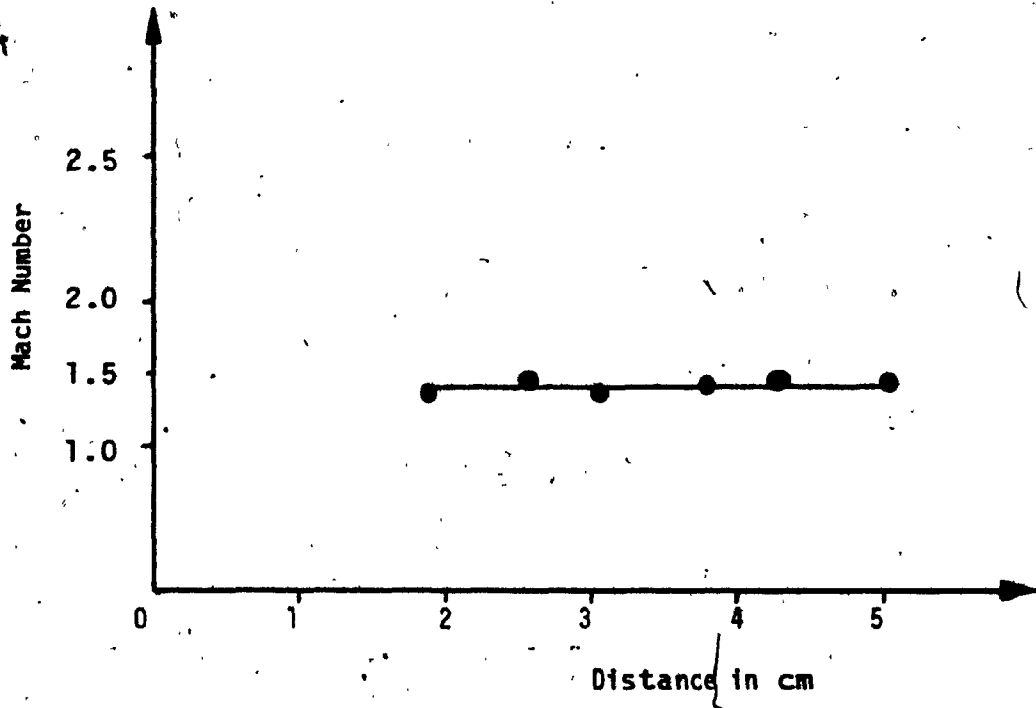
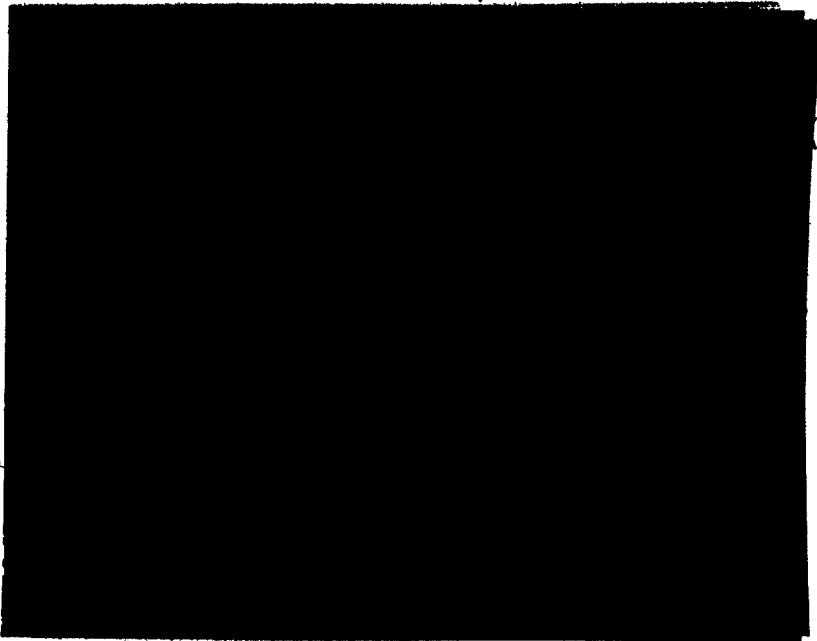
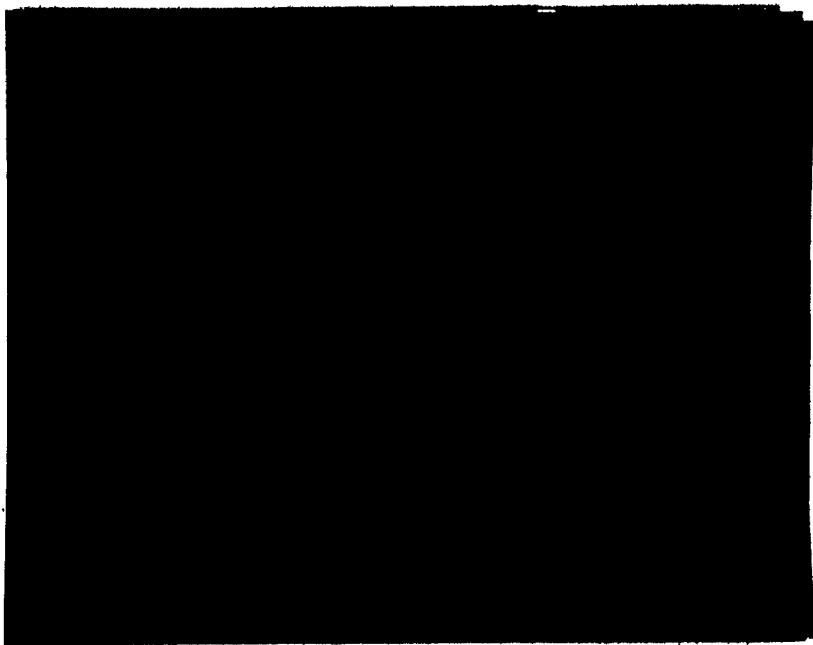


Fig. 16b. Mach Number Variation In The Longitudinal Direction.



Position A  
Time Delay 1350  $\mu$ sec  
Distance From Exit 25.4 mm  
Vacuum Pressure 700 mm Hg



Position B  
Time Delay 1350  $\mu$ sec  
Distance From Exit 25.4 mm  
Vacuum Pressure 700 mm Hg

Fig. 17a. Schlieren Photographs Of A Wedge For Determining Flow Uniformity In Transverse Direction.



Position C  
Time Delay 1350  $\mu$ sec  
Distance From Exit 25.4 mm  
Vacuum Pressure 700 mm Hg

Fig. 17a. Continues.

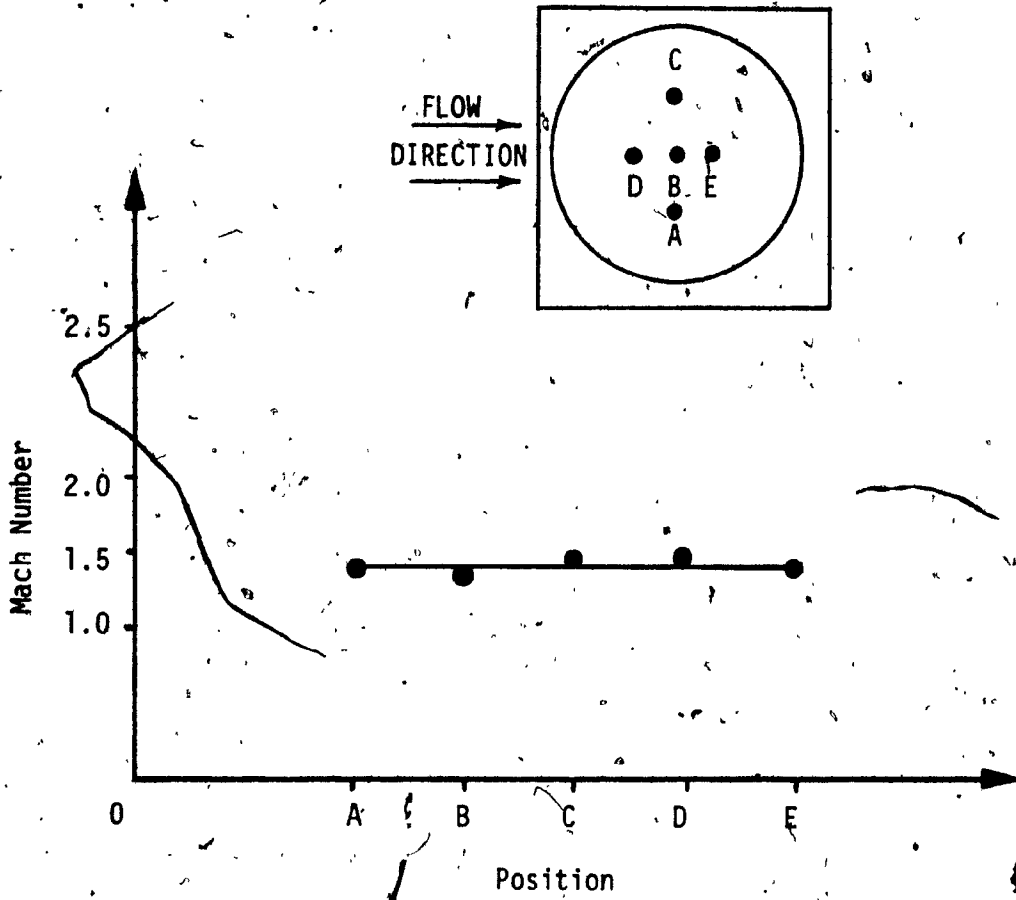


Fig. 17b. Mach Number Variation In The Lateral Direction

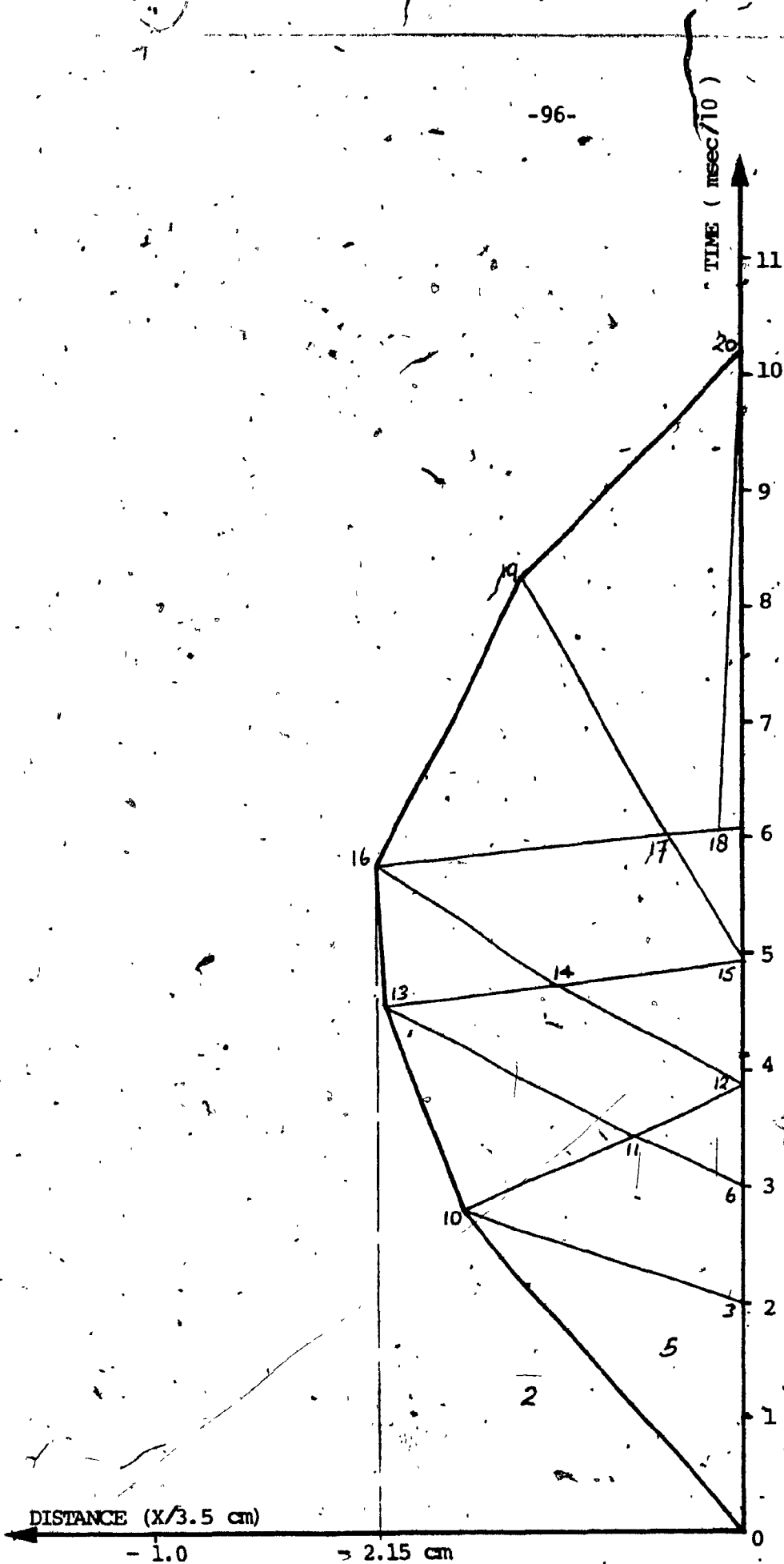


Fig. 18. Reflected Shock Wave Interaction With The Expansion Waves Originating At The Open End.

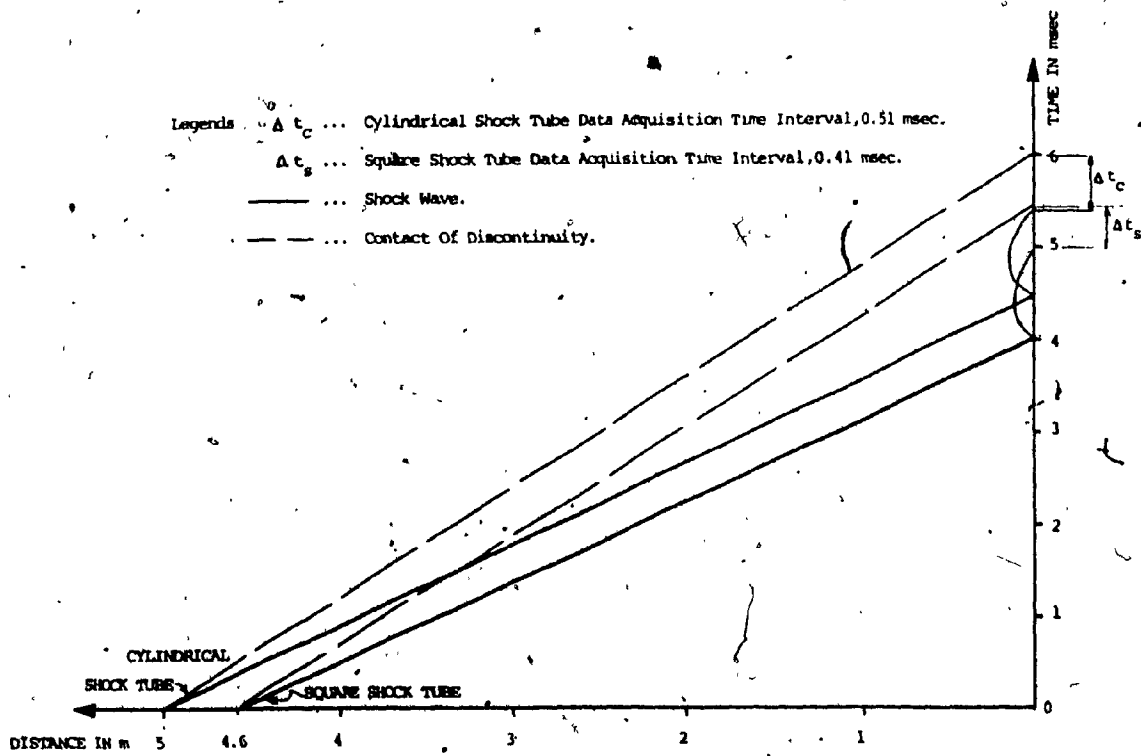


Fig. 19. Data Acquisition Time Interval.



Fig. 20a. Schlieren Picture Of A Single Turbine Blade  
Inside Uniform Flow Of Mach Number 1.4.

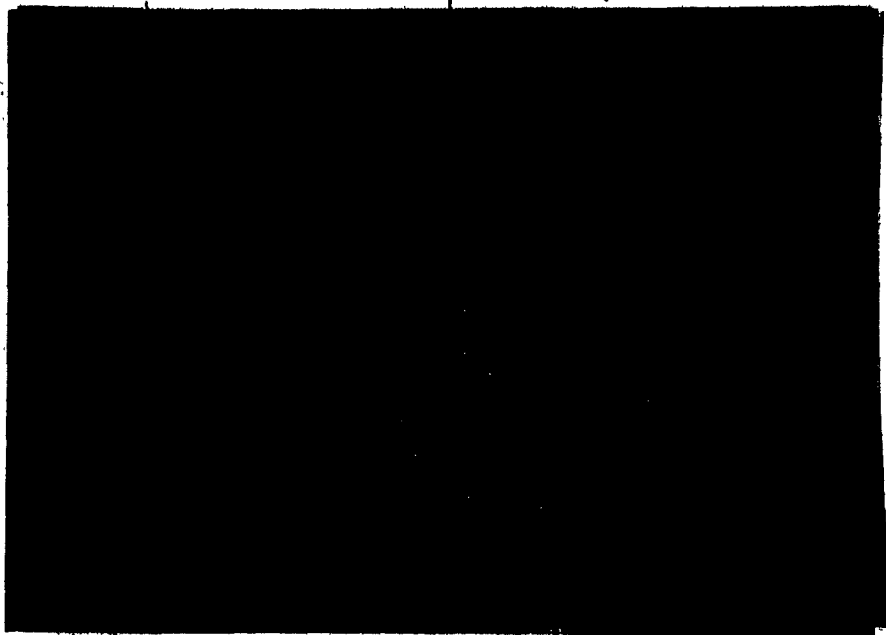
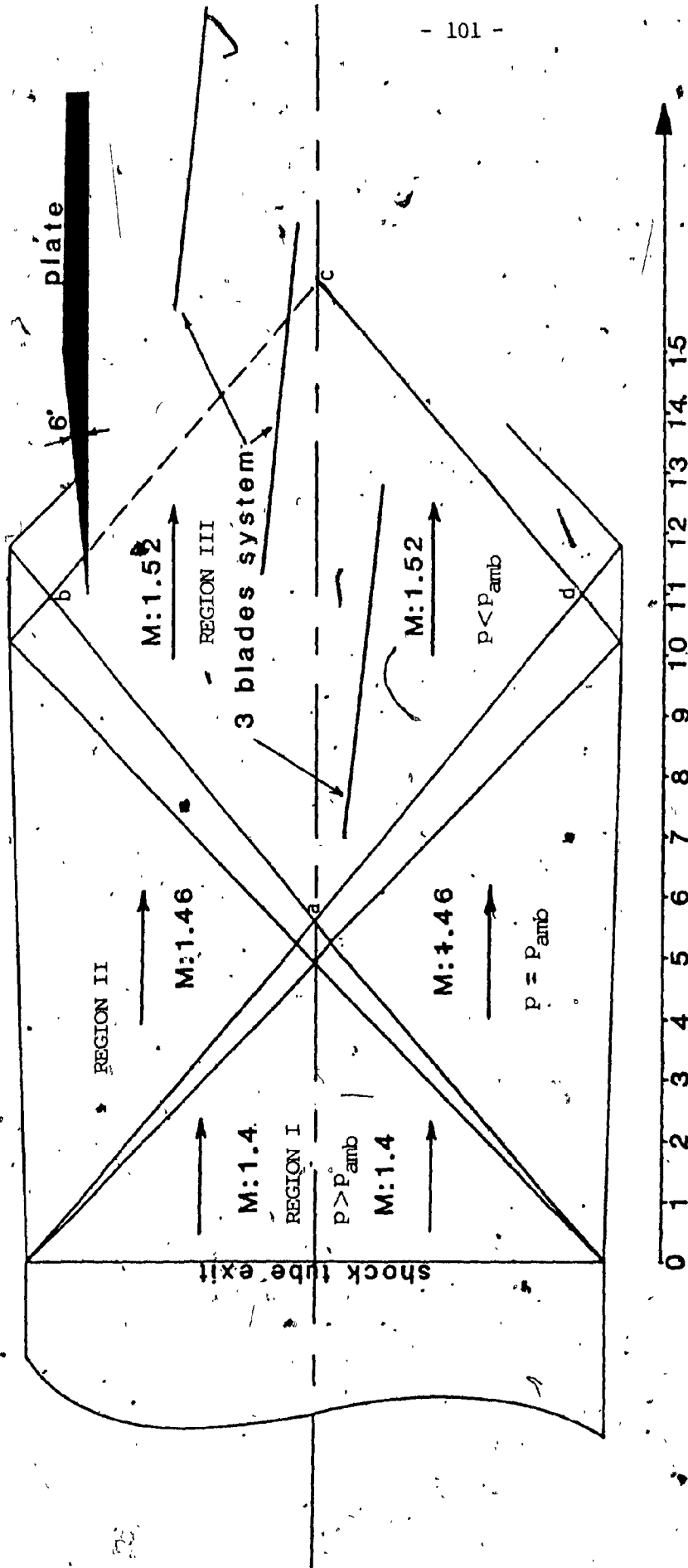


Fig. 20b. Schlieren Picture Of Two Turbine Blades  
Inside Uniform Supersonic Flow Of Mach  
Number 1.4.





Fig. 20c. Schlieren Picture Of Two Turbine Blades With Damper Placed Downstream Of The System.

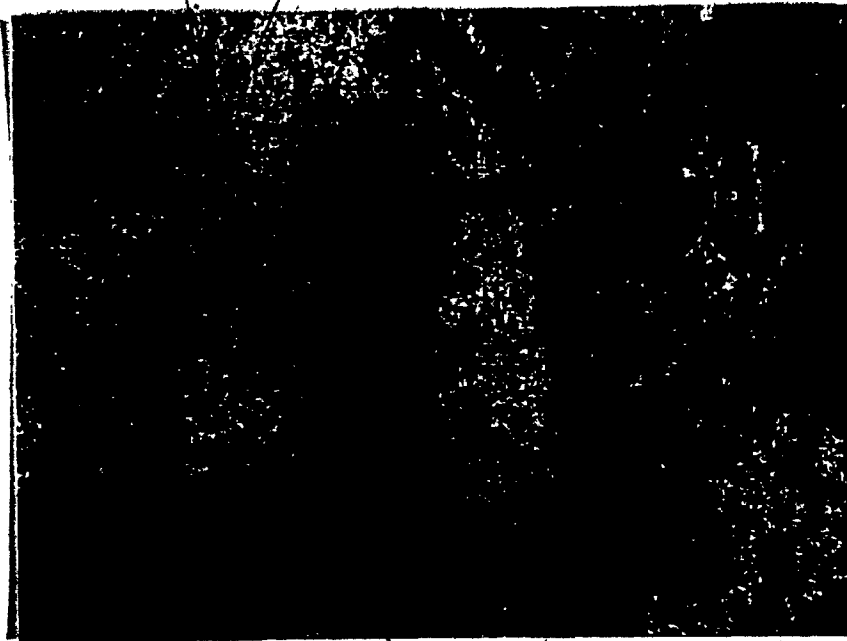


Distance From Shock Tube Exit (in CM)

Fig. 21. The Wave Diagram Of The Underexpanded Jet.

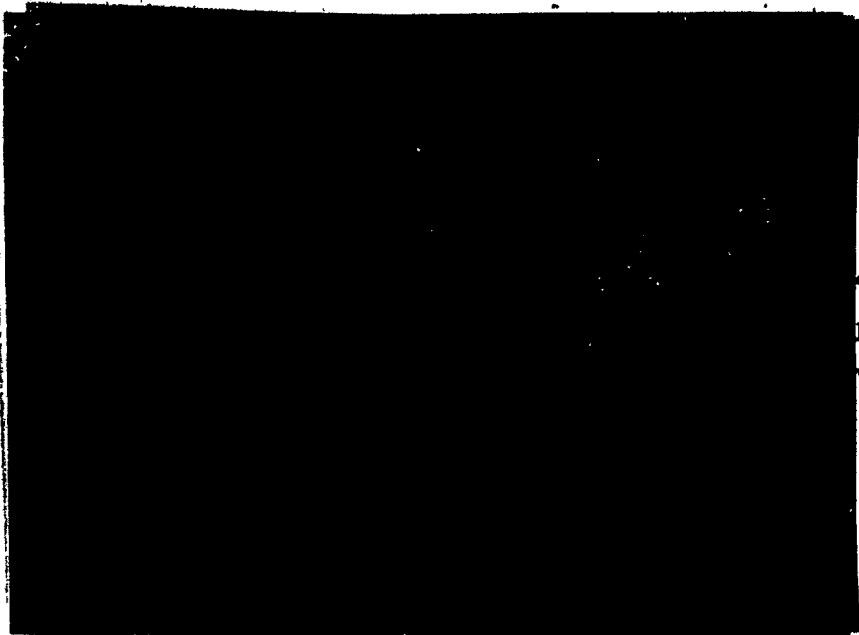


Time Delay 1400 sec  
Distance From Exit 19.1 mm  
Vacuum Pressure 620 mm Hg

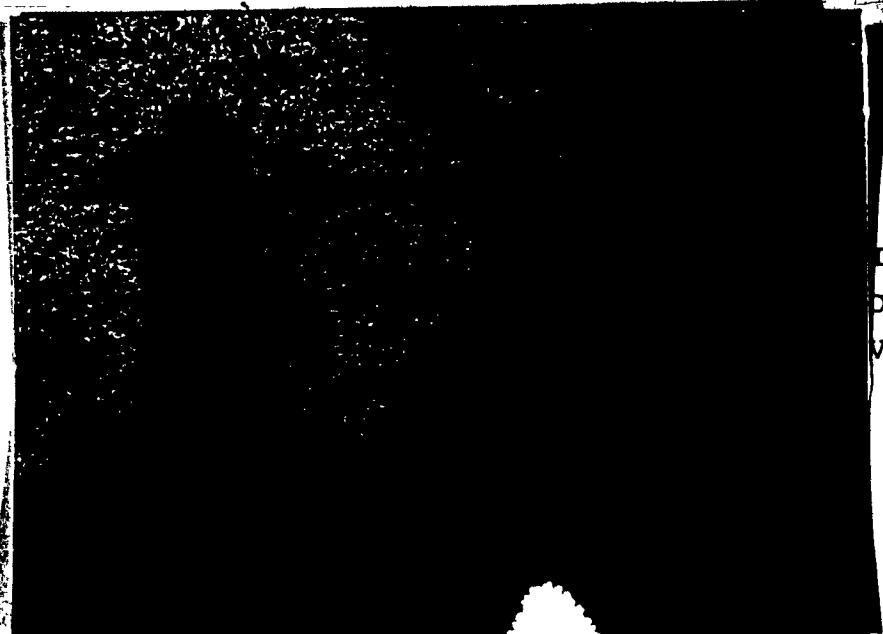


Time Delay 1400 sec  
Distance From Exit 32 mm  
Vacuum Pressure 620 mm Hg

Fig. 22a. Schlieren Photographs Of A Wedge Inside Uniform  
Supersonic Flow.



Time Delay 1400 sec  
Distance From Exit 38 mm  
Vacuum Pressure 620 mm Hg



Time Delay 1400 sec  
Distance From Exit 51 mm  
Vacuum Pressure 620 mm Hg

Fig. 22a. Continues

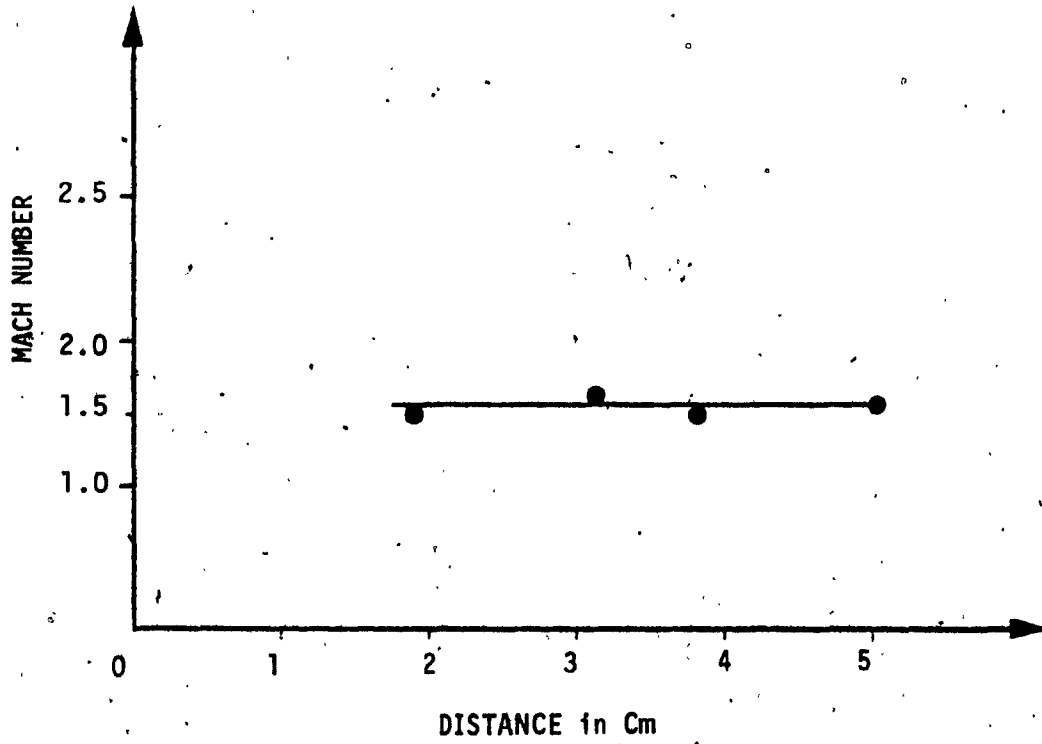


Fig. 22b. Uniform Flow Mach Number.



Driver Pressure . 1120 kPa  
Vacuum Pressure 620 mm Hg  
Time Delay 1400 sec

Fig. 23. Schlieren Picture Of The Cascade System Exposed  
To Supersonic Flow Of  $M : 1.53$  And 4 Degrees  
Angle Of Incidence.

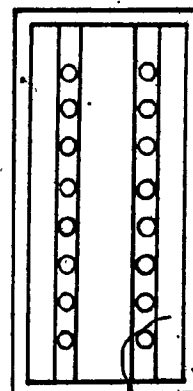
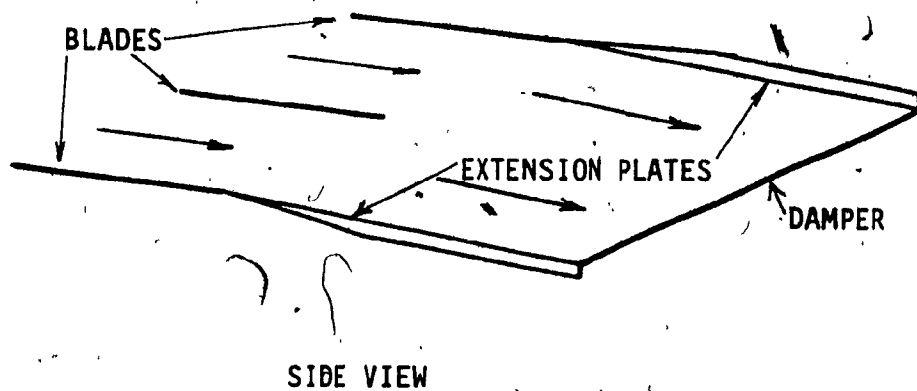
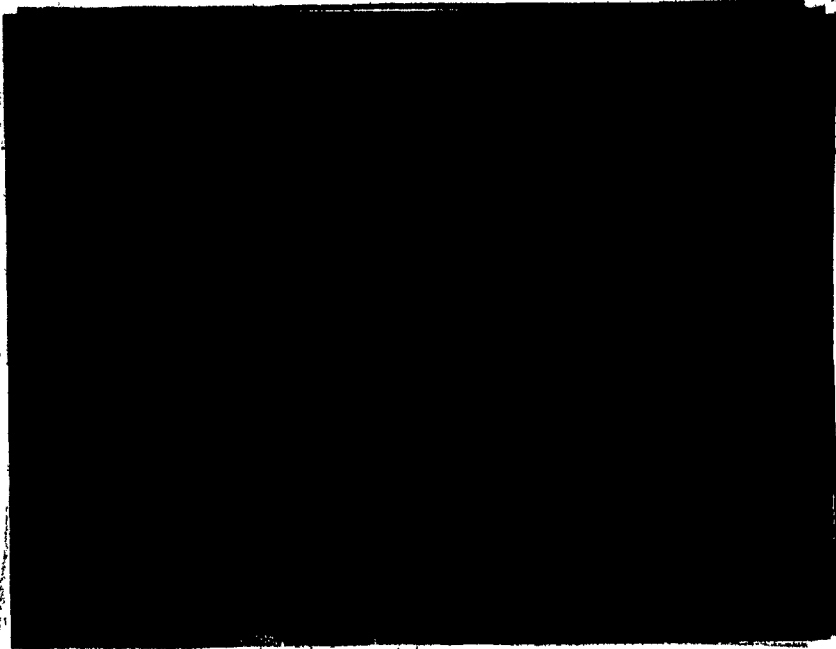


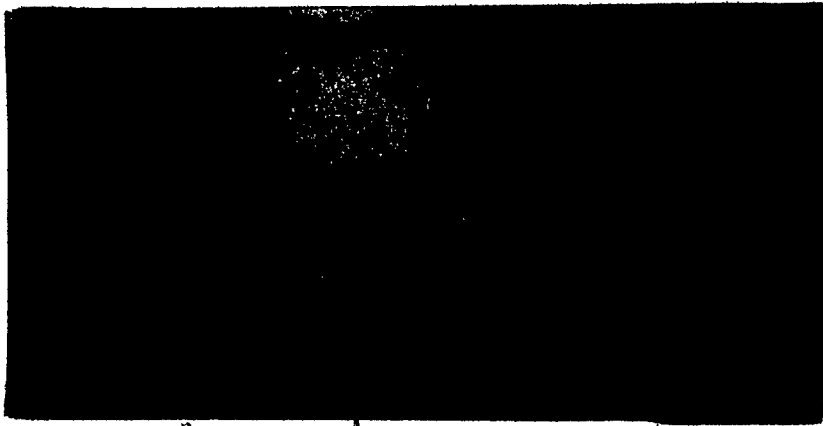
Fig. 24. Schematic View Of Damper



Driver Pressure 1120 kPa  
Vacuum Pressure 620 mm Hg  
Time Delay 1400 sec

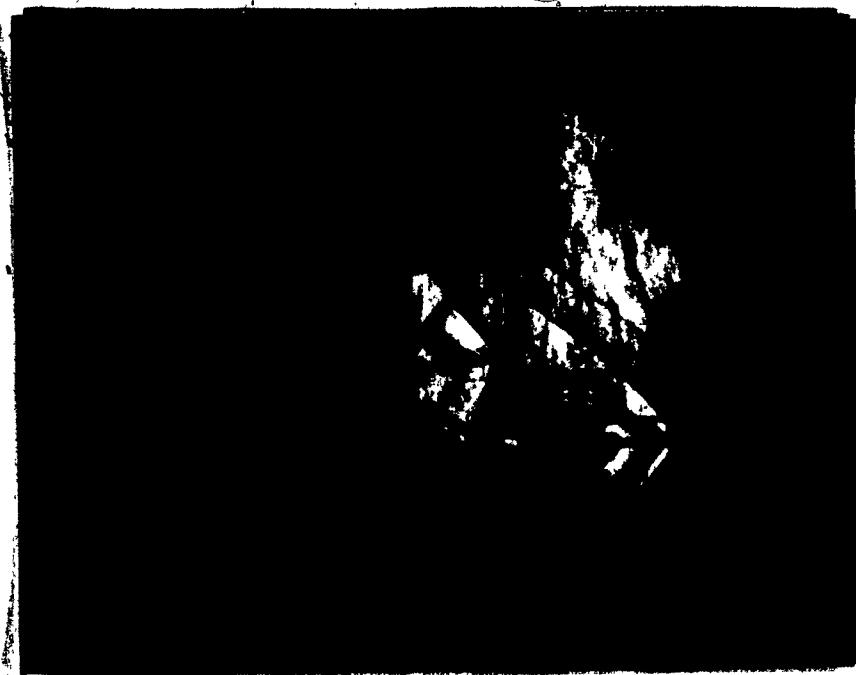
Fig. 25a. Schlieren Picture Of Three Blade Cascade System  
With 8% Reduction Of Exit Area.





Driver Pressure 1120 kPa  
Vacuum Pressure 620 mm Hg  
Time Delay 1400 sec

Fig. 25b. Schlieren Picture Of Three Blade Cascade System  
With 10% Reduction Of Exit Area.



Driver Pressure	1120 kPa
Vacuum Pressure	620 mm Hg
Time Delay	1400 sec

Fig. -25c. Schlieren Picture Of Three Blade Cascade System  
With 24% Reduction Of Exit Area.

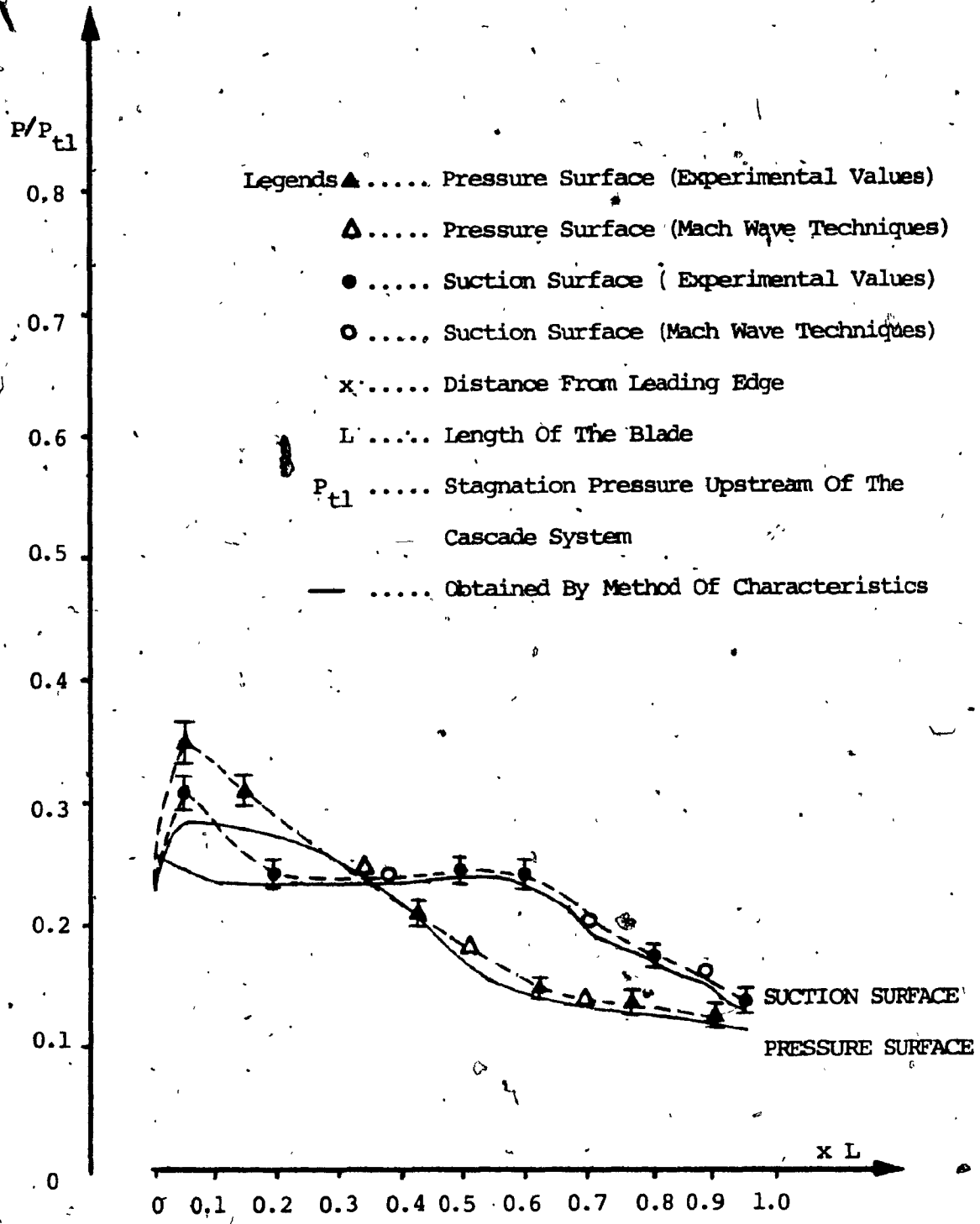


Fig. 26a. Surface Pressure Distribution For Pressure Ratio Of 1.3 And 4 Degrees Angle Of Incidence.

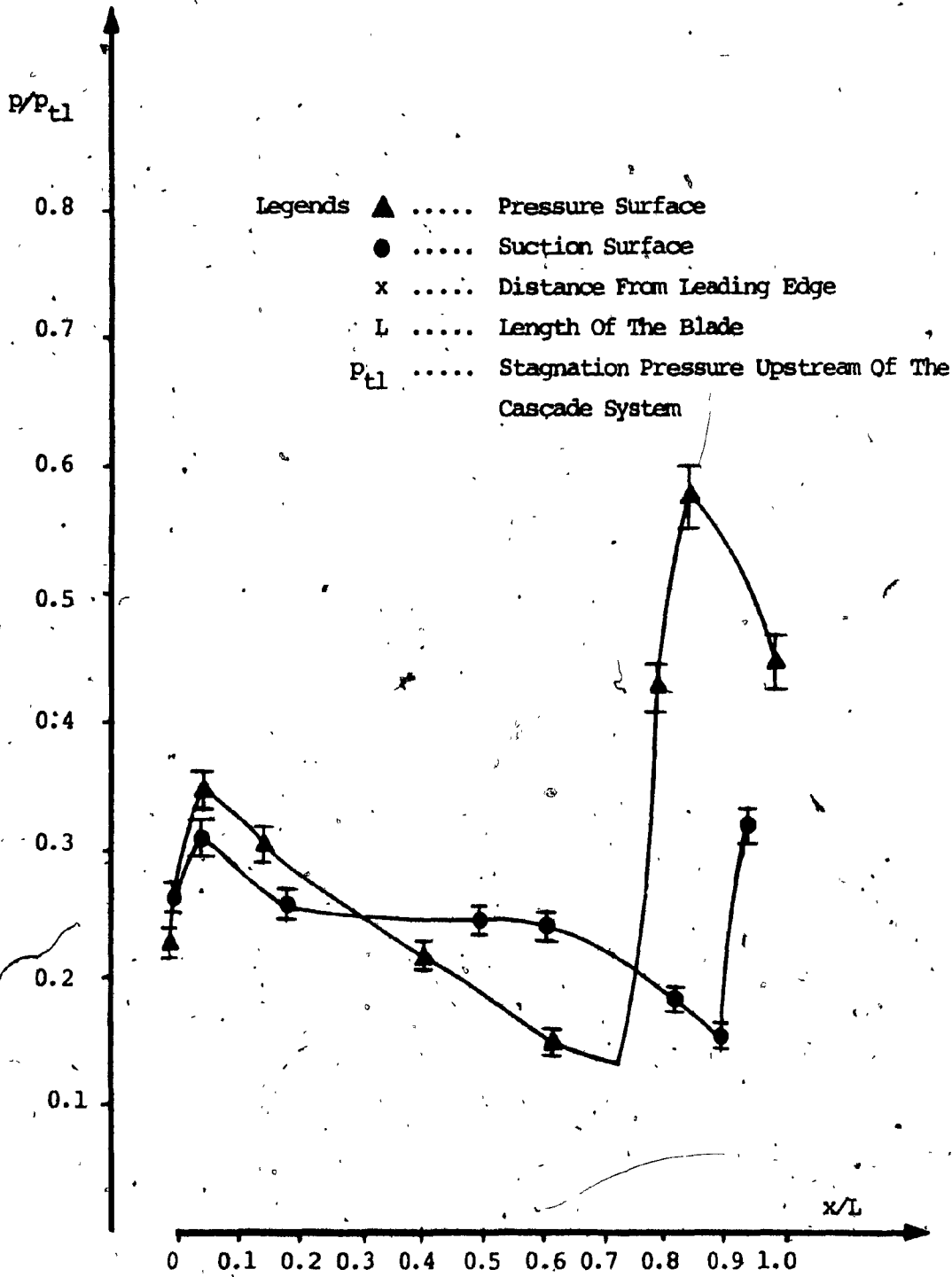


Fig. 26b. Surface Pressure Distribution For Pressure Ratio Of 1.62 And 4 Degree Angle Of Incidence.

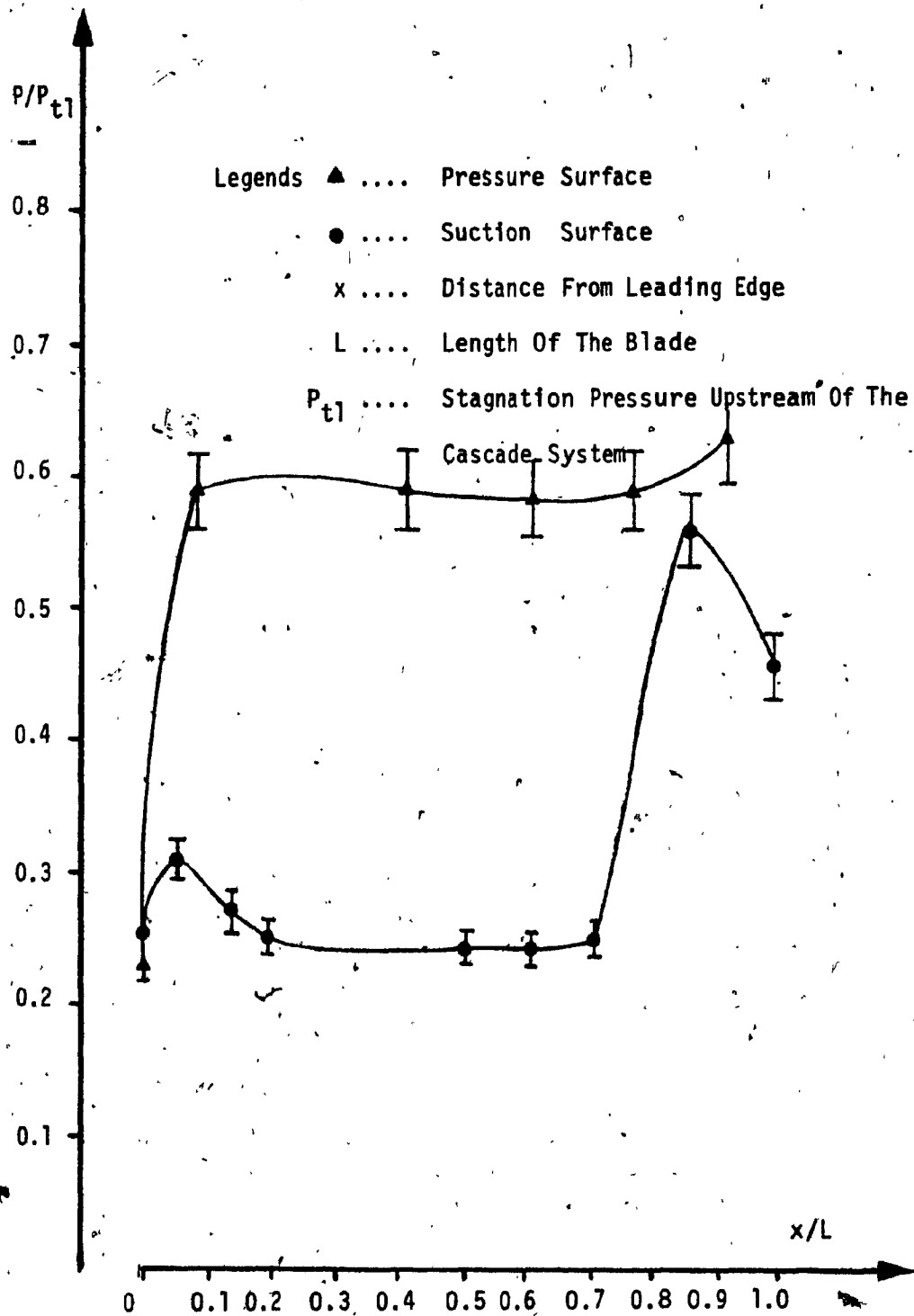


Fig. 26c. Surface Pressure Distribution For Pressure Ratio Of 2.0 and 4 Degrees Angle Of Incidence.

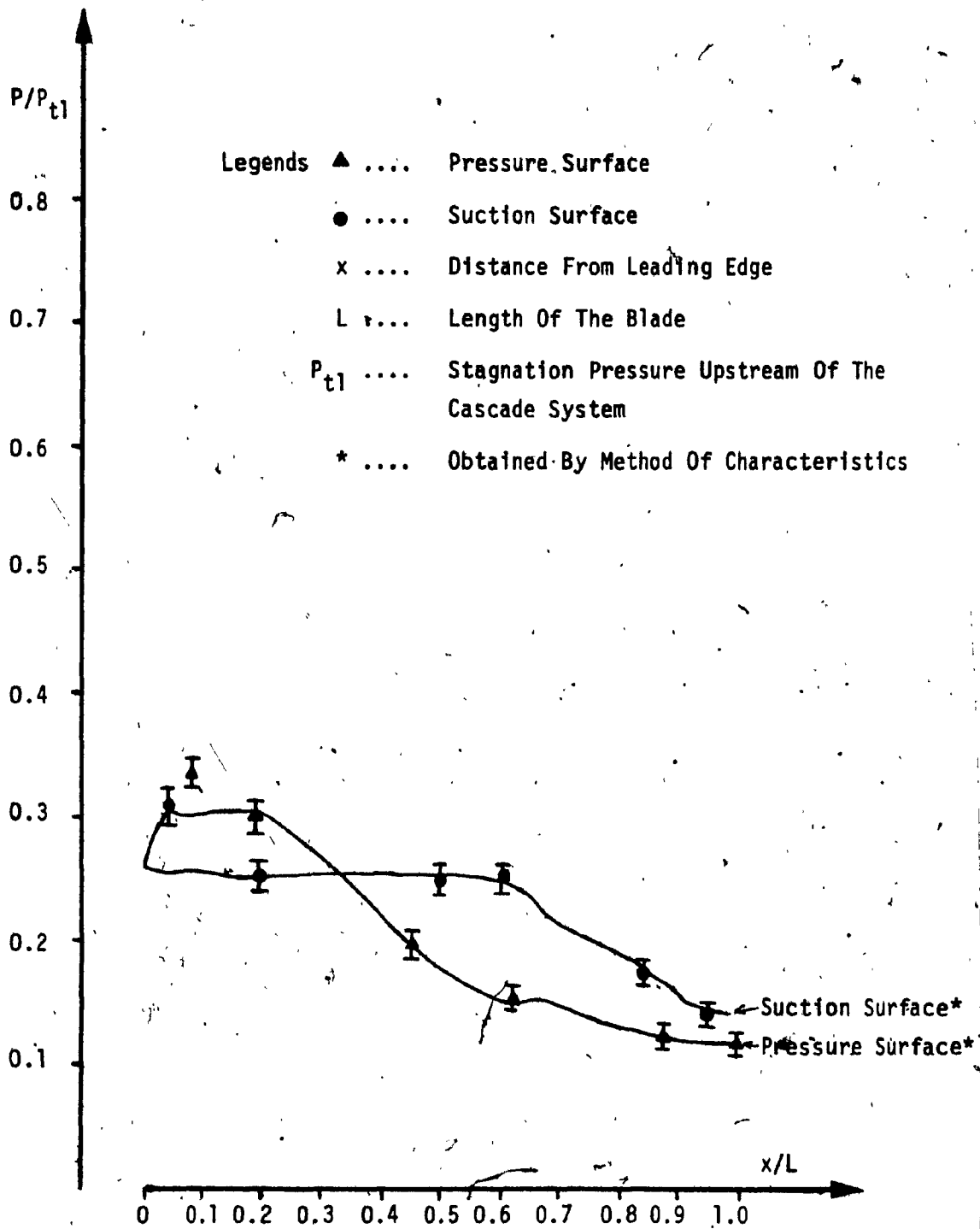


Fig. 27. Surface Pressure Distribution For Pressure Ratio Of 1.40 And Zero Angle Of Incidence.

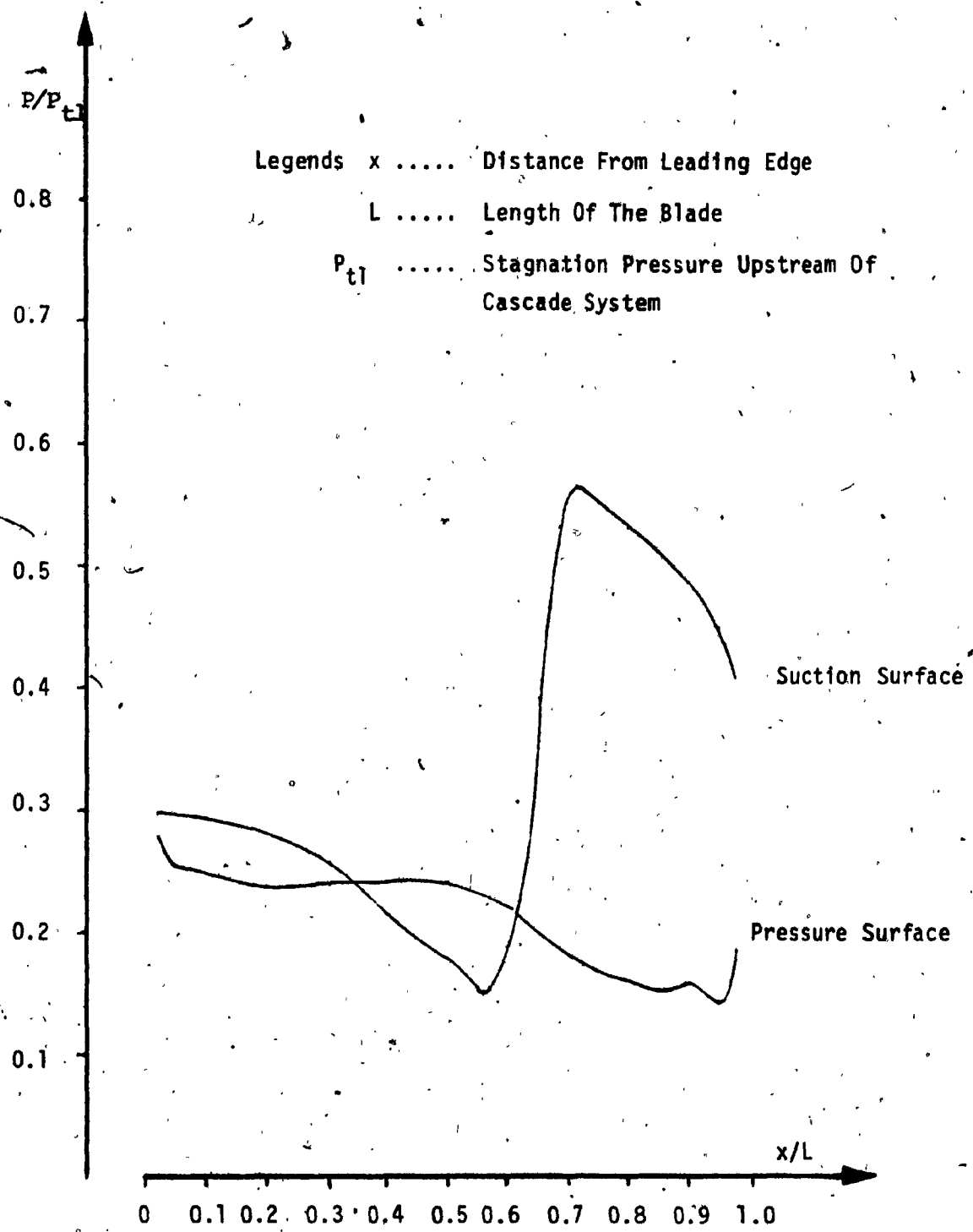


Fig. 28. Surface Pressure Distribution Provided By PWAC For 1.64 Pressure Ratio And Zero Angle Of Incidence.

Table 1. Coordinate Points of the Blade  
Surfaces





PRESSURE SURFACE				SUCTION SURFACE			
x ORDINATE	y ORDINATE	REGION (SEGMENT)	ANGLE FROM POSITIVE y DIRECTION*	x ORDINATE	y ORDINATE	REGION (SEGMENT)	ANGLE FROM POSITIVE y DIRECTION*
-1.118	-1.574			-1.118	-1.574		
-1.091	-1.565	0	17.67	-1.126	-1.547	0	-73.26
-0.986	-1.382	1	60.15	-1.034	-1.357	1	64.16
-0.883	-1.198	2	* 60.76	-0.943	-1.167	2	64.40
-0.780	-1.014	3	60.76	-0.851	-0.978	3	64.04
-0.678	-0.829	4	61.13	-0.758	-0.788	4	63.92
-0.578	-0.644	5	61.60	-0.666	-0.599	5	64.04
-0.478	-0.458	6	61.74	-0.574	-0.410	6	64.04
-0.380	-0.271	7	62.34	-0.482	-0.221	7	64.04
-0.283	-0.084	8	62.58	-0.390	-0.031	8	64.16
-0.186	0.105	9	62.83	-0.298	0.159	9	64.16
-0.091	0.294	10	63.31	-0.207	0.348	10	64.29
0.007	0.484	11	63.92	-0.115	0.539	11	64.28
0.096	0.676	12	63.91	-0.022	0.730	12	64.04
0.190	0.867	13	63.80	0.074	0.921	13	63.32
0.286	1.057	14	63.19	0.117	1.110	14	61.41
0.385	1.247	15	62.48	0.284	1.296	15	60.09
0.485	1.435	16	62.00	0.397	1.480	16	58.67
0.587	1.622	17	61.42	0.514	1.660	17	56.98
0.691	1.807	18	60.66	0.635	1.836	18	55.49
0.795	1.991	19	60.52	0.759	2.010	19	54.37
0.898	2.173	20	60.49	0.886	2.180	20	53.40
0.896	2.182	21	-74.64	0.896	2.182	21	11.13

\*Positive direction is counter-clockwise

Table 2a. Wave Diagram Calculation Steps for  
4 Degrees Angle of Incidence

POINTS	(Q WAVE)	(R WAVE)	$\nu(^{\circ})$	$\theta(^{\circ})$	$\mu(^{\circ})$	$\theta+\mu(^{\circ})$	$\theta-\mu(^{\circ})$	M	P/Pt <sub>1</sub>
1-16	-13.05	38.63	12.79	-25.84	40.81	14.97	-66.65	1.530	0.2608
17	-13.05	38.15	12.55	-25.60	41.07	15.47	-66.67	1.522	0.2640
18-19	-13.05	38.15	12.55	-25.60	41.07	15.47	-66.67	1.522	0.2640
20-21	-13.05	38.87	12.91	-25.96	40.68	14.72	-66.64	1.534	0.2550
22-23	-13.05	38.99	12.97	-26.02	40.62	14.60	-66.64	1.536	0.2500
24-25	-13.05	38.87	12.91	-25.97	40.68	14.72	-66.64	1.534	0.2550
26-27	-13.05	38.87	12.91	-25.96	40.68	14.72	-66.64	1.534	0.2550
28-29	-13.05	38.63	12.79	-25.84	40.81	14.97	-66.65	1.530	0.2608
x	-13.05	38.75	12.85	-25.90	40.75	14.85	-66.65	1.532	0.2553
y	-20.29	39.42	9.57	-29.85	44.77	14.95	-74.52	1.420	0.3055
30-31	-20.29	39.00	9.34	-29.65	45.06	15.41	-74.71	1.413	0.3085
32	-19.80	39.00	9.76	-29.24	44.50	15.26	-73.74	1.427	0.3025
33-34	-12.68	38.74	13.03	-25.71	40.55	14.84	-66.26	1.538	0.2577
35-36	-20.29	38.74	9.23	-29.51	45.25	15.74	-74.76	1.408	0.3107
37	-19.80	38.74	9.47	-29.27	44.90	15.63	-74.17	1.417	0.3068
38	-19.74	38.74	9.50	-29.24	44.86	15.62	-74.10	1.418	0.3066
39-40	-12.86	38.58	12.86	-25.72	40.74	15.02	-66.46	1.532	0.2600
41-42	-20.29	38.58	9.15	-29.44	45.36	15.92	-74.80	1.405	0.3110
43	-19.80	38.58	9.39	-29.19	45.01	15.82	-72.20	1.414	0.3081
44	-19.74	38.58	9.42	-29.16	44.96	15.81	-74.13	1.415	0.3077
45	-19.16	38.58	9.71	-28.87	44.57	15.70	-73.44	1.425	0.3034
46-47	-12.68	39.96	13.64	-26.32	39.91	13.59	-66.23	1.559	0.2494
48-49	-20.29	39.96	9.84	-30.13	44.41	14.27	-74.53	1.429	0.3016
50	-19.80	39.96	10.08	-29.88	44.07	14.19	-73.95	1.438	0.2979
51	-19.74	39.96	10.11	-29.85	44.03	14.18	-73.88	1.439	0.2974

POINTS (Q WAVE)	(R WAVE)	$v(^{\circ})$	$\theta(^{\circ})$	$\mu(^{\circ})$	$\theta+\mu(^{\circ})$	$\theta-\mu(^{\circ})$	M	P/Pt <sub>1</sub>	
52	-19.16	39.96	10.40	-29.56	43.65	14.09	-73.21	1.493	0.2971
53	-16.56	39.96	11.70	-28.56	42.05	13.79	-70.31	1.493	0.2752
54	-12.68	40.68	14.00	-26.68	39.54	12.86	-66.21	1.571	0.2455
55	-20.29	40.68	10.20	-30.49	43.92	13.44	-74.40	1.442	0.2961
56	-19.80	40.68	10.44	-30.24	43.60	13.36	-73.84	1.450	0.2923
57	-19.74	40.68	10.47	-30.21	43.56	13.35	-73.77	1.451	0.2923
58	-19.16	40.68	10.76	-29.92	43.19	13.27	-73.11	1.461	0.2882
59	-16.56	40.68	12.06	-28.62	41.63	13.01	-70.25	1.505	0.2705
60	-14.64	40.68	13.02	-27.66	40.56	12.90	-68.22	1.538	0.2579
61	-12.68	44.50	15.91	-28.59	37.71	9.12	-66.30	1.635	0.2234
63	-20.25	44.50	12.13	-32.37	41.56	9.19	-73.93	1.507	0.2700
64	-19.80	44.50	12.35	-32.15	41.30	9.15	-73.45	1.515	0.2665
65	-19.74	44.50	12.35	-32.15	41.30	9.15	-73.45	1.515	0.2665
66	-19.16	44.50	12.67	-31.83	40.95	9.12	-72.78	1.526	0.2623
67	-16.56	44.50	13.97	-30.53	39.56	9.03	-70.09	1.570	0.2459
68	-14.64	44.50	14.93	-29.57	38.62	9.04	-68.19	1.602	0.2346
69	-9.84	44.50	17.33	-27.17	35.44	9.27	-63.61	1.684	0.2376
70-71	-12.68	47.14	17.23	-29.91	36.52	6.61	-66.43	1.680	0.2088
72	-20.20	47.14	13.47	-33.67	40.08	6.41	-73.75	1.553	0.2521
73	-19.80	47.14	13.67	-33.47	39.88	6.41	-73.35	1.560	0.2496
74	-19.74	47.14	13.70	-33.44	39.87	6.43	-73.31	1.560	0.2496
75	-19.16	47.14	14.00	-33.15	39.55	6.40	-72.70	1.571	0.2455
76	-16.56	47.14	15.29	-31.85	38.27	6.42	-70.12	1.615	0.2303
77	-14.64	47.14	16.25	-30.89	37.38	6.49	-68.12	1.647	0.2194
78	-9.84	47.14	18.65	-28.49	35.34	6.85	-63.83	1.729	0.1940
79	-5.02	47.14	21.06	-26.08	33.50	7.42	-59.58	1.812	0.1709

POINTS (Q WAVE)	(R WAVE)	$v(^{\circ})$	$\theta(^{\circ})$	$\mu(^{\circ})$	$\theta+\mu(^{\circ})$	$\theta-\mu(^{\circ})$	M	P/Pt <sub>1</sub>	
80-81	-12.82	49.98	18.65	-31.33	35.34	4.01	-66.67	1.729	0.1940
82	-20.18	49.98	14.90	-35.08	38.64	3.56	-73.72	1.601	0.2348
83	-19.80	49.98	15.09	-34.89	38.46	3.57	-73.35	1.608	0.2326
84	-19.74	49.98	15.12	-34.86	38.43	3.57	-73.29	1.609	0.2323
85	-19.16	49.98	15.41	-34.57	38.16	3.59	-72.73	1.619	0.2289
86	-16.56	49.98	15.71	-33.27	36.97	3.71	-70.24	1.663	0.2131
87	-14.64	49.98	17.67	-32.31	36.15	3.84	-68.46	1.700	0.2041
88	-9.84	49.98	20.07	-29.91	34.24	4.33	-64.15	1.777	0.1802
89	-5.02	49.98	22.48	-27.50	32.50	5.00	-60.00	1.861	0.1585
90	-2.42	49.98	23.78	-26.20	31.63	5.43	-57.83	1.907	0.1477
91-92	-12.68	49.98	18.65	-31.33	35.34	4.01	-66.67	1.729	0.1940
93	-20.15	49.98	14.92	-35.07	38.63	3.56	-73.70	1.602	0.2477
94	-19.80	49.98	15.09	-34.89	38.46	3.67	-73.35	1.608	0.2326
95	-19.74	49.98	15.12	-34.86	38.43	3.67	-73.00	1.609	0.2322
96	-19.16	49.98	15.41	-34.57	38.16	3.59	-72.73	1.619	0.2288
97	-16.56	49.98	16.71	-33.27	36.98	3.71	-70.25	1.663	0.2143
98	-14.64	49.98	17.67	-32.31	36.15	3.84	-68.46	1.695	0.2041
99	-9.84	49.98	20.07	-29.91	34.24	4.33	-64.15	1.777	0.1802
100	-5.02	49.98	22.48	-27.50	32.50	5.00	60.00	1.861	0.1585
101	-2.42	49.98	23.78	-26.20	31.63	5.43	-57.83	1.907	0.1477
102	-3.64	49.98	23.17	-26.81	32.04	5.23	-58.85	1.885	0.1527
103-104	-12.68	53.37	20.34	-33.02	34.03	1.00	-67.05	1.787	0.1776
105	-20.10	53.37	16.64	-36.74	37.04	0.30	-73.78	1.660	0.2151
106	-19.80	43.37	16.79	-36.59	36.91	0.32	-75.60	1.665	0.2134
107	-19.74	53.37	16.82	-36.56	36.88	0.33	-73.44	1.666	0.2132
108	-19.16	53.37	17.11	-36.27	36.63	0.32	-72.90	1.676	0.2100

POINTS (Q WAVE)	(R WAVE)	$v(^{\circ})$	$\theta(^{\circ})$	$\mu(^{\circ})$	$\theta+\mu(^{\circ})$	$\theta-\mu(^{\circ})$	M	P/Pt <sub>1</sub>	
109	-16.56	53.37	18.41	-34.97	35.31	0.34	-70.28	1.730	0.1932
110	-14.64	53.37	19.37	-34.01	34.78	0.77	-68.79	1.753	0.1870
111	-9.84	53.37	21.77	-31.61	33.00	1.40	-64.61	1.836	0.1647
112	-5.02	53.37	24.18	-29.20	31.37	2.18	-60.57	1.921	0.1449
113	-2.42	53.37	25.48	-27.90	30.55	2.66	-58.45	1.967	0.1345
114	-3.64	53.37	25.87	-28.50	30.93	2.43	-59.43	1.946	0.1391
115	-2.65	53.37	25.36	-28.01	30.62	2.61	-58.63	1.963	0.1354
116-117	-12.68	56.34	21.83	-34.51	32.95	-1.56	-67.46	1.838	0.1642
118	-20.06	56.34	18.14	-38.20	35.76	-2.44	-73.96	1.713	0.1992
119	-19.80	56.34	18.27	-38.07	35.65	-2.42	-73.72	1.716	0.1979
120	-19.74	56.34	18.30	-38.04	35.63	-2.41	-73.67	1.717	0.1976
121	-19.16	56.34	18.59	-37.75	35.39	-2.36	-73.14	1.727	0.1946
122	-16.56	56.34	19.89	-36.45	34.37	-2.08	-70.82	1.771	0.1819
123	-14.64	56.34	20.85	-35.49	33.66	-1.82	-69.15	1.804	0.1730
124	-9.84	56.34	23.25	-33.09	31.98	-1.11	-65.07	1.888	0.1521
125	-5.02	56.34	25.66	-30.68	30.44	-0.24	-61.12	1.974	0.1331
126	-2.42	56.34	26.96	-29.38	29.65	-0.28	-59.03	2.021	0.1237
127	-3.64	56.34	26.35	-29.99	30.02	0.03	-60.01	1.999	0.1278
128	-2.65	56.34	36.85	-29.50	29.72	0.23	-59.22	2.017	0.1245
129	-2.34	56.34	27.00	-29.34	29.63	0.29	-58.97	2.022	0.1235
130-131	-12.68	58.58	22.95	-35.63	32.18	-3.45	-67.81	1.878	0.1543
132	-20.05	58.58	19.27	-39.32	34.86	-4.46	-74.18	1.750	0.1878
133	-19.80	58.58	19.39	-39.19	34.76	-4.43	-73.95	1.754	0.1867
134	-19.74	58.58	19.42	-39.16	34.74	-4.42	-73.90	1.755	0.1864
135	-19.16	58.58	19.71	-38.87	34.51	-4.36	-73.38	1.765	0.1836
136	-16.56	58.58	21.01	-37.57	33.54	-4.03	-71.11	1.810	0.1714

	POINTS (Q WAVE)	(R WAVE)	$v(^{\circ})$	$\theta(^{\circ})$	$\mu(^{\circ})$	$\theta+\mu(^{\circ})$	$\theta-\mu(^{\circ})$	M	P/Pt <sub>1</sub>
137	-14.64	58.58	21.97	-36.61	32.85	-3.75	-69.46	1.843	0.1630
138	-9.84	58.58	24.37	-34.21	31.25	-2.96	-65.46	1.928	0.1429
139	-5.02	58.58	26.78	-31.80	29.76	-2.04	-61.56	2.015	0.1249
140	-2.42	58.58	28.78	-30.50	29.00	-1.50	-59.50	2.062	0.1160
141	-3.64	58.58	27.47	-31.11	29.35	-1.77	-60.46	2.040	0.1201
142	-2.65	58.58	27.97	-30.62	29.07	-1.55	-59.66	2.058	0.1167
143	-2.34	58.58	28.12	-30.46	28.98	-1.47	-59.44	2.064	0.1157
144	-0.44	58.58	29.07	-29.51	28.45	-1.06	-57.96	2.099	0.1220
145	-12.68	58.58	22.95	-35.63	32.18	-3.45	-67.81	1.878	0.1543
146	-12.68	60.52	23.92	-36.60	31.54	-5.06	-68.14	1.912	0.1465

Table 2b. Wave Diagram Calculation Steps for  
0 Degrees Angle of Incidence



POINTS	(Q WAVE)	(R WAVE)	$v(^{\circ})$	$\theta(^{\circ})$	$\mu(^{\circ})$	$\theta+\mu(^{\circ})$	$\theta-\mu(^{\circ})$	M	P/Pt <sub>1</sub>
21	-10.86	36.44	12.79	-23.65	40.88	17.23	-64.53	1.528	0.2654
22-31	-10.86	36.44	12.79	-23.65	40.88	17.23	-64.53	1.528	0.2654
32-41	-11.93	40.80	14.44	-26.36	39.09	12.73	-65.45	1.586	0.2402
32'-41'	-10.90	40.80	14.95	-25.85	38.60	12.75	-65.45	1.603	0.2343
42-51	-10.90	41.02	15.05	-25.96	38.60	12.64	-64.56	1.603	0.2343
52-59	-10.90	41.02	15.05	-25.96	38.60	12.64	-64.56	1.603	0.2343
60-67	-10.90	41.02	15.05	-25.96	38.60	12.64	-64.56	1.603	0.2343
68	-10.90	41.02	15.05	-25.96	38.60	12.64	-64.56	1.603	0.2343
69	-18.83	40.87	11.02	-29.85	42.86	13.01	-72.71	1.470	0.2845
70	-18.83	40.87	11.02	-29.85	42.86	13.01	-72.71	1.470	0.2845
71-77	-10.90	40.78	14.94	-25.84	38.61	12.77	-64.45	1.603	0.2343
78	-10.90	40.78	14.94	-25.84	38.61	12.77	-64.45	1.603	0.2343
79	-18.83	40.78	10.98	-29.80	42.92	13.12	-72.71	1.468	0.2853
80	-18.83	40.78	10.98	-29.80	42.92	13.12	-72.71	1.468	0.2853
81	-17.70	40.78	11.54	-29.24	42.24	13.00	-71.48	1.487	0.2776
82	-10.90	40.78	14.94	-25.84	38.61	12.76	-64.45	1.603	0.2343
83-87	-10.90	40.78	14.94	-25.84	38.61	12.76	-64.45	1.603	0.2343
88	-10.90	40.78	14.94	-25.84	38.61	12.76	-64.45	1.603	0.2343
89	-18.83	40.78	10.98	-29.80	42.92	13.12	-72.72	1.468	0.2853
90	-18.83	40.78	10.98	-29.80	42.92	13.12	-72.72	1.468	0.2853
91	-17.70	40.78	11.54	-29.24	42.25	13.00	-71.48	1.487	0.2776
92	-15.88	40.78	12.46	-28.33	41.18	12.85	-69.51	1.519	0.2651
93-97	-10.90	44.38	16.74	-27.64	36.95	9.31	-64.59	1.664	0.2138
98	-10.90	44.38	16.74	-27.64	36.95	9.31	-64.59	1.664	0.2138
99	-18.83	44.38	12.78	-31.60	40.83	9.23	-72.43	1.530	0.2610
100	-18.83	44.38	12.78	-31.60	40.83	9.23	-72.43	1.530	0.2610

POINTS	(Q WAVE)	(R WAVE)	$\nu(^{\circ})$	$\theta(^{\circ})$	$\mu(^{\circ})$	$\theta+\mu(^{\circ})$	$\theta-\mu(^{\circ})$	M	P/Pt <sub>1</sub>
101	-17.70	44.38	13.34	-31.04	40.22	9.18	-71.24	1.549	0.2538
102	-15.88	44.38	14.25	-30.13	39.28	9.15	-69.41	1.579	0.2427
103	-10.21	44.38	17.09	-27.29	36.64	9.35	-63.93	1.676	0.2102
104-108	-10.90	48.92	19.01	-29.91	35.06	5.15	-64.97	1.741	0.1904
109	-10.90	48.92	19.01	-29.91	35.06	5.15	-64.97	1.741	0.1904
110	-18.83	48.92	15.05	-33.87	38.50	4.63	-72.37	1.606	0.2332
111	-18.83	48.92	15.05	-33.87	38.50	4.63	-72.37	1.606	0.2332
112	-17.70	48.92	15.61	-33.31	37.97	4.66	-71.28	1.625	0.2267
113	-15.88	48.92	16.52	-32.40	37.14	4.74	-69.54	1.656	0.2164
114	-10.21	49.92	19.35	-29.57	34.79	5.23	-64.35	1.753	0.1898
115	-3.24	48.92	22.84	-26.08	32.25	6.17	-58.34	1.874	0.1553
116-119	-10.90	51.76	20.43	-31.33	33.97	2.64	-65.30	1.790	0.1767
120	-10.90	51.76	20.43	-31.33	33.97	2.64	-65.30	1.790	0.1767
121	-18.83	51.76	16.45	-35.29	37.19	1.90	-72.48	1.654	0.2171
122	-18.83	51.76	16.45	-35.29	37.19	1.90	-72.48	1.654	0.2171
123	-17.70	51.76	17.03	-34.73	36.70	1.97	-71.43	1.673	0.2110
124	-15.88	51.76	17.94	-33.82	35.92	2.10	-69.74	1.703	0.2014
125	-10.21	51.76	20.77	-30.90	33.71	2.73	-64.70	1.802	0.1735
126	-3.24	51.76	24.26	-27.50	31.31	3.82	-58.81	1.923	0.1440
127	-1.84	51.76	24.96	-26.80	30.87	4.70	-57.67	1.949	0.1383
128	-10.90	55.14*	22.14	-33.02	32.75	-0.27	-65.77	1.848	0.1617
129	-18.83	55.14	18.16	-36.98	35.74	-1.24	-72.72	1.712	0.1990
130	-17.70	55.14	18.72	-36.42	35.29	-1.13	-71.71	1.731	0.1933
131	-15.87	55.14	19.63	-35.51	34.57	-0.94	-70.08	1.762	0.1844
132	-10.21	55.14	22.47	-32.68	32.61	-0.16	-65.19	1.860	0.1587
133	-3.24	55.14	25.95	-29.19	30.27	1.08	-59.46	1.984	0.1310

POINTS	(Q WAVE)	(R WAVE)	$v(^{\circ})$	$\theta(^{\circ})$	$\mu(^{\circ})$	$\theta+\mu(^{\circ})$	$\theta-\mu(^{\circ})$	M	P/Pt <sub>1</sub>
134	-1.84	55.14	26.65	-28.49	29.84	1.35	-58.33	2.010	0.1258
135	-2.02	55.14	26.56	-28.58	29.89	1.31	-58.47	2.000	0.1278
136	-10.90	58.12	23.61	-34.51	31.74	-2.77	-66.25	1.900	0.1492
137	-10.90	58.12	23.61	-34.51	31.74	-2.77	-66.25	1.900	0.1492
138	-10.90	58.12	23.61	-34.51	31.74	-2.77	-66.25	1.900	0.1492
139-140	-10.90	58.12	23.61	-34.51	31.74	-2.77	-66.25	1.900	0.1492
141	-18.80*	58.12	19.64	-38.47	34.56	-3.90	-73.03	1.762	0.1844
142	-17.70	58.12	20.21	-37.91	34.13	-3.77	-72.04	1.782	0.1787
143	-15.88	58.12	21.12	-37.00	33.46	-3.54	-70.46	1.814	0.1704
144	-10.21	58.12	23.96	-34.16	31.51	-2.65	-65.67	1.913	0.1463
145	-3.24	58.12	27.44	-30.68	29.37	-1.31	-60.05	2.039	0.1203
146	-1.84	58.12	28.14	-29.98	28.97	-1.00	-58.95	2.064	0.1157
147	-2.02	58.12	28.05	-30.07	29.02	-1.05	-59.09	2.061	0.1162
148	-0.86	58.12	28.63	-29.49	28.70	-0.79	-58.19	2.083	0.1123
149-152	-10.90	60.36	24.73	-35.63	31.01	-4.62	-66.65	1.941	0.1401
153	-18.80*	60.36	20.78	-39.58	33.71	-5.87	-73.29	1.802	0.1735
154	-17.70	60.36	21.33	-39.03	33.31	-5.72	-72.33	1.821	0.1685
155	-15.88	60.36	22.24	-38.12	32.67	-5.45	-70.79	1.853	0.1605
156	-10.21	60.36	25.07	-35.29	30.80	-4.49	-66.09	1.953	0.1374
157	-3.21	60.36	28.57	-31.79	28.73	-3.05	-60.52	2.080	0.1128
158	-1.84	60.36	29.26	-31.10	28.35	-2.75	-59.45	2.106	0.1084
159	-2.02	60.36	29.17	-31.19	28.39	-2.80	-59.59	2.103	0.1089
160	-0.86	60.36	39.75	-30.60	28.08	-2.53	-58.69	2.124	0.1053

Note: \*Value obtained by trial and error.

